秋田県立大学大学院博士学位論文

Construction of the Polymers-Based Interfacial Solar Evaporation Systems for Water Purification and Desalination

（ポリマーベース界面蒸発システムの構築および水の浄化と海水淡水化への応用）

Zhaoxing Lin

林 肇星

2022 年 9 月

Abstract

Energy crisis, shortage of freshwater resources, and increasingly serious water pollution are the challenges facing the world today. In recent years, the technology of solar-driven water interfacial evaporation has developed rapidly. The technology of using solar energy to heat seawater or wastewater to obtain steam can develop eco-friendly and cost-effective freshwater production, and meet the energy and environmental needs at the same time. It has good application prospects in seawater desalination, sewage treatment, synergistic freshwater-power generation and so on. In recent years, conjugated polymers have been widely studied in this field. Poly(N-phenylglycine) (PNPG) is a kind of conjugated polymer, with easily available raw materials, a simple synthesis process, and good chemical and environmental stability. At the same time, it has remarkable optical properties and the potential for light-to-heat conversion. This thesis is based on the construction of PNPG-based solar evaporation systems and their applications.

In chapter 1, the research background, research significance, summary of the research, and the construction of this thesis are described. The objectives of the research are to study the PNPG-based solar evaporation systems and their applications.

In chapter 2, the properties of experimental materials, as well as the experimental methods and the characterizations are presented.

In chapter 3, inspired by the Amazon water lily, an interfacial water-trapped structure solar evaporator was developed to achieve a continuous supply of water from

the water-trapped layer and three-dimensional heat distribution management. The artificial photothermal membrane with PNPG can be easily prepared by vacuum filtration. Then, combined with the three-dimensional heat distribution management design and the water-trapped layer for a continuous supply of water, more optimized energy utilization and efficient interface heating were realized. Besides, because the novel nanoscale PNPG has excellent light capture performance and the absorbed solar energy can be concentrated in the water-trapped layer, which makes the solar evaporation more effective, showing higher energy efficiency (93.5%) and higher evaporation rate (1.72 kg m^{-2} h^{-1}) under 1 sun. This special structure aims to minimize energy loss and better regulate the relationship between water evaporation, solar energy conversion, and heat regulation. This bionic solar evaporator can provide new ideas for designing the structure of high-efficiency solar evaporators and new opportunities for practical applications.

In chapter 4, inspired by the transpiration of trees, a PNPG-wood solar evaporator was developed to further explore the possibility of reducing the cost of the solar evaporator. Compared with PVDF membrane, the price of wood blocks purchased in supermarkets is more competitive. PNPG coating greatly makes up for the weak light absorption of wood, and effectively improves the solar heat conversion efficiency. In addition, thanks to the low thermal conductivity and special microstructure of the wood, the relationship between water transportation, solar energy conversion, and heat regulation was better regulated. As a result, the PNPG-wood system can effectively and quickly generate steam, and the evaporation rate and efficiency can reach 1.64 kg

m^{-2} h^{-1} and 90.4% under 1 sun, which is higher than that of most reported wood-based solar evaporators. Therefore, this kind of solar evaporation system with reasonable design, low cost, durability, and high efficiency has the potential to be applied to solve the practical problem of seawater desalination and water purification.

In chapter 5, to optimize the efficiency and form of solar heat utilization, a synergistic photothermal layer was created from PNPG/MoS_2 nanohybrid by the electrostatic induced assembly for broad-spectrum and efficient solar absorption. The PNPG/MoS_2 system provides effective synergistic photothermal conversion and good water transmission, which enables solar steam to escape quickly. It is worth noting that the synergistic coupling of solar evaporation-thermoelectric (TE) power generation has also been realized, which provides more effective solar energy development. The system demonstrated a solar evaporation rate up to 1.70 kg m^{-2} h^{-1} and achieved a maximum thermoelectric output power of 0.23 W m^{-2} under one sun. The high-performance PNPG/MoS_2 synergistic photothermal system developed in this research provides potential opportunities for coupling solar water purification and thermoelectric power generation to meet the demand of resource-scarce areas.

In chapter 6, general conclusions of this thesis are made.

Contents

Chapter 1 Introduction

1.1 Background

With the continuous growth of the population, water consumption has increased sharply, which directly leads to the lack of clean water. In addition, many industrial activities not only consume large amounts of local water resources but also cause serious water pollution, which further aggravates the shortage of water resources. The shortage of water resources has become the biggest problem hindering the development of human society.[1]

To solve this problem, the technology of seawater desalination has been paid great attention. Traditional seawater desalination includes burning fossil fuels to produce high-temperature evaporation of seawater and capturing steam to produce treated fresh water. This method can treat sea water efficiently and quickly, but on the one hand, it causes a lot of fossil energy consumption. On the other hand, burning fossil fuels will produce a lot of pollutants, which will cause immeasurable harm to the local ecological environment. Therefore, it is urgent to develop a new, efficient, clean, and pollution-free seawater desalination technology to solve the current water crisis.

Seawater desalination based on solar steam power generation technology, using special photothermal conversion materials to collect solar energy to heat seawater and evaporate it, has become one of the most promising new technologies for seawater desalination.[2, 3] On the one hand, it can be attributed to the use of clean and renewable solar energy, no consumption of other energy sources, and environmental

protection. On the other hand, it doesn't need a lot of materials or equipment, which makes the cost of this technology relatively low. In recent years, to improve the energy utilization efficiency of solar steam power generation technology, researchers have made a lot of exploration in the aspects of optical performance adjustment of the light absorber, structure of evaporation device, thermal management, etc., and made great progress, with the efficiency increased to more than 90%.[4, 5] At the same time, the researchers also found that in the application of solar seawater desalination, the energy is mainly consumed in the evaporation process, and it is converted into latent heat through the vapor phase change.[6, 7] This kind of latent heat energy is usually wasted in collecting the solar steam generated. Therefore, to further improve the efficiency of energy utilization, researchers can make small-scale thermoelectric power generation by reusing latent heat of phase change of solar steam based on obtaining clean water, to achieve the goal of water evaporation-cogeneration. In recent years, solar water evaporation co-generation based on high-efficiency solar heat conversion technology has become a new field of solar energy conversion and utilization.[8, 9]

1.2 Development of solar desalination

With the intensification of the world energy crisis and the increasing shortage of fossil fuels, solar energy is one of the most important clean energy sources, which is not only renewable, and pollution-free, but also inexhaustible. The conversion and utilization of solar energy have become a more and more important part of human production and life, and have been developing rapidly. At present, the use of solar

energy can be divided into solar photoelectric conversion and solar thermal conversion, which are widely used in different fields.

Water resources are closely related to people's life and production. However, seawater accounts for up to 97% of the world's water resources, but people can not use it directly because of its high salt content. Less than 2% of fresh water resources can be directly used by human beings, and this proportion is declining due to population growth, industrial development, and the increase in water contamination. The technology of solar steam generation, which combines abundant solar energy and water resources, has attracted much attention for many years and made great progress in recent years.[10, 11] One reason is that this technology uses clean and renewable solar energy, and has less pollution than thermal distillation used in traditional industries. On the other hand, solar seawater desalination based on solar steam power generation technology can make full use of the abundant seawater resources on the earth, which is expected to fundamentally solve the current water shortage crisis.

However, the low efficiency of solar energy severely restricts the development and application of solar evaporation technology. The energy efficiency obtained by traditional methods is only 30%~45%, which can not meet the needs of industrialization. To solve these problems, in recent years, many new and more optimized solar evaporation systems have been put forward, which has greatly promoted the development of this technology.[12]

The typical solar evaporation system can be divided into two parts according to its function: solar thermal conversion material (also known as solar absorber) and water

evaporation area. The traditional solar evaporation method is shown in Fig. 1-1a and is called integral heating or bottom heating. In this type of evaporation system, the absorber effectively converts sunlight into heat to evaporate water, thus promoting the evaporation of the water. However, due to the different positions of the solar heating area and the evaporation area, this leads to a serious and inevitable problem: heat is lost from the heating area to bulk water and the environment. To solve this problem, the researchers put forward a new solar energy evaporation system, nanofluid heating, as shown in Fig. 1-1b. The absorbent consists of nanoparticles dispersed throughout the water. When exposed to light, the nanoparticles absorb the energy of sunlight and heat up, which effectively heating the surrounding water and promoting evaporation. However, when the whole water body is heated, the heat loss to the surrounding environment is very serious, and it is difficult to obtain enough efficient energy-steam conversion efficiency.

Through material characteristics and device design, the energy converted by absorbent can be effectively concentrated on the surface of the water, and the water on the interface can be selectively heated, thus avoiding the energy loss to water and the surrounding environment, thus effectively improving the energy conversion efficiency (Fig. 1-1c). In recent years, many new solar photothermal conversion materials have been developed, and their applications have been extended to many fields such as seawater desalination, disinfection, sewage treatment, power generation, and so on.

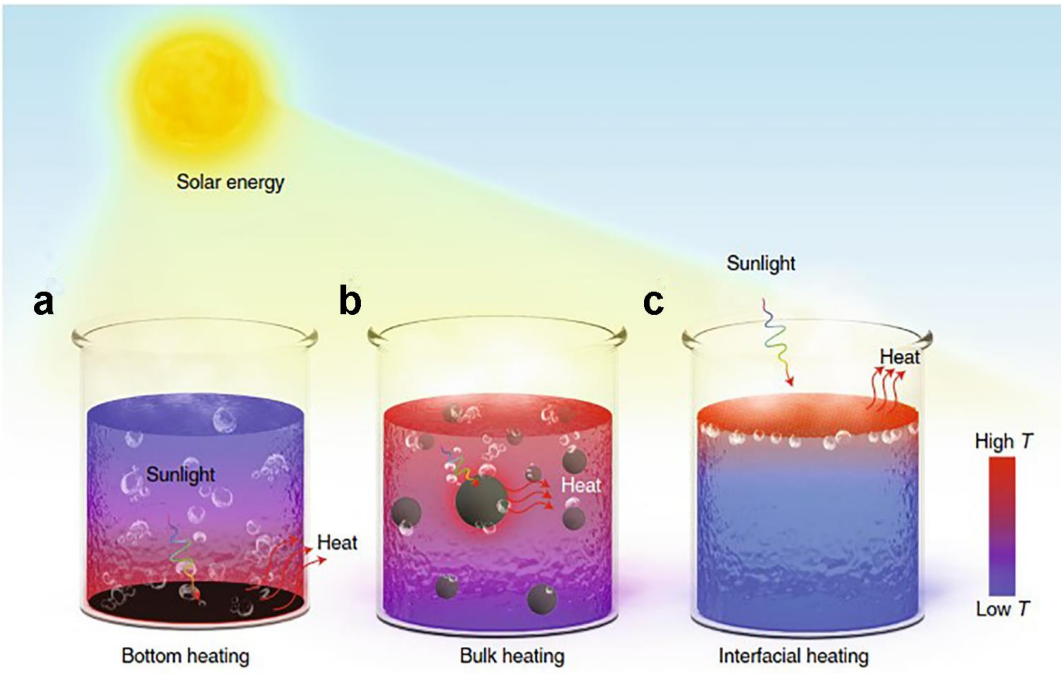

Fig. 1-1 solar-driven evaporation through various forms of solar heating.[12] Copyright 2018 Nature Publishing Group.

1.3 Design principle of the solar evaporators

To develop and design various materials and evaporator structures for solar steam generation, a lot of research has been done. Through material selection, material composition adjustment, and surface engineering, it is possible to achieve a high solar absorption rate of the absorber while limiting thermal emissivity and light reflectivity. In addition, in the process of solar heat conversion, there will be system heat losses caused by conduction, convection, or radiation (Fig. 1-2a), and measures must be taken to reduce such losses.

The solar-absorbing materials not only need to have excellent light-to-heat conversion performance but also should be economical and easy to manufacture on a

large scale. Because the photothermal evaporation efficiency is directly proportional to the area of the solar absorbing material. In addition, they should be durable and have antifouling properties specially designed for brine or waste water purification applications. The requirements of solar absorbers for efficient water evaporation are discussed in detail below.

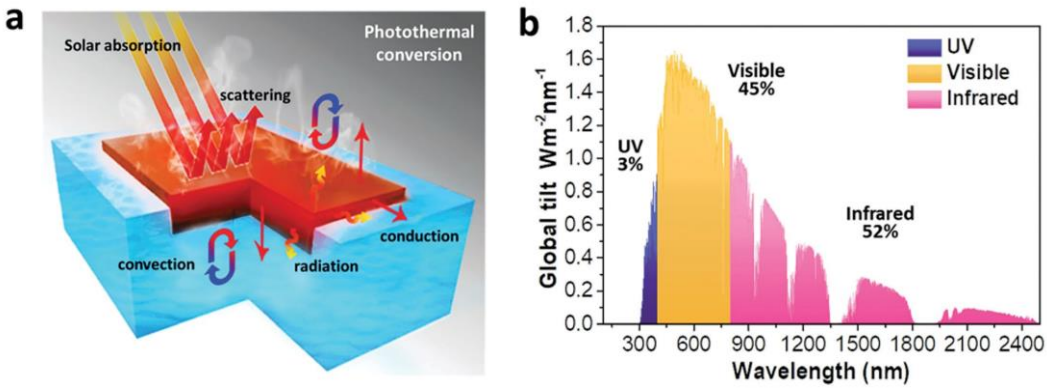

Fig. 1-2 (a) Schematic drawing of the photothermal conversion process for steam generation. (b) Solar spectral irradiance (AM 1.5).[13] Copyright 2019 Royal Society of Chemistry.

1.3.1. Efficient solar absorption and light-to-heat conversion

Photothermal conversion materials can effectively absorb sunlight and rapidly convert the absorbed solar radiation energy into heat energy. Materials and structural design enabling high light absorption over the whole solar spectrum and high-efficiency light-to-heat conversion is the first step toward a high-performance solar evaporation device. As shown in Fig. 1-2b, the distributed solar energy on the earth's surface covers a wide wavelength range of 300 nm to 2500 nm and consists of three parts: the

ultraviolet region (300–400 nm, accounting for 3% of the total energy), the visible region (400–700 nm, accounting for 45% of the total energy), and the infrared region (700–2500 nm, accounting for 52% of the total energy). An ideal light-absorbing material and structure design should be able to absorb the solar energy across the whole solar spectrum to the maximum extent.[13]

To effectively enhance the light absorption and/or photothermal conversion of multifunctional photothermal materials, the synthesis and structural engineering strategies of various materials have been deeply studied, and a series of mechanisms have been described comprehensively in recent research papers and review articles.[9, 10, 14] Here, we focus on some typical strategies: i) Adjust the microstructure of the light absorber so that incident light can be scattered multiple times and transmission and reflection are minimized (Fig. 1-3a,b). ii) Adjust the size and/or shape of the plasma nanoparticles over a wide distribution range to achieve light absorption at multi-wavelength (Fig. 1-3c,d). iii) By adjusting the energy band structure of the semiconductor through atomic doping, light absorption can span a wider wavelength range and achieve higher photothermal conversion efficiency (Fig. 1-3e,f).

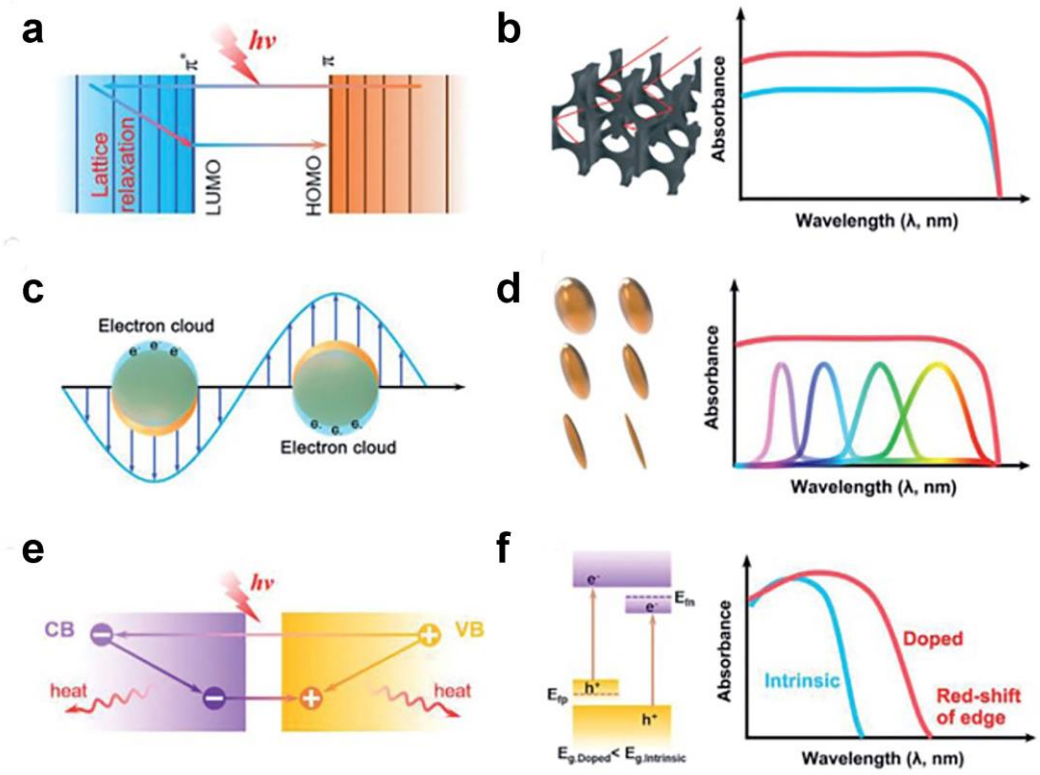

Fig. 1-3 Photothermal physics and materials engineering with different matters in the corresponding light-absorption range. (a) The thermal vibration of molecules and (b) microstructure engineering. (c) Plasmonic heating and (d) adjustment of particle geometry and size. (e) Photoexcitation and relaxation of charge carriers, and (f) energy band structure engineering.[9] Copyright 2020 Royal Society of Chemistry.

1.3.2. Efficient thermal to steam generation

The heat generated by light absorption is effectively transferred to the evaporation process, that is, the heat energy should be mainly used to overcome the latent heat of water evaporation, while all other heat losses including most of the water and surrounding air heating, convection, and blackbody radiation losses should be minimized. To get the maximum evaporation efficiency, the heat generated by the solar

absorber should be transferred entirely for water evaporation. However, in practice, some heat will be consumed by a large amount of heating water and will be lost to the container and the environment through conduction, convection, and radiation.

In this case, a solar simulator or natural solar energy directly irradiates the solar energy-absorbing material in the water. The mass loss of water changes with time and is used to calculate the energy efficiency of the evaporation. Using thermocouples or infrared cameras, you can also measure the temperature of each part of the system to evaluate the temperature rise and heating uniformity. The efficiency η is then calculated as follows in the equation [15-17]:

$$\eta = \frac{(m - m_0) h_V}{C_{opt} P_0} \tag{1}$$

where m is the solar evaporation rate, m_0 is the natural evaporation rate in dark, h_v is the liquid-vapor phase enthalpy, C_{opt} is the optical concentration, and P_0 is the power density of 1 sun irradiation.

Although the energy conversion efficiency can be well improved by the optical properties of solar absorbers, the severe heat loss during evaporation remains a major obstacle to further improving solar-to-steam efficiency. As mentioned earlier, there are three types of energy losses in typical interfacial photothermal systems, including conduction heat loss, which is caused by the inevitable temperature gradient between the high-temperature surface of the absorber and the low-temperature bulk water. These three kinds of heat losses seriously inhibit the performance of the solar interface steam generation system. To solve this problem, it is necessary to carry out effective thermal management of the whole device.

To optimize efficiency, materials with low thermal conductivity and high solar absorption are used as absorbers to achieve better energy localization. In 2016, Hu et al. reported a great potential aerogel absorber based on graphene oxide and carbon nanotubes[18] It has the advantages of good adsorption properties, low cost, simple preparation method, and large-scale production. Moreover, it has light weight and thermal conductivity, to ensure its self-floating in the evaporation process, which can greatly inhibit the conduction loss of heat to water.

1Besides the characteristics of the absorber material, a well-designed evaporation structure can also make a considerable contribution to limiting heat loss. Li et al. demonstrated an interfacial photothermal structure based on two-dimensional water channels.[19] The authors used low thermal conductivity, dense, non-porous insulation material as an insulation layer, and wrapped it with a cellulose film as a water transmission path. Water is confined in the two-dimensional transmission channel to further reduce heat loss. In this structure, the water transport capacity will be restrained to some extent, but the heat conduction loss can be significantly reduced by the closed water channel. The energy conversion efficiency can reach 80% when combined with graphene oxide-based absorbent with high water absorption and good hydrophilicity.

1.3.3. Water transportation

Generally, the ideal water transport process is to transport a proper amount of water to the surface of the solar evaporator to achieve the desired evaporation efficiency (too much water may increase conduction losses in the evaporation processes, and too little water is not enough to support it. The water transportation process generally

depends on the capillary force generated by the evaporator structure, and the water transportation process can be better realized with the help of capillary force. Therefore, these devices usually use super absorbent materials, such as cotton, filter paper, and gauze, to transport seawater. In addition, it is also necessary to discharge the water vapor generated after heating in time, otherwise, the generated steam will be cooled on the spot, and secondary heating will occur, resulting in a decrease in evaporation efficiency. To meet these two requirements, researchers designed different internal structures of photothermal conversion materials to ensure water transportation and diffuse the water vapor in them, to promote the seawater to be converted into steam and discharge the steam in time, thus greatly improving the energy efficiency.

However, the problem still exists, because the conversion of light to heat occurs on the surface of light-absorbing materials, and these systems need to be constantly replenished with water or directly contacted with bulk water to meet evaporation requirements. Therefore, driven by thermal diffusion, there is a large amount of heat loss in the non-evaporative part of the fluid. Meanwhile, the internal structure of the evaporator is also very important. It not only determines some properties of the material but also plays an important role in the evaporation of water from the sun. It can be seen from the literature in recent years that structure affects factors such as water transport and heat loss level and then affects water evaporation efficiency.

Hu's team designed a jellyfish-like solar steam generator, which is composed of a porous carbon black/graphene oxide (CB/GO) composite layer, aligned GO columns, and an expanded polystyrene matrix.[20] The porous CB/GO composite layer has good

fibrous channels, which is beneficial to water transport. And it has high broadband light absorption (99%) in the wavelength range of 250−2500 nm. The linear water transport in the GO pillars can greatly reduce the contact area between the evaporation layer and scattering water, effectively. It suppresses the heat dissipation of the scattered water. Similarly, Yu's research team showed a gel-based on polyvinyl alcohol (PVA) and polypyrrole (PPy), which can be used as an independent solar steam generator. (Fig. 1-4).[21] The converted energy can be used in situ, and the nanopore's numerous structures are beneficial to the transport of water. At the same time, the evaporation of water provides a driving force for water transport in the molecular grid of the PVA network, and the hydrogel skeleton promotes the evaporation of water. Due to the penetration of the solar absorber in the polymer gel network, the converted solar energy can be directly transferred to a small amount of water in the molecular grid under the irradiation of light. The PVA chain eliminates the main energy loss pathway for solar steam generators-convective heat loss from water. In addition, fast water diffusion and capillary pumping through microchannels and internal gaps allow the polymer network to rapidly replenish the molecular grid by swelling to maintain a high rate of steam generation. Importantly, the evaporation enthalpy of water in the gel molecular grid is smaller than that of bulk water. Therefore, the water evaporation rate of water is high.

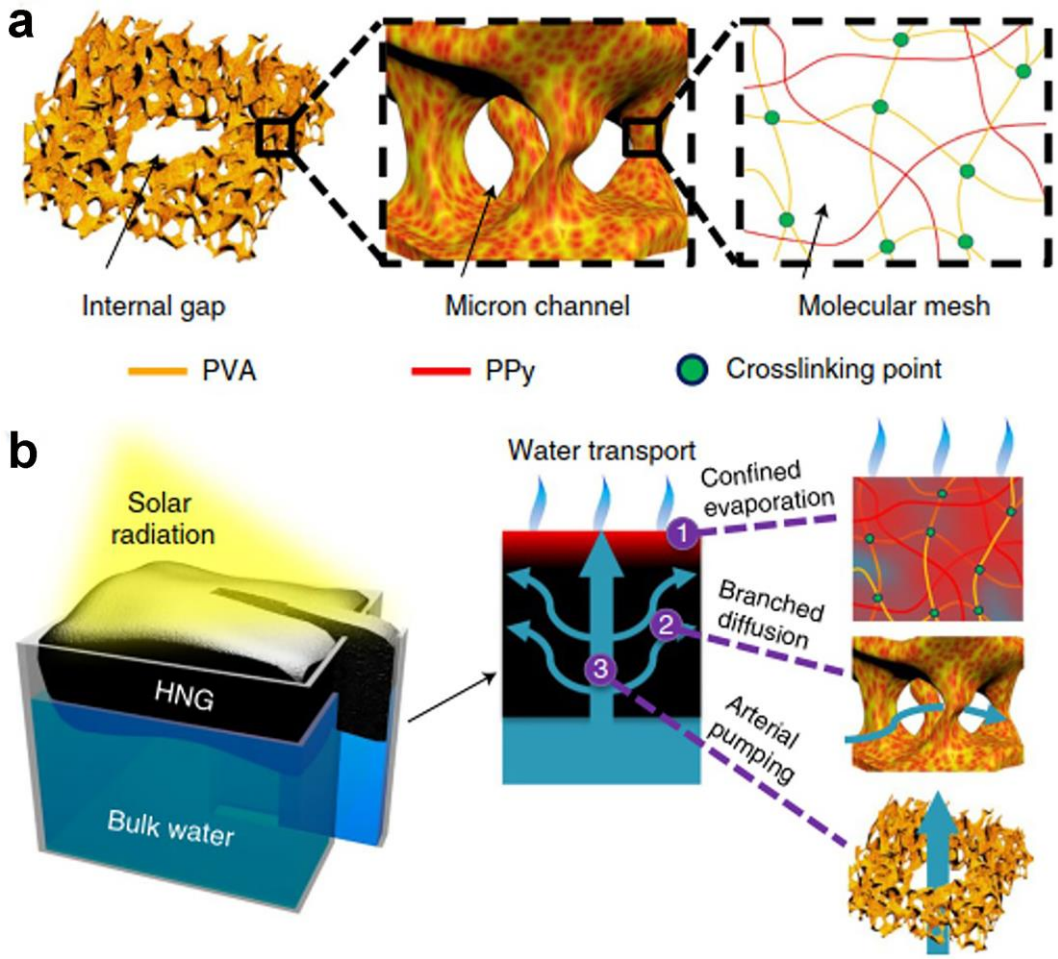

Fig. 1-4 (a) The three-dimensional network structure diagram of the gel. (b) Water evaporation diagram and three different water transport channels.[21] Copyright 2018 Nature Publishing Group.

1.3.4. Bionic structure design

Over millions of years of evolution, nature has become a master at building various complicated structures. These structures bring great inspiration to structural design in many fields of human beings. For example, inspired by the structure and physiological process of trees, a two-in-one solar-driven evaporation/photocatalysis system for efficient water evaporation and in situ purification was fabricated from wood-derived

porous carbon.[22] The system can quickly evaporate (up to 3.23 kg m^{-2} h^{-1}) and effectively purify the mixed volatile wastewater containing rhodamine B, phenol, and tetracycline with a total concentration is up to 11700 mg L^{-1} under one sun irradiation, which was significantly higher than the previously reported concentration. Meanwhile, distilled water with no detected volatile pollutants could be obtained. Besides the tree structure, biological structures such as flowers, reeds, sphagnum, and lotus flowers also provide a lot of inspiration for the structural design of the absorber.[23-26]

1.4 Polymer-based solar evaporators and their application

Polymer is a promising candidate material for constructing solar evaporators. They can be designed from the molecular level to the macro level to achieve the chemical and physical characteristics required by high-efficiency solar evaporators (for example, high solar absorption rate, fast water pumping, excellent heat insulation, and low density). First of all, conjugated polymers with various tight π-stacked microstructures, such as polypyrrole (PPy), polydopamine (PDA), and polyaniline (PANI), have broadband absorption in the solar spectrum. Because of their simple synthesis process and easy integration with many other materials, they have been widely used as light absorbing materials in solar evaporation systems. Secondly, lightweight insulating porous polymer foams, such as polystyrene (PS), polyurethane (PU), or aerogels, can be used as self-floating and insulating support bases for the solar evaporator, minimizing the heat loss from the external environment. In addition, various processing characteristics of polymer materials provide additional opportunities to improve the

performance of solar evaporation systems, such as effective water lock control or effective salt resistance in the evaporator.

With the rapid development of solar evaporation systems, the related important applications have attracted the attention of researchers. At present, solar evaporation systems are mainly used for clean water production, including seawater desalination and sewage treatment.

1.4.1 Classification of polymer-based solar evaporators

1.4.1.1 Conjugated polymers

Conjugated polymers are a kind of important macromolecules, which have a delocalized π-electron system in the main chain of polymers. Since the discovery of polyacetylene doping, many other novel polymers with high structural diversity and stability in neutral and doped states have been successfully synthesized and applied in different fields, such as batteries, organic electronics, solar cells, and biomedicine. In addition, due to their excellent photothermal conversion properties, these polymers have recently attracted great interest in the field of solar evaporation. They are very effective for solar thermal energy conversion because the incident photons can be converted into thermal energy by non-radiative relaxation and molecular vibrations in polymers.

Polypyrrole (PPy). PPy is known to possess excellent photothermal performance and low thermal conductivity, so it is an ideal candidate material for solar-thermal energy conversion. Li et al. reported a one-step, low-cost, and mass-productive synthesis method for photothermal materials, which is based on origami PPy and the

original portable low-pressure controlled solar steam collection system with high synergies in water evaporation and steam collection.[27] As the areas of steam dissipation are increased, the water evaporation rate of PPy origami is increased by at least 71% compared with that of a planar structure, reaching 2.12 kg m^{-2} h^{-1}, and the solar thermal energy conversion efficiency is 91.5% under one sun. Wang et al. demonstrated that the multilayer PPy nanosheets (Fig. 1-5), which spontaneously formed surface structures such as folds and ridges by continuous polymerization on the paper base, could significantly improve the broadband and wide-angle light absorption of the entire solar spectrum, and the solar-heat conversion efficiency can reach 95.33%.[28] The intriguing solar–thermal properties and structural characteristics of multi-layer PPy nanosheets can be used for solar heating and photo-actuators. At the same time, when it is used for solar steam generation, the measured efficiency could reach 92% under one sun irradiation.

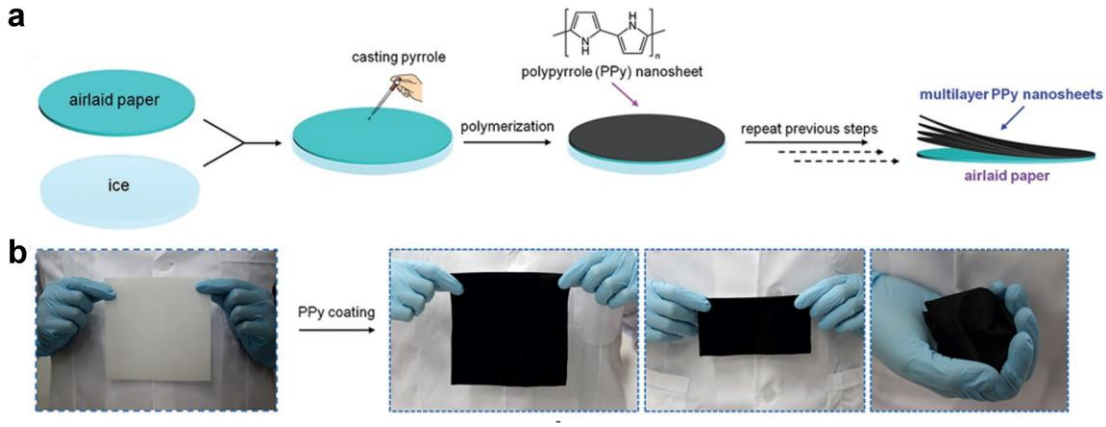

Fig. 1-5 (a) Schematic illustration of the overall preparation process toward multilayer PPy nanosheets by sequential polymerization. (b) Photos of the air-laid paper substrates before and after coating a layer PPy nanosheets.[28] Copyright 2019 Wiley-VCH.

Polyaniline (PANI). PANI is a well-known photo-thermal material with high stability, and it is widely used in solar steam generation. Zou et al. reported the direct fabrication of flexible and robust polymer composites for highly efficient solar evaporation based on PANI and hydrophilic polyvinylidene fluoride (PVDF) (Fig. 1-6).[29] The resulting PANI@PVDF composite devices demonstrated stretchable, durable, and tunable solar-thermal energy conversion features, which could achieve an excellent evaporation rate of 1.41 kg m^{-2} h^{-1} with efficiency of 85.0% under one sun illumination. Similarly, Peng et al. reported a vertically-aligned PANI nanofibers layer on the surface of a hydrophobic PVDF microfiltration membrane.[30] The excellent light trapping effect from the vertically arranged PANI nanofiber layer provides the photothermal membrane with high light absorption of up to 95% in the UV-visible range of the solar spectrum. The photothermal membrane showed performance with a distillation flux of 1.09 kg m^{-2} h^{-1} and a corresponding solar energy to-collected water efficiency as high as 74.15% under one sun irradiation.

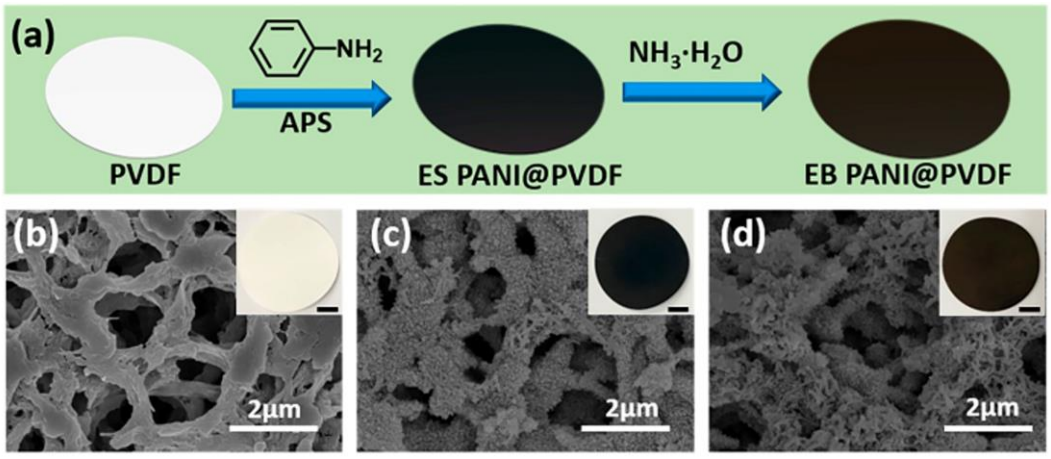

Fig. 1-6 (a) Schematic diagram of ES PANI@PVDF and EB PANI@PVDF composites,

and (b−d) the corresponding SEM images. [29] Copyright 2020 American Chemical Society.

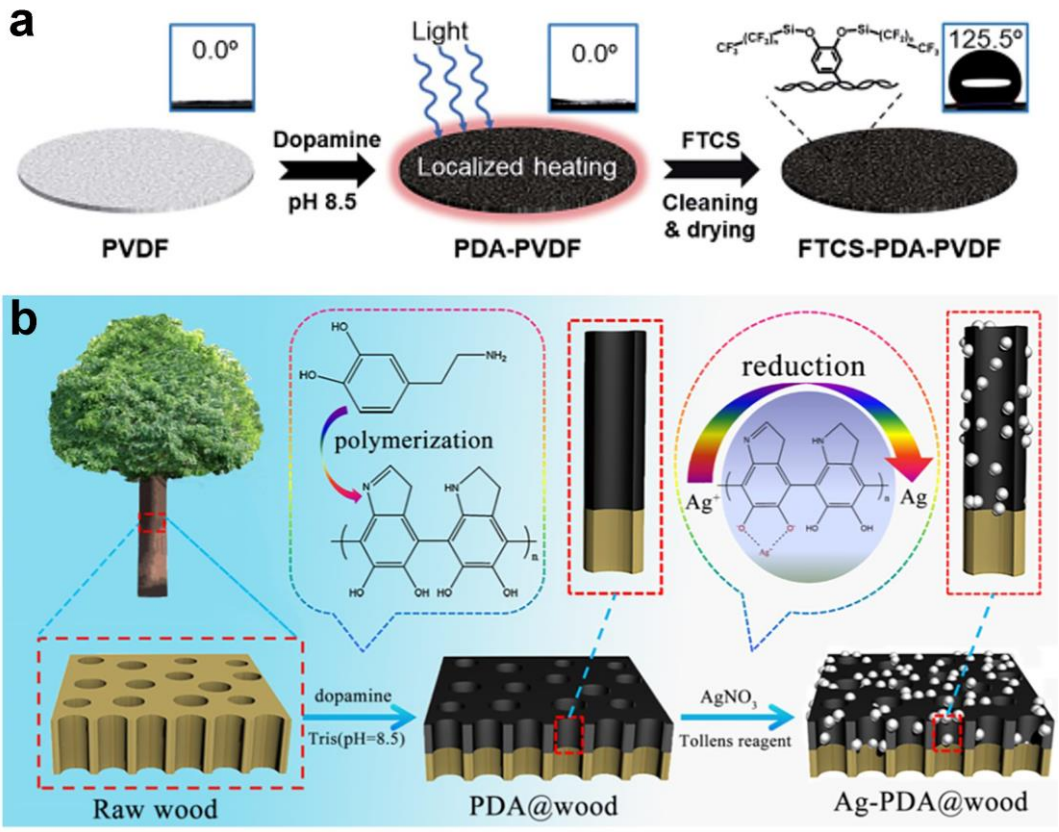

Fig. 1-7 (a) Schematic depicting the synthesis of the FTCS-PDA-PVDF membrane. (b) Schematic illustration of the fabrication process of Ag-PDA@wood. [31, 32] Copyright 2018 Royal Society of Chemistry and 2020 American Chemical Society, respectively.

Polydopamine (PDA). PDA has good photothermal characteristics and has been widely studied for water purification or desalination. Wu et al. demonstrated a simple, stable, and scalable PDA-coated PVDF membrane for highly efficient solar-driven membrane distillation (Fig 1-7a).[31] The membrane showed the best energy efficiency among existing photothermal membranes (45%) and the highest water flux (0.49 kg

m^{-2} h^{-1}) using a direct contact membrane distillation system under 0.75 kW m^{-2} solar irradiation. Yang et al. reported a simple dipping method, which prepared a new type of solar interfacial evaporation device by depositing silver nanoparticles (AgNPs) on natural wood (Fig 1-7b).[32] Owing to the synergistic photothermal effect between PDA and AgNPs, Ag-PDA@wood had an ultrafast solar-thermal response, and more heat was located at the interface. The natural wood layer with low thermal conductivity provides a sufficient water supply and reduces the bulk heat loss. A high evaporation rate of 1.58 kg m^{-2} h^{-1} was achieved and its evaporation efficiency reached 88.6%.

1.4.1.2 Polymeric hydrogel materials

Hydrogels are usually synthesized from monomers or polymers, and cross-linked networks are formed by physical interactions or chemical bonds. The polymer network of hydrogels can be adjusted by functional additives, monomer/polymer functional groups, crosslinking density, etc. Their micro or nano structure and surface morphology can also be customized by interface synthesis, freeze-drying, and surface coating. The adjustable synthesis and easy modification of hydrogel can meet the demanding requirements of a high-efficiency solar evaporator. Hydrogel-based solar evaporators can be formed by combining functional materials with photothermal conversion effects into hydrophilic polymer chains through in-situ polymerization. The uniform penetration of photothermal materials in the polymer network can limit the heat energy in the molecular network, thus reducing heat loss from bulk water. Hydrophilic polymer chains can capture water molecules, and water-polymer interactions contribute to the

activation of water. In addition, the molecular network acts as a water channel for transporting water to the evaporation surface, which has a significant influence on the water state and water transportation in the hydrogel. The energy required for the vaporization of water can be adjusted by the pore size. Therefore, with appropriate solar absorbers, material selection of hydrophilic polymer chains, and micro-nano surface design, hydrogels can be a promising material platform for efficient solar water purification.[6, 7, 33]

Typical polymer skeleton in hydrogel matrices, such as polyvinyl alcohol (PVA),[34, 35] poly(N-isopropylacrylamide) (PNIPAM),[36, 37] and polyacrylamide (PAM),[38, 39] have recently attracted much attention in solar evaporation applications. Because they have highly hydrophilic groups that strongly interact with water molecules, they are essential for the rapid transportation and retention of a large amount of water. Zhou et al. demonstrated a solar evaporator based on hydrogel, which can generate steam at a high rate of 2.5 kg m^{-2} h^{-1} under one sun irradiation.[40] This efficient solar evaporation is realized by the mixed hydrogel composed of a hydrophilic PVA and solar absorbent (reduced graphene oxide, rGO), which have internal capillary channels. (Fig. 1-8a) The PVA can greatly facilitate water evaporation owing to the reduced water evaporation enthalpy in the hydrogel network. The rGO penetrating the polymer network can efficiently utilize energy. The capillary keeps a sufficient water supply and continuously generates solar steam at a high rate. This hydrogel-based solar evaporator also shows good antifouling performance and can be desalted for a long time without recycling. Xu et al. developed a solar absorber gel (SAG), which consists of an

elastic thermal responsive PNIPAm hydrogel, a photothermal PDA layer, and a sodium alginate (SA) network (Fig. 1-8b).[41] All processing is aqueous-based and occurs at room temperature. It is worth noting that the SAG can purify all kinds of harmful reservoir water containing small molecules, oils, metals, and pathogens only by using sunlight. The SAG depends on solar energy to drive a hydrophilic/hydrophobic phase change at the lower critical solution temperature. Because the purification mechanism does not need water evaporation, it is an energy-intensive process, and the passive solar water purification rate is the highest reported. Sun et al. for the first time reported an inorganic-organic light-absorbing material, copper sulfide-macroporous polyacrylamide hydrogel (CuS-m-PAM).[42] The CuS-m-PAM was prepared by the in-situ synthesis method via loading CuS nanoparticles loaded into macroporous polyacrylamide hydrogel. CuS-m-PAM forms a heating zone at the air-water interface and CuS nanoparticles can efficiently convert the strongly absorbed light into localized heat, thus reducing the heat loss in the transfer process.

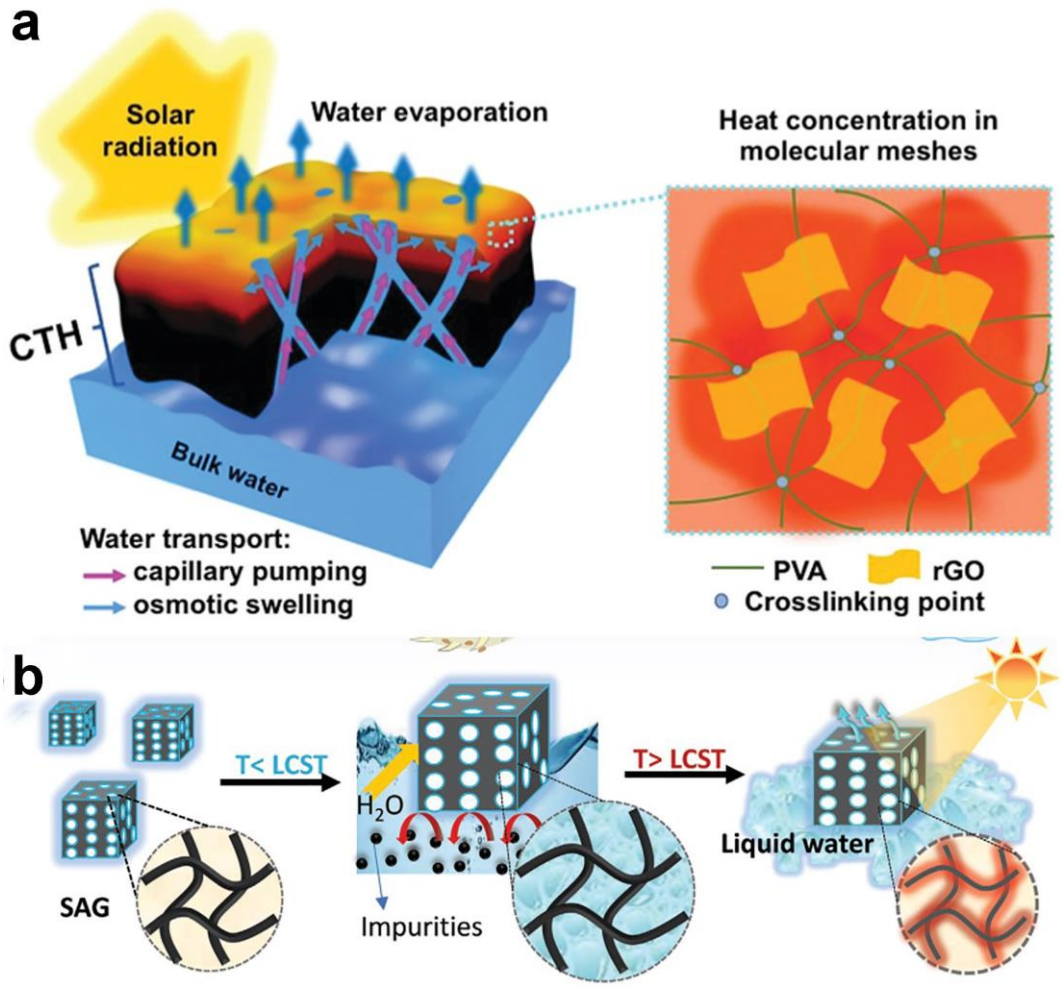

Fig. 1-8 (a) Schematic diagram of solar steam generation based on PVA-rGO hybrid hydrogel with capillarity facilitated water transport. (b) Inspired by the pufferfish, the SAG technology is based on the phase transformation (swelling and de-swelling) of PNIPAm under natural sunlight. [40, 41] Copyright 2018 Royal Society of Chemistry and 2021 Wiley-VCH., respectively.

1.4.1.3 Polymeric aerogels and foams

Foam, such as melamine foam (MF), polyurethane (PU) foam, and Polydimethylsiloxane (PDMS) foam, have attracted people's attention in the field of solar evaporation because of their porous structure and good thermal insulation

performance.[43-45] However, due to the poor light absorption ability of photothermal materials, in-situ modification of photothermal materials in foam materials is a commonly used research strategy.

Li et al. fabricated an expandable, low-cost, and durable bilayer polymer foam, which was used for efficient and stable solar steam generation.[46] With the bilayer structure, different functions are assigned to different layers, PPy coating pre-pressed MF has used light absorption and water evaporation, and the bottom pre-pressed MF layer for water transport and thermal insulation (Fig. 1-9a). A high average evaporation rate of 1.574 kg m^{-2} h^{-1} and an excellent steam generation efficiency of 90.4% under one sun were achieved. Bilayer foam demonstrated remarkable robustness and stability under a series of severe conditions, with long-term durability, excellent anti-fouling performance, and good reusability. Fan's group reported an innovative 3D solar evaporator assembled by carbon-molybdenum-disulfide, which provided synergistic and efficient removal of steam and heavy metal (Fig. 1-9b).[47] The mesoporous PU composite sponge can also be used as an independent reservoir, avoiding single-sided contact with a large amount of water, effectively suppressing the parasitic heat loss commonly observed, providing 88% high energy efficiency, and achieving the highest evaporation rates of 1.95 kg m^{-2} h^{-1} under one sun.

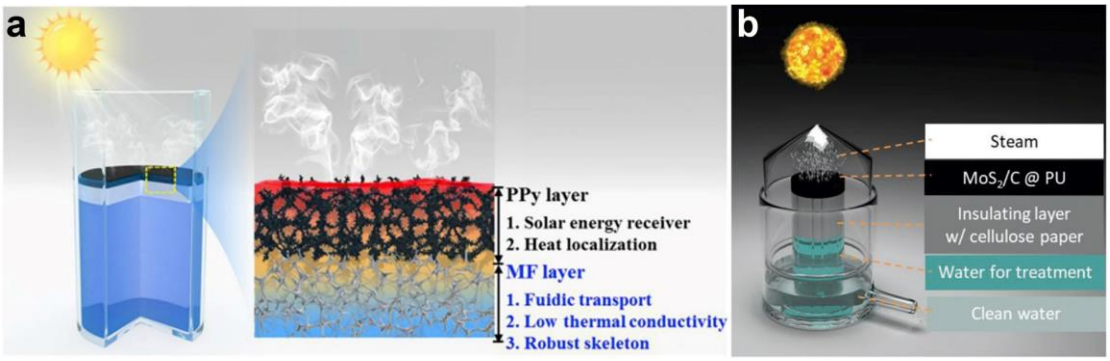

Fig. 1-9 (a) Schematic illustrations of PPy-MF bilayer polymer foam evaporator and the solar steam generation mechanism of the bilayer polymer foam. (b) Schematic of the design of the s MoS_2/C@PU solar steaming collection system. [46, 47] Copyright 2019 Elsevier, and 2019 Wiley-VCH., respectively.

Aerogel materials that are similar to foam in structure and function have also attracted attention. Aerogels are porous solid materials, such as inorganic aerogels, polymeric aerogels, and hybrid aerogels, made by forming a colloidal gel and then removing liquid from the pores of the gel. Among them, polymer aerogels have many advantages, such as multiple synthesis strategies, adjustable porous characteristics, customized physicochemical properties, inherent heat insulation properties, and their ultra-lightweight are suitable for water-air evaporation interfaces. It is self-floating, so it has advantages in the structure of the solar evaporator.

Yang et al. proposed a spectroscopic-specific solar aerogel inspired by the spectral selective sunlight utilization of plants.[48] It consists of a semiconductor D-HNb_3O_8 nanosheets rich in oxygen vacancy defects and a PAM skeleton, which realizes the integration of photochemical and photothermal solar energy conversion. The designed solar absorbent-polymer composite has good thermal insulation, reactant enrichment,

rapid mass diffusion, and capillary pumping characteristics, thus achieving efficient steam generation and photochemical activity. Han et al. prepared a PEDOT:PSS nanofibrillated cellulose aerogel employing to establish a high-performance solar steam generator.[49] The low density of the aerogel ensured minimal material requirements while simultaneously satisfying efficient water transport. Due to the high absorbance of the aerogel and the thermal-localization performance of the foam, the system exhibits a high evaporation rate of 1.61 kg m^{-2} h^{-1} under one sun irradiation, which is higher than most reported solar steam generation devices.

1.4.1.4 Fiber materials

The application of fiber-based materials in the field of photothermal evaporation has also been widely concerned. Fiber-based materials in the form of continuous filaments or porous matrices composed of fibers or nanofibers are commonly used to make clothing, filters, and passive cooling. Polymer material composed of fiber-matrix has been considered a favorable choice for photothermal evaporators due to its good mechanical stability, large-scale commercialization potential, and adjustable porous structure.

Chen's group fabricated the photothermal and superhydrophobic fabrics which can be produced on a large scale by a completely wet manufacturing strategy (Fig. 1-10a).[50] Through effective energy management, the limited heating strategy can significantly reduce heat conduction loss during the evaporation process. As a result, the evaporation rate can reach up to 1.49 kg m^{-2} h^{-1} with an evaporation efficiency of

91.68% under one sun irradiation. Similarly, Liu et al. designed and fabricated a hydrophilic, PANI-coated photothermal fabric (Fig. 1-10b).[51] In this study, the two ends of the fabric are designed to contact seawater, and the water flow is guided by capillary attraction. Both arc-shaped top/bottom surfaces of the hanging fabrics are exposed to air, which can prevent heat dissipation to bulk seawater and facilitate the double-surface evaporation upon sunlight irradiation. This study produced an effective evaporation rate of 1.94 kg m^{-2} h^{-1} and high solar efficiency of 89.9% in one sun irradiation.

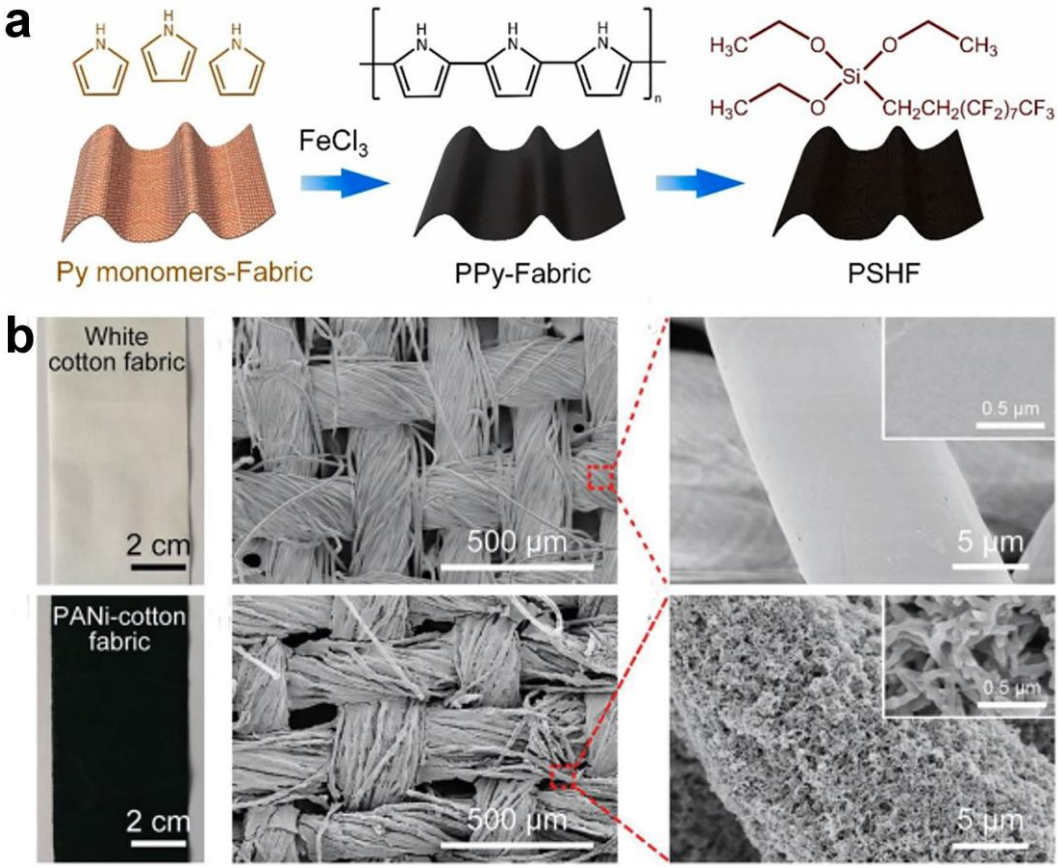

Fig. 1-10 (a) The fabricating process of superhydrophobic fabric. (b) Morphologies and SEM of the fabrics of the cotton fabric and PANI-cotton fabric. [50, 51] Copyright 2022 Elsevier and 2019 Wiley-VCH., respectively.

1.4.2 The application of seawater desalination

Seawater desalination is a process of removing minerals from seawater, and it is one of the most important and cheapest methods to obtain usable water so far. The interfacial solar-driven evaporation process has made great progress in the material design and system design of the absorber, which can realize large-scale and low-cost seawater desalination under standard sunlight. After solar seawater desalination, salinity in seawater is reduced, which can reach the reference water standard specified by the World Health Organization (1‰) and the U.S. Environmental Protection Organization (0.5‰). The interfacial solar-driven evaporation can make the seawater desalination devices portable, and provide enough water for individuals. For example, Yu's group demonstrated a hydrogel based on PVA and PPy, which can be used as an independent solar evaporator.[21] The converted energy can be used in-situ to drive the evaporation of seawater contained in the molecular meshes of the PVA network, in which the hydrogel skeleton promotes the evaporation of water. A floating hydrogel sample can obtain a record high evaporation rate of 3.2 kg m^{-2} h^{-1} and efficiency of 94% under 1 sun, and 18–23 kg m^{-2} per day of the hydrogel evaporator was gathered daily when purifying brine water. This material shows excellent desalting performance. Xia et al. designed a solar evaporator composed of a PVA cloth cylinder as the 2D water path and a circular carbon black coated PVA cloth disc as the evaporation layer. [52] By generating directional flow, accumulated salt is discharged through the discharge of concentrated brine. This approach is effective and applicable for brines with a broad range of concentration owing to their tuneable concentrating performance. With the

capability of continuously producing clean water and near-saturation brine, this research advances solar seawater evaporation technologies toward practical applications, such as brine concentration and resource recovery.

1.4.3 The application of wastewater purification

Another important application of the interface solar evaporation systems is the treatment of domestic and industrial wastewater. A solar desalination device is also used in wastewater treatment, including the removal of dye molecules, heavy metals, and oil-water separation. Zhao et al. have developed a hydrogel with intriguing evaporative properties by simply mixing and cross-linking poly (3,4 ethylene dioxythiophene):polystyrene sulfonate (PEDOT:PSS) nanofibrils and PVA viscous solutions.[53] The materials can effectively treat the wastewater containing heavy metals and printing and dyeing. Purified water collected from the bottom of the evaporation facility was tested to be effective in removing metal cations by 4 to 6 orders of magnitude, including the most common heavy metals cations such as Cu^{2+}, Zn^{2+}, Pb^{2+}, and Ni^{2+}, compared to the original wastewater. For wastewater containing organic pollutants, the purification effect was verified by adding common dyes MB (20 mg L^{-1}) and RhB (20 mg L^{-1}), and the water obtained from them could meet the drinking requirements set by the WHO. Kospa et al. demonstrated the combination of cheap semiconductor material with a porous ionic polymer (PIP), emeraldine salt (ES) form of PANI, as salt-resistant and oil-repellent evaporator, which was synthesized through a facile and cost-effective one-step method.[54] The composite showed a high oil contact angle in water (138.5°) and air (135.2°), and at the same time had high

hydrophilicity (8°), which proved the hydrophilicity and oleophobicity of the membrane. The results of this work indicated that the PANI-based membrane could exhibit a high evaporation rate despite the desalination of pure or oil-contaminated water. In addition, the authors have estimated the morphology of the pure water and oil-contaminated water by TOC test and optical microscopy, which is promising for oil-water separation applications.

1.5 Research topic and contribution of this dissertation

In recent years, the environmental problems caused by traditional energy sources have become increasingly prominent, and people begin to pay attention to the development and utilization of clean energy. Solar energy, as an inexhaustible clean energy source, has attracted people's attention. Among them, solar evaporation is a research field in which solar energy is used in the form of photothermal-steam conversion. The structure of the light absorber is the most important foundation for studying solar evaporation. PNPG is a conjugated conductive polymer with low cost of raw materials, various and simple synthesis methods, good chemical stability, and special optical properties. Among the many photothermal conversion materials in the field of solar evaporation of water, PNPG rarely attracts people to explore and study. Based on its numerous advantages, we think that PNPG can be used as an excellent photothermal conversion material for seawater desalination. This thesis takes the construction of a PNPG-based interfacial heating solar evaporation system as the starting point for research. The main research contents and significance are as follows:

In chapter 3, inspired by the amazon water lily, an interfacial water-trapped tridimensional structure solar evaporator was developed to achieve a continuous supply of water from the water-trapped layer and three-dimensional heat distribution management. The artificial photothermal membrane with PNPG can be easily prepared by vacuum filtration. Then, combined with the three-dimensional heat distribution management design and the water-trapped layer for a continuous supply of water, more optimized energy utilization and efficient interface heating were realized. Besides, because the novel nanoscale PNPG has excellent light capture performance and the absorbed solar energy can be concentrated in the water-trapped layer, which makes solar evaporation more effective. This special structure aims to minimize energy loss and better regulate the relationship between water evaporation, solar energy conversion, and heat regulation. Therefore, this low-cost, flexible and durable water collecting device is used for a long-term solar steam generator.

In chapter 4, to further explore the possibility of reducing the cost of the solar evaporator, a PNPG-wood solar evaporator was developed inspired by the transpiration process of trees. Compared with PVDF membrane, the price of wood blocks purchased in supermarkets is more competitive. PNPG coating greatly makes up for the weak light absorption of wood, and effectively improves the solar heat conversion efficiency. In addition, thanks to the low thermal conductivity and special microstructure of the wood, the relationship between water transportation, solar energy conversion, and heat regulation were better regulated. As a result, the PNPG-wood system can generate steam efficiently and quickly. Therefore, this solar evaporation system with reasonable

design, low cost, durability, and high efficiency has the potential to be applied to solve the practical problem of seawater desalination and water purification.

In chapter 5, to optimize solar-heat utilization efficiency and form, we prepared a synergistic photothermal layer from a PNPG/MoS_2 nanohybrid by the electrostatic induced assembly, which can be used for broad-spectrum and high-efficiency solar energy absorption. PNPG/MoS_2 system provided effective synergistic photothermal conversion and good water transmission, enabling solar steam to escape quickly. It is worth noting that the synergistic coupling of solar evaporation-thermoelectric (TE) power generation has also been realized, which provides more effective solar energy development. The high-performance PNPG/MoS_2 synergistic photothermal system developed in this study provides potential opportunities for coupling solar water purification and thermoelectric power generation to meet the demand of resource-scarce areas.

Reference

[1] J. Schewe, J. Heinke, D. Gerten, I. Haddeland, N.W. Arnell, D.B. Clark, R. Dankers, S. Eisner, B.M. Fekete, F.J. Colon-Gonzalez, S.N. Gosling, H. Kim, X. Liu, Y. Masaki, F.T. Portmann, Y. Satoh, T. Stacke, Q. Tang, Y. Wada, D. Wisser, T. Albrecht, K. Frieler, F. Piontek, L. Warszawski, P. Kabat, Multimodel assessment of water scarcity under climate change, Proc. Natl. Acad. Sci. U. S. A. 111 (2014) 3245-3250.

[2] C. Chen, Y. Kuang, L. Hu, Challenges and Opportunities for Solar Evaporation, Joule 3 (2019) 683-718.

[3] W. Shang, T. Deng, Solar steam generation: Steam by thermal concentration, Nat. Energy 1 (2016) 1-2.

[4] X. Min, B. Zhu, B. Li, J. Li, J. Zhu, Interfacial Solar Vapor Generation: Materials and Structural Design, Accounts of Materials Research 2 (2021) 198-209.

[5] X. Zhou, F. Zhao, P. Zhang, G. Yu, Solar Water Evaporation Toward Water Purification and Beyond, ACS Materials Letters (2021) 1112-1129.

[6] Y. Guo, J. Bae, Z. Fang, P. Li, F. Zhao, G. Yu, Hydrogels and Hydrogel-Derived Materials for Energy and Water Sustainability, Chem. Rev. 120 (2020) 7642-7707.

[7] X. Zhou, Y. Guo, F. Zhao, G. Yu, Hydrogels as an Emerging Material Platform for Solar Water Purification, Acc. Chem. Res. 52 (2019) 3244-3253.

[8] Z. Li, X. Xu, X. Sheng, P. Lin, J. Tang, L. Pan, Y.V. Kaneti, T. Yang, Y. Yamauchi, Solar-Powered Sustainable Water Production: State-of-the-Art Technologies for Sunlight-Energy-Water Nexus, ACS Nano 15 (2021) 12535–12566.

[9] G. Liu, T. Chen, J. Xu, G. Li, K. Wang, Solar evaporation for simultaneous steam

and power generation, J. Mater. Chem. A 8 (2020) 513-531.

[10] F. Zhao, Y. Guo, X. Zhou, W. Shi, G. Yu, Materials for solar-powered water evaporation, Nat. Rev. Mater. 5 (2020) 388-401.

[11] X. Li, T. Cooper, W. Xie, P.-C. Hsu, Design and Utilization of Infrared Light for Interfacial Solar Water Purification, ACS Energy Letters (2021) 2645-2657.

[12] P. Tao, G. Ni, C. Song, W. Shang, J. Wu, J. Zhu, G. Chen, T. Deng, Solar-driven interfacial evaporation, Nat. Energy 3 (2018) 1031-1041.

[13] M. Gao, L. Zhu, C.K. Peh, G.W. Ho, Solar absorber material and system designs for photothermal water vaporization towards clean water and energy production, Energy Environ. Sci. 12 (2019) 841-864.

[14] S. Karami, F. Arabpour Roghabadi, M. Maleki, V. Ahmadi, S.M. Sadrameli, Materials and structures engineering of sun-light absorbers for efficient direct solar steam generation, Solar Energy 225 (2021) 747-772.

[15] H.-H. Yu, L.-J. Yan, Y.-C. Shen, S.-Y. Chen, H.-N. Li, J. Yang, Z.-K. Xu, Janus Poly(Vinylidene Fluoride) Membranes with Penetrative Pores for Photothermal Desalination, Research 2020 (2020) 1-10.

[16] L. Zhang, B. Tang, J. Wu, R. Li, P. Wang, Hydrophobic Light-to-Heat Conversion Membranes with Self-Healing Ability for Interfacial Solar Heating, Adv. Mater. 27 (2015) 4889-4894.

[17] X. Li, G. Ni, T. Cooper, N. Xu, J. Li, L. Zhou, X. Hu, B. Zhu, P. Yao, J. Zhu, Measuring Conversion Efficiency of Solar Vapor Generation, Joule 3 (2019) 1798-1803.

[18] X. Hu, W. Xu, L. Zhou, Y. Tan, Y. Wang, S. Zhu, J. Zhu, Tailoring Graphene Oxide-

Based Aerogels for Efficient Solar Steam Generation under One Sun, Adv. Mater. 29 (2017) 201604031.

[19] X. Li, W. Xu, M. Tang, L. Zhou, B. Zhu, S. Zhu, J. Zhu, Graphene oxide-based efficient and scalable solar desalination under one sun with a confined 2D water path, Proc. Natl. Acad. Sci. U. S. A. 113 (2016) 13953-13958.

[20] Y. Li, T. Gao, Z. Yang, C. Chen, Y. Kuang, J. Song, C. Jia, E.M. Hitz, B. Yang, L. Hu, Graphene oxide-based evaporator with one-dimensional water transport enabling high-efficiency solar desalination, Nano Energy 41 (2017) 201-209.

[21] F. Zhao, X. Zhou, Y. Shi, X. Qian, M. Alexander, X. Zhao, S. Mendez, R. Yang, L. Qu, G. Yu, Highly efficient solar vapour generation via hierarchically nanostructured gels, Nat. Nanotechnol. 13 (2018) 489-495.

[22] D. Xie, M. He, X. Li, J. Sun, J. Luo, Y. Wu, F. Cheng, Tree-inspired efficient solar evaporation and simultaneous in-situ purification of ultra-highly concentrated mixed volatile organic wastewater, Nano Energy 93 (2022) 106802.

[23] C. Liu, Y. Peng, X. Zhao, Flower-inspired bionic sodium alginate hydrogel evaporator enhancing solar desalination performance, Carbohydr. Polym. 273 (2021) 118536.

[24] J. Li, C. Chen, W. Gan, Z. Li, H. Xie, M. Jiao, S. Xiao, H. Tang, L. Hu, A bio-inspired, hierarchically porous structure with a decoupled fluidic transportation and evaporative pathway toward high-performance evaporation, J. Mater. Chem. A 9 (2021) 9745-9752.

[25] L. Ji, L. Yan, M. Chao, M. Li, J. Gu, M. Lei, Y. Zhang, X. Wang, J. Xia, T. Chen,

Y. Nie, T. Chen, Sphagnum Inspired g-C3 N4 Nano/Microspheres with Smaller Bandgap in Heterojunction Membranes for Sunlight-Driven Water Purification, Small (2021) e2007122.

[26] H.-Y. Zhao, J. Zhou, Z.-L. Yu, L.-F. Chen, H.-J. Zhan, H.-W. Zhu, J. Huang, L.-A. Shi, S.-H. Yu, Lotus-Inspired Evaporator with Janus Wettability and Bimodal Pores for Solar Steam Generation, Cell Rep. Phy. Sci. 1 (2020) 100074.

[27] W. Li, Z. Li, K. Bertelsmann, D.E. Fan, Portable Low-Pressure Solar Steaming-Collection Unisystem with Polypyrrole Origamis, Adv. Mater. 31 (2019) 1900720.

[28] X. Wang, Q. Liu, S. Wu, B. Xu, H. Xu, Multilayer Polypyrrole Nanosheets with Self-Organized Surface Structures for Flexible and Efficient Solar-Thermal Energy Conversion, Adv. Mater. 31 (2019) 1807716-1807725.

[29] Y. Zou, X. Chen, W. Guo, X. Liu, Y. Li, Flexible and Robust Polyaniline Composites for Highly Efficient and Durable Solar Desalination, ACS Appl. Energy Mater. 3 (2020) 2634-2642.

[30] Y. Peng, Y. Wang, W. Li, J. Jin, Bio-inspired vertically aligned polyaniline nanofiber layers enabling extremely high-efficiency solar membrane distillation for water purification, J. Mater. Chem. A 9 (2021) 10678-10684.

[31] X. Wu, Q. Jiang, D. Ghim, S. Singamaneni, Y.-S. Jun, Localized heating with a photothermal polydopamine coating facilitates a novel membrane distillation process, J. Mater. Chem. A 6 (2018) 18799-18807.

[32] J. Yang, Y. Chen, X. Jia, Y. Li, S. Wang, H. Song, Wood-Based Solar Interface Evaporation Device with Self-Desalting and High Antibacterial Activity for Efficient

Solar Steam Generation, ACS Appl. Mater. Interfaces 12 (2020) 47029-47037.

[33] Y. Guo, G. Yu, Engineering Hydrogels for Efficient Solar Desalination and Water Purification, Accounts of Materials Research 2 (2021) 374-384.

[34] Y. Guo, X. Zhou, F. Zhao, J. Bae, B. Rosenberger, G. Yu, Synergistic Energy Nanoconfinement and Water Activation in Hydrogels for Efficient Solar Water Desalination, ACS Nano 13 (2019) 7913-7919.

[35] Y. Guo, H. Lu, F. Zhao, X. Zhou, W. Shi, G. Yu, Biomass-Derived Hybrid Hydrogel Evaporators for Cost-Effective Solar Water Purification, Adv. Mater. 32 (2020) e1907061.

[36] S. Cao, J. Jiang, Q. Tian, C. Guo, X. Wang, K. Dai, Q. Xu, Building of multifunctional and hierarchical HxMoO3/PNIPAM hydrogel for high-efficiency solar vapor generation, Green Energy & Environment (2020) 10.1016/j.gee.2020.1012.1012.

[37] H. Geng, Q. Xu, M. Wu, H. Ma, P. Zhang, T. Gao, L. Qu, T. Ma, C. Li, Plant leaves inspired sunlight-driven purifier for high-efficiency clean water production, Nat. Commun. 10 (2019) 1512.

[38] C.-S. Hu, H.-J. Li, J.-Y. Wang, A. Haleem, X.-C. Li, M. Siddiq, W.-D. He, Mushroom-Like rGO/PAM Hybrid Cryogels with Efficient Solar-Heating Water Evaporation, ACS Appl. Energy Mater. 2 (2019) 7554-7563.

[39] R. Li, Y. Shi, M. Alsaedi, M. Wu, L. Shi, P. Wang, Hybrid Hydrogel with High Water Vapor Harvesting Capacity for Deployable Solar-Driven Atmospheric Water Generator, Environ. Sci. Technol. 52 (2018) 11367-11377.

[40] X. Zhou, F. Zhao, Y. Guo, Y. Zhang, G. Yu, A hydrogel-based antifouling solar

evaporator for highly efficient water desalination, Energy Environ. Sci. 11 (2018) 1985-1992.

[41] X. Xu, S. Ozden, N. Bizmark, C.B. Arnold, S.S. Datta, R.D. Priestley, A Bioinspired Elastic Hydrogel for Solar-Driven Water Purification, Adv. Mater. (2021) e2007833.

[42] Y. Sun, J. Gao, Y. Liu, H. Kang, M. Xie, F. Wu, H. Qiu, Copper sulfide-macroporous polyacrylamide hydrogel for solar steam generation, Chem. Eng. Sci. 207 (2019) 516-526.

[43] S. Ma, C.P. Chiu, Y. Zhu, C.Y. Tang, H. Long, W. Qarony, X. Zhao, X. Zhang, W.H. Lo, Y.H. Tsang, Recycled waste black polyurethane sponges for solar vapor generation and distillation, Appl. Energy 206 (2017) 63-69.

[44] L. Zhu, T. Ding, M. Gao, C.K.N. Peh, G.W. Ho, Shape Conformal and Thermal Insulative Organic Solar Absorber Sponge for Photothermal Water Evaporation and Thermoelectric Power Generation, Adv. Energy Mater. 9 (2019) 1900250-1900256.

[45] F. Gong, H. Li, W. Wang, J. Huang, D. Xia, J. Liao, M. Wu, D.V. Papavassiliou, Scalable, eco-friendly and ultrafast solar steam generators based on one-step melamine-derived carbon sponges toward water purification, Nano Energy 58 (2019) 322-330.

[46] C. Li, D. Jiang, B. Huo, M. Ding, C. Huang, D. Jia, H. Li, C.-Y. Liu, J. Liu, Scalable and robust bilayer polymer foams for highly efficient and stable solar desalination, Nano Energy 60 (2019) 841-849.

[47] W. Li, M.C. Tekell, Y. Huang, K. Bertelsmann, M. Lau, D. Fan, Synergistic High-Rate Solar Steaming and Mercury Removal with MoS_2/C@Polyurethane Composite

Sponges, Adv. Energy Mater. 8 (2018) 1802108.

[48] M.Q. Yang, C.F. Tan, W. Lu, K. Zeng, G.W. Ho, Spectrum Tailored Defective 2D Semiconductor Nanosheets Aerogel for Full-Spectrum-Driven Photothermal Water Evaporation and Photochemical Degradation, Adv. Funct. Mater. 30 (2020) 2004460.

[49] S. Han, T.P. Ruoko, J. Gladisch, J. Erlandsson, L. Wågberg, X. Crispin, S. Fabiano, Cellulose-Conducting Polymer Aerogels for Efficient Solar Steam Generation, Adv. Sustain. Syst. 4 (2020) 2000004.

[50] C. Zhang, P. Xiao, F. Ni, J. Gu, J. Chen, Y. Nie, S.-W. Kuo, T. Chen, Breathable and superhydrophobic photothermic fabric enables efficient interface energy management via confined heating strategy for sustainable seawater evaporation, Chem. Eng. J. 428 (2022).

[51] Z. Liu, B. Wu, B. Zhu, Z. Chen, M. Zhu, X. Liu, Continuously Producing Watersteam and Concentrated Brine from Seawater by Hanging Photothermal Fabrics under Sunlight, Adv. Funct. Mater. 29 (2019) 1905485.

[52] Y. Xia, S. Yuan, Y. Li, L. Gao, X. Zhang, Solar-driven brine desalination and concentration by controlled salt excretion, EcoMat 3 (2021) 12143.

[53] Q. Zhao, J. Liu, Z. Wu, X. Xu, H. Ma, J. Hou, Q. Xu, R. Yang, K. Zhang, M. Zhang, H. Yang, W. Peng, X. Liu, C. Zhang, J. Xu, B. Lu, Robust PEDOT:PSS-based hydrogel for highly efficient interfacial solar water purification, Chem. Eng. J. 442 (2022) 136284.

[54] D.A. Kospa, A.I. Ahmed, S.E. Samra, S.A. El-Hakam, A.A. Ibrahim, Flexible CuO-rGO/ PANI thermal absorber with high broadband photoresponse and salt

resistance for efficient desalination of oil-contaminated seawater, Desalination 528 (2022) 115612.

Chapter 2 Materials, experimental methods, and characterizations

2.1 Materials

2.1.1 Chemical reagents

N-phenylglycine (NPG, >97.0%) was bought from Tokyo Chemical Industry (Japan). High Purity Materials Kojundo Chemical Lab Co., Ltd (Japan) provided MoS_2 powder (99.9%). Tannic acid (TA, ≤100%), H_2SO_4 (98%), HCl (35.0~37.0%), ammonium persulfate (APS, 98.0%), sodium chloride (NaCl, 99.0+%), phenol (99.0+%), methylene blue (MB, 98.5%), methyl orange (MO, ≤100%), and rhodamine B (RhB, ≤100%) were provided by Fujifilm Wako Pure Chemical (Japan). Ultrapure water was supplied by the lab. All of the reagents were applied directly in the following experiments.

2.1.1 Other materials

Polyvinylidene fluoride (PVDF, hydrophilic) filter has pores not larger than 220 nm and was obtained from Merck Millipore (USA). Wood materials were purchased from a local market and then cut into the size of 3 cm × 3 cm × 1 cm (length × width × height) with the growth direction. Natural seawater was collected from the Sea of Japan.

2.2 Experimental methods

2.2.1 Preparation of PNPG nanoparticles

PNPG was prepared by polymerization from the NPG monomer. In brief, NPG

was dissolved in 50 mL acid solution (HCl or H_2SO_4) and stirred thoroughly at room temperature for 10 min. The initiator APS was dissolved in 50 mL acid solution with ultrasonication. The APS solution was added to the NPG solution. The polymerization process was performed using an ice-water bath method for 24 h. The prepared sample was washed several times with ultra-pure water to remove impurities, and the PNPG was re-dispersed into the water with ultrasonication and kept at 4 ℃.

2.2.2 Preparation of MoS_2 nanosheets

The aqueous exfoliation process of MoS_2 was performed with the assistance of TA using a 250 W ultrasonic cell crusher (Branson Sonifier 250, USA). Briefly, 120 mg of MoS_2 powder was added to 60 mL (1.0 mg L^{-1}) aqueous TA solution, and the suspension was sonicated for 3 h. Finally, the MoS_2 nanosheets in the supernatant were collected after 15 min centrifugation at 3000 rpm to remove the MoS_2 bulk. Ultrapure water was used in the exfoliation experiments to prevent the aggregation of the exfoliated nanosheets.

2.2.3 Experiment for solar desalination

The interfacial solar evaporation with mass and temperature changes was measured at 1 sun by the XES-40S3-TT solar simulator (SAN-EI Electric, Japan). The indoor temperature and humidity were kept at 25 °C and 60% during the experiments, respectively. The water mass changes used to calculate evaporation rates and solar-heat efficiency were recorded in real-time by an FX-200GD balance with an accuracy of 0.001 g (A&D Company, Japan).

The following equation was used to calculate the energy efficiency (η) of the

interface solar evaporation process:

$$\eta = (m_1\text{-}m_0)h_v/C_{opt}P_0 \quad (1)$$

where m_1 (units: kg m^{-2} h^{-1}) represents the interface solar evaporation rate, m_0 (units: kg m^{-2} h^{-1}) is the dark natural evaporation rate, h_v (units: kJ kg^{-1}) donates to the liquid-vapor phase transition enthalpy, C_{opt} is the optical density, and P_0 (units: W m^{-2}) donates to the power density of one sun illumination.

Corresponds with the real-time evaporation rates V_e of solar evaporation systems were determined by the below equation:

$$V_e = dm/(S \times dt) \quad (2)$$

where dm is the water weight change per minute, S donates the area of the PNPG wood device, and t donates the solar illumination time.

2.3 Characterizations

2.3.1 Scanning electron microscopy (SEM)

Before sample testing, gold spraying is performed using an ion sputterer (E-1030; Hitachi, Japan) to enhance the conductivity of the sample surface. Afterward, morphological analysis is performed using SEM (Hitachi S-4300, Japan).

2.3.2 Transmission electron microscopy (TEM)

Microscopic morphologies of nanomaterials were taken by TEM (Hitachi HT-7700, Japan).

2.3.3 Fourier transform infrared spectroscopy (FTIR)

The chemical functional groups of the samples were confirmed by FTIR (PerkinElmer Spectrum Two N, USA) using KBr pellets.

2.3.4 X-ray diffractometer (XRD)

XRD patterns were recorded on a Rigaku-D/MAX 2500v/pc diffractometer (Rigaku, Japan).

2.3.5 Contact angles

Contact angles were measured on a conventional system (DMs-401, Kyowa Interface Science Co., Ltd., Japan) at room temperature with a 3 μL droplet as the indicator.

2.3.6 Zeta potential

The zeta potential was recorded by a zeta potential analyzer (Zeta Plus, Brookhaven Instruments, USA).

2.3.7 Inductively coupled plasma atomic emission spectroscopy (ICP-AES)

The ion concentrations in seawater and distilled water were tested with the help of Shimadzu ICPE-9000 (Japan)

2.3.8 UV-vis-NIR spectra

The UV-Vis-NIR absorption spectra were collected on a spectrophotometer (UV-3600, Shimadzu, Japan).

2.3.9 Thermal imagery

The temperature change and IR images under different conditions were monitored

by a thermal imager (FLIR One Pro, USA), and the IR images were edited by the software FLIR Tools.

Chapter 3 Poly(N-phenylglycine)-based bioinspired system for stably and efficiently enhancing solar evaporation

3.1 Introduction

In recent decades, seawater desalination has become a viable solution to water shortage. However, the traditional methods of seawater desalination expend needed vast energy and operating costs, which run counter to the sustainable development goals (SDGs).[1-4] For the past few years, solar evaporation has attracted much attention because of its fast evaporation rate and small carbon footprint.[5-8] Thus, due to the complexity and high cost associated with the required high optical density, it is particularly important to develop a cheap and easily available solar-thermal conversion material.[5,7-10] So far, several materials with broad and powerful full solar absorption characteristics and stable energy conversion performance, such as noble metal nanomaterials,[11-13] carbon-based materials,[14-16] semiconductor materials,[17,18], etc., have been used for solar desalination. Although the development of these materials has made great progress, the exploration of practical strategies still faces several problems, including high cost, frangibility, inefficiency, and complicated manufacturing processes. For example, carbon nanomaterials and noble metals nanomaterials are generally expensive and hard to be large-scale used.[19] In addition, the metal-base nanomaterials mainly rely on the narrow absorption bandwidth of localized surface plasmon resonance (LSPR) effects,[20] which further limits their

application in this field. To solve these challenges, polymer materials have received a lot of attention in recent years for manufacturing high-performance solar absorbers due to the advantages of simple preparation method, low cost, high light-to-heat conversion efficiency, durability, and light weight.[7, 21] The development of this kind of materials provides more choices in the facile fabrication of high-performance solar steam generators, and is expected to have a scalable application in solar desalination.[22-24]

Poly(N-phenylglycine) (PNPG), an analog of polyaniline (PANI), as a part of the photothermal polymer category with outstanding light absorption was used in cancer phototherapy.[25-27] In recent years, phototherapy polymers, such as PANI, polydopamine (PDA) and polypyrrole (PPy), etc. have been widely applied in solar desalination.[28-30] Similar to the above-mentioned, PNPG has several remarkable characteristics, such as high-efficiency photothermal conversion performance, low toxicity, good biocompatibility, and large-scale preparation, which make it an outstanding candidate material for solar evaporation. Moreover, compared with plasmon metals and graphene materials, PNPG is more cost-competitive in the large-scale application of solar evaporation. In addition, since its low toxicity has been demonstrated in previous studies, PNPG will not introduce harmful substances into purified water in the process of solar desalination.[27, 31] However, as a completely new branch for the solar-thermal application, PNPG has not been used for solar evaporation.

The structure of devices is another challenge to be solved in the process of solar evaporation. It is reported that different device structures have a great influence on

evaporation performance. Recently, researchers have studied different dimensionality to better adjust the relationship between water evaporation, solar conversion, and thermal regulation.[32-36] These results confirm that in addition to selecting high-efficiency photothermal materials, it is equally important for a researcher to consider water delivery balance, water content, and thermal insulation as the principles of designing solar evaporators.[37-40] In this regard, nature often brings a lot of inspiration for building high-performance devices. For example, Yu et al. developed a lotus morphology-inspired solar evaporator modified by PDA for high-speed and persisting water evaporation.[41] Song *et al.* built a high-efficiency biomimetic 3D evaporator, which imitated the unique water transpiration characteristics of the peristome surface of the pitcher plant and the bird's beak.[42] Here, the Amazon water-lily (Scheme 1) has a versatile water transmission and transpiration system. First, the top surface absorbs solar light and provides stomas for steam to escape. Meanwhile, the hydrophobic top surface has the nature of self-cleaning. Secondly, Amazon water-lily can naturally float on water because the air chamber and the thick cane stems on the back of the leaves strongly support the leaves. Thirdly, there is a confined water channel provided by the bundle vessels to pump water and distribute it to the large-surface leaves of Amazon water lily. Based on the enlightenment of the above properties, in this work, an interfacial water-trapped tridimensional structure (IWTS) device inspired by the Amazon water lily was developed, which performs stable solar evaporation.

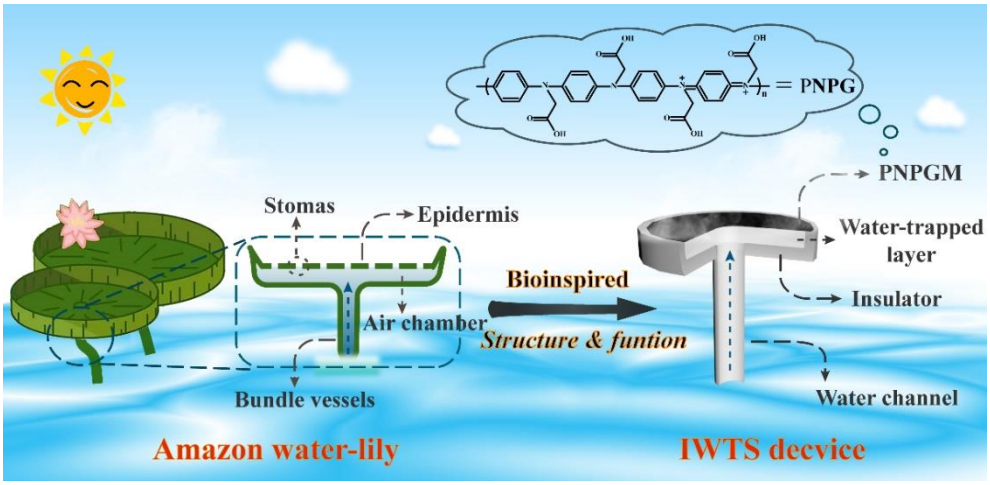

Scheme 3-1 Schematic Illustration of natural Amazon water-lily and bio-inspired IWTS device.

The IWTS device has a morphology-inspired structure and similar functional features to the Amazon water lily (Scheme 3-1). It consists of a novel nanoscale PNPG-based solar absorber on the top side, a thermal insulation layer at the bottom, a water-trapped layer embedded in the insulation module, and a confined water channel. Different from most of the previous studies, water can only flow through a narrow channel just like the Amazon water lily. And water will be trapped in the layer between the top hydrophobic solar absorber and the bottom thermal insulator like a sandwich instead of water directly getting into the absorber. The nanoscale solar absorption mainly takes place on the water-trapped layer, which minimizes the loss of heat conduction and light absorption and plays a significant role in effective light absorption. In the meanwhile, the microscale stomata of the absorber provide a way for steam to escape. Besides, the thermal insulation layer supports the whole device so that it can naturally float on water. The special structure is designed to minimize the loss of energy

and better adjust the connection between water evaporation, solar conversion, and thermal regulation. Thus, this low-cost, flexible, durable water-trapped device is used for a long-term solar steam generator.

3.2 Experimental

3.2.1 Reagents and materials

Polyvinylidene fluoride (PVDF, hydrophilic) filter has pores not larger than 220 nm and was obtained from Merck Millipore. N-phenylglycine (NPG) was provided by Tokyo Chemical Industry Co., Ltd. (Japan). Sulfuric acid (H_2SO_4), ammonium persulfate (APS), and sodium chloride (NaCl) were obtained from Fujifilm Wako Pure Chemical Corporation (Japan). Ultrapure water was supplied by the lab. All of these reagents are used without further purification.

3.2.2 Preparation of IWTS device

The PNPG can be polymerized from NPG monomer according to the research of Shen's group.[31] The detail of the synthetic operation is as follows: Mixing NPG (1.06 g) with 0.1 M H_2SO_4 (50 mL), and well stirring it at room temperature for 10 min. Then, mix APS (1.60 g) and 0.1 M H_2SO_4 (50 mL), and dropwise add it into the above NPG solution. The whole experiment process was in ice-water bath condition for 24 h, and the black suspension was formed. This resulting suspension was filtered and washed with ultrapure water to eliminate impurities and then re-dispersed in ultrapure water for later use.

PNPG membrane (PNPGM) solar absorber, formed by PNPG suspension, was

fabricated on PVDF by vacuum filtration. The obtained PNPGM was dried at room temperature all night. After drying completely, the membranes were successful in preparation. Then, a simple IWTS device was assembled using a PNPGM absorber, and a thermally insulated polystyrene foam with a small drilled hole that was filled with a cotton water-trapped layer connected with a cotton water supply channel.

3.2.3 Characterization

Scanning electron microscopy (SEM) images and transmission electron microscope (TEM) photos were taken by Hitachi S-4300 and Hitachi HT-7700, respectively. The UV-vis-NIR absorption spectra were collected on a spectrophotometer (UV-3600, Shimadzu, Japan). FT-IR spectra were recorded on PerkinElmer Spectrum Two N. Contact angles were measured on a conventional system (DMs-401, Kyowa Interface Science Co., Ltd., Japan) at room temperature with a 3 μL droplet as the indicator. The temperature change and IR images under different conditions were taken using a FLIR thermal imager. The concentration of metal ions can be determined with the help of inductivity coupled plasma optical emission spectrometer measurements (ICPE-9000, Shimadzu, Japan). The salinity was analyzed using a LAQUAtwin salinity meter (Salt-22, HORIBA Scientific, Japan).

3.2.4 Experimental setup for solar desalination

A solar simulator (XES-40S3-TT, SAN-EI Electric Co., Ltd., Japan) with the standard AM 1.5G solar spectrum was applied to the solar evaporation and wastewater treatment. The indoor temperature was carefully kept at approximately 24 °C and humidity 60 % during the experiments. Evaporation rate and energy efficiency were

calculated by the mass change of water recorded using a high-accuracy balance (FX-200GD, A&D Company, Limited, Japan) in real-time.

The solar-thermal conversion efficiency (η) was determined by using the following equation:

$$\eta = \frac{(m - m_0) h_V}{C_{opt} P_0} \quad (1)$$

where m is the solar evaporation rate, m_0 is the natural evaporation rate in dark, h_v is the enthalpy of liquid-vapor phase change,[43] C_{opt} is the optical concentration, and P_0 is the power density of 1 sun irradiation.

3.3 Results and discussion

3.3.1 Fabrication and characterization of PNPG-based device

The bio-inspired high-performance PNPG-based solar steam generation device was realized in this work, which was customizable and scalable, with high efficiency and durable performance. PNPG was synthesized under the following process: NPG was dissolved in H_2SO_4 solution, and then the initiator APS solution was dropwise added under an ice-water bath. After 24 h the PNPG was formed. (Fig. 3-1a) In the next step, the PNPG suspension was assembled to form the PNPGM solar absorber by vacuum filtration. And then the photothermal membrane was formed after natural dry overnight. The obtained PNPGM was used to build the solar steam generation device for subsequent solar evaporation. (Fig. 3-1b).

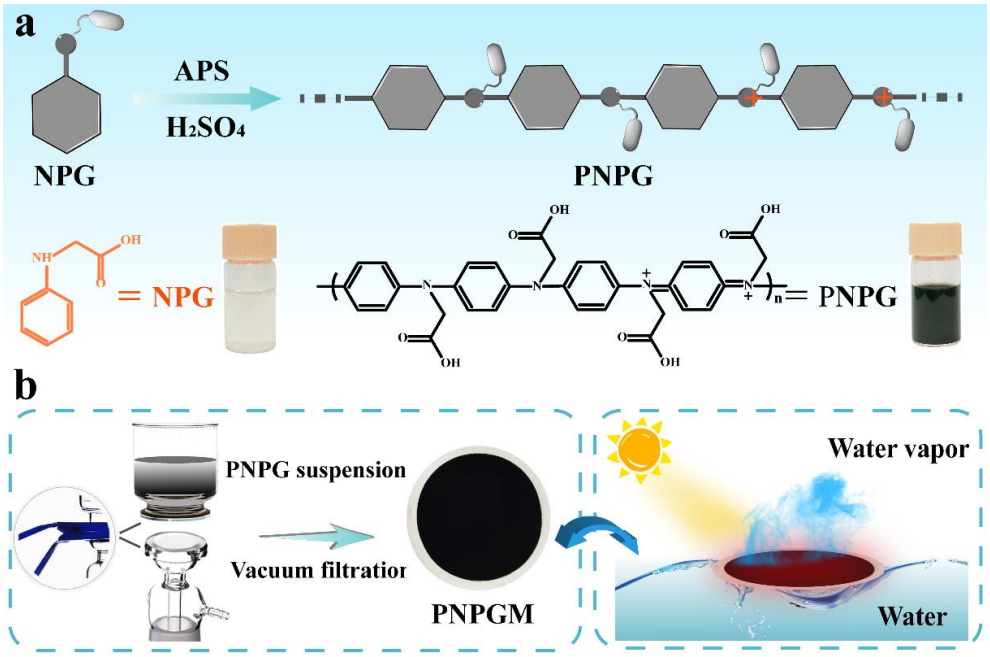

Fig. 3-1 (a) Schematic diagram of the synthetic process of PNPG (simplified the counterions). Inset: photos of NPG water solution and PNPG suspension, respectively. (b) Preparation of the PNPGM and the PNPGM-based solar evaporation system.

To observe the size and morphology features of PNPG, a transmission electron microscope (TEM) was employed to characterize the stability and uniformly. It found that the PNPG had uniform distribution morphology and good monodispersity (Fig. 3-2a and Fig. 3-3a). The size distribution of PNPG is determined according to the corresponding statistical data shown in the inset of Fig. 3-2a, the average size is found to be around 120 nm, which is consistent with the Gaussian distribution. Then, PNPG nanoparticles were deposited on PVDF by vacuum filtration method, and a 4~6 μm thin top photothermal layer was formed (Fig. 3-2b and c). Compared with the original PVDF (Fig. 3-3b), PNPGM still maintains the morphology of a good porous structure (Fig. 3-2d and e). It is worth noting that such interconnected pores can be used as water

vapor transmission channels, similar to the pores on the surface of water lilies, which is beneficial for effective evaporation applications. In addition, PNPGM can be curled very well, which proves its stable and flexible property (Fig. 3-2f). Thus, the durability of solar evaporation is guaranteed.

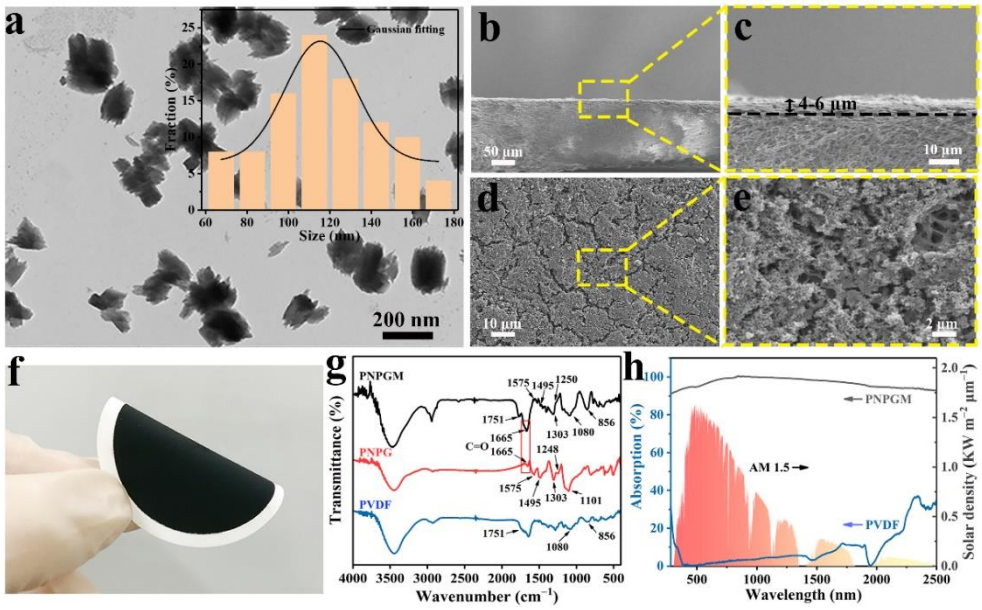

Fig. 3-2 (a) TEM image of PNPG nanoparticles. Inset: its corresponding size distribution. (b) SEM images of the upper surface of PNPGM and (c) a magnified image of the structure in (b). (d) SEM image of the vertical cross-section of PNPGM and (e) a magnified image show 4-6 μm thickness of PNPG coating. (f) The photograph of a bent PNPGM. (g) FT-IR spectra of PVDF, pure PNPG, and PNPGM, respectively. (h) UV-Vis-NIR spectra of original PVDF, PNPGM, and the normalized AM 1.5G spectral solar density (the pink area).

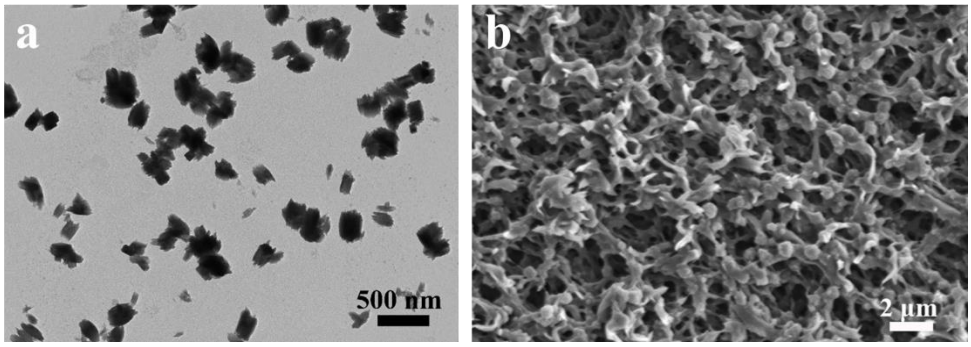

Fig. 3-3 (a) TEM image of PNPG nanoparticles. (b) SEM image of PVDF membrane.

The chemical functional groups of PVDF, pure PNPG, and PNPGM are shown in FT-IR spectra (Fig. 3-2g). For PNPGM, the bands at 1575 and 1495 cm^{-1} were attributed to stretching vibrations of the quinonoid and benzenoid structure of PNPG. The peaks located at 1303 cm^{-1} and 1250 cm^{-1} were related to C–N stretching vibration.[27, 31] The stretching vibration absorption of C=O in PNPG is located in 1665 cm^{-1}, which is in the same location as PNPGM. It can also be obtained that most absorption peaks in PVDF were reserved in the PNPGM, such as 856, 1080, and 1751 cm^{-1}. All these observations indicated that the PVDF surfaces were successfully covered by PNPG nanoparticles.

The performance of IWTS devices depends to a large extent on the photothermal conversion capability of PNPGM. The solar light absorption capability of the PNPGM is determined based on the ultraviolet-visible-near infrared (UV-vis-NIR) spectrum. As shown in Fig. 3-2h, because the blank PVDF membrane reflects most of the impacting solar radiation, the original PVDF membrane has a weak solar light absorption capacity (PNPG 0 mg). After coating with the PNPG, the totality light absorption rate of PNPGM significantly increase (PNPG 10 mg), and solar light on PNPGM can be almost

absorbed completely. This enhancement is owed to the effective photothermal conversion of PNPG coating, which also fully confirmed the previously mentioned concentrating light energy on the top thin PNPG layer. Considering that further increasing the quality of the PNPG coating can improve the total absorption, however, the excessively thick coating will lead to a decrease in the stability and durability of the material itself. Therefore, the coating mass of 10 mg is used to balance the relationship between durability and efficiency, and as a follow-up research standard.

3.3.2 Evaporation acceleration by IWTS system

The surface wettability of the photothermal membrane is related to water transport, which is one of the significant factors affecting effective solar evaporation. Water droplets (3 μL) were dropped on the PVDF membrane and the top side and backside of PNPGM to measure their wettability (Fig. 3-4 and Fig. 3-5a). The pristine PVDF membrane exhibits good hydrophilicity, which is revealed in its water contact angle of 0°. The contact angle of the water droplets on the top side and backside of the PNPGM is 94° and 0° after 10 s, respectively. On one hand, the good hydrophilicity of the backside of PNPGM can be sufficient and fast water supply to ensure the interface evaporation. On the other hand, the hydrophobicity of the top side of PNPGM is also critical because it resists pore wetting, which ensures that only vapor passes through the membrane pores enhancing the solar desalination performance. Immediately after the PNPGM is positioned over the water-trapped plate, water will quickly diffuse from the initial contact position till it covers the full of the membrane, the total time of the whole process is within 5 s (Fig. 3-5b). Therefore, all the above results show that water

can be continuously and effectively transferred to the PNPGM to avoid direct contact with bulk water, which is beneficial for solar evaporation.

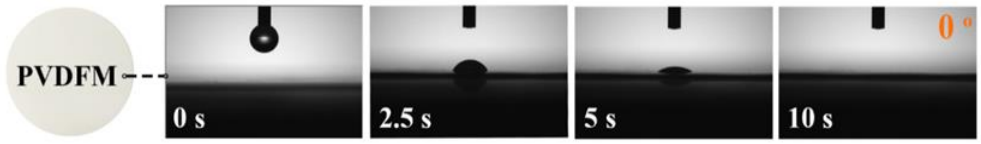

Fig. 3-4 Water contact angles of pure PVDF membrane.

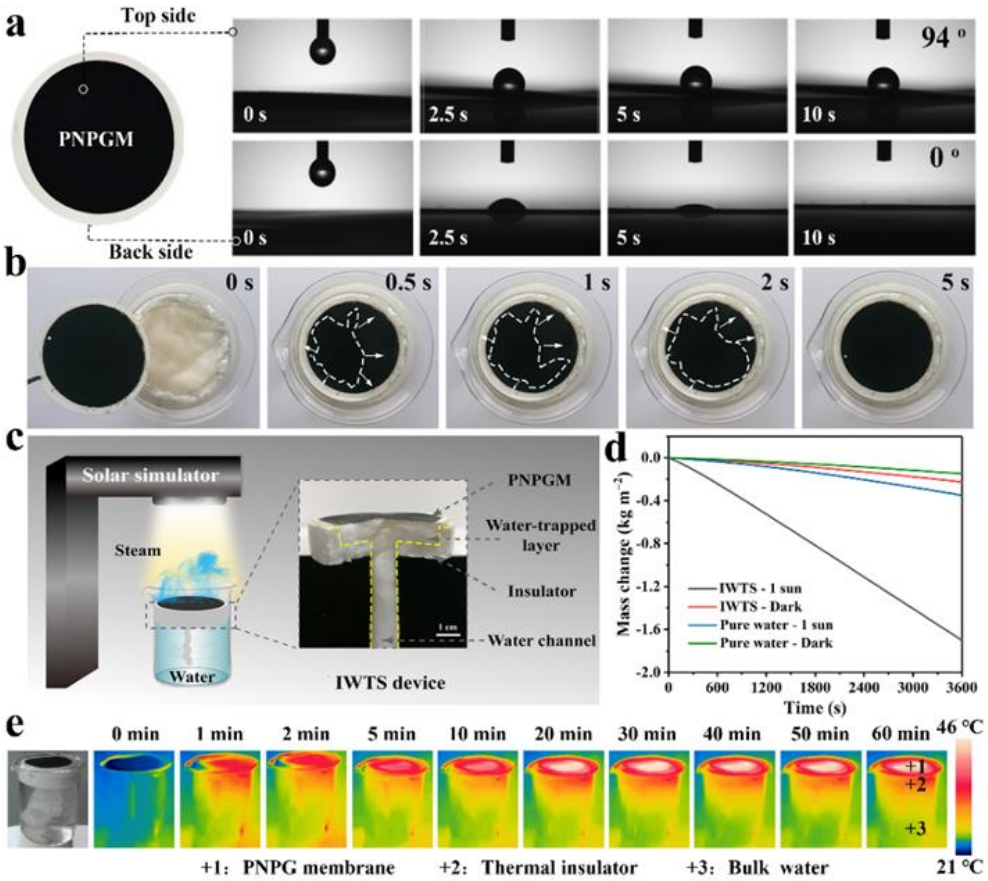

Fig. 3-5 (a) Water contact angles of the top side and backside of PNPGM. (b) Time-dependent wetted area of the PNPGM. (c) Schematic diagram of the IWTS system and the internal structure of the IWTS device. (d) Water mass change curves of IWTS system and pure water with and without solar irradiation. (e) The temperature infrared images of the IWTS solar evaporation system at different time points.

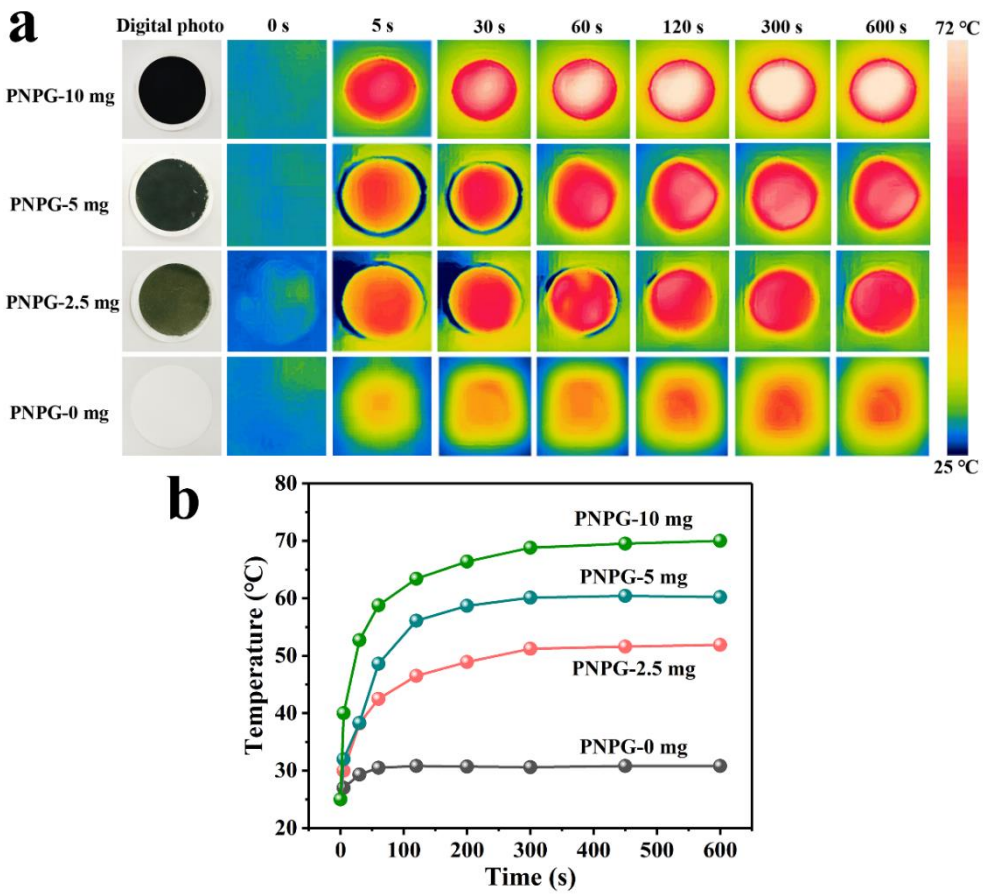

Fig. 3-6 (a) IR mapping images (b) and the corresponding temperature curves of the PNPGM with 0 mg, 2.5 mg, 5 mg, and 10 mg coating mass under 1 sun illumination at different time points.

Encouraged by the high-effective absorption of the black polymer, PNPGM with different coating mass was exposed to simulated solar radiation to explore the solar-thermal behavior (1 kW m^{-2}) (Fig. 3-6). Because of the exciting light absorption capacity, the temperature of the PNPGM rises rapidly after irradiation and reaches a stable state after 300 s. The coating mass also affects the photothermal effect, PNPG-10 mg can reach a high temperature of 72 °C after 600 s of illumination. In contrast, the

thermal effect of the blank PVDF under the same irradiation conditions is negligible.

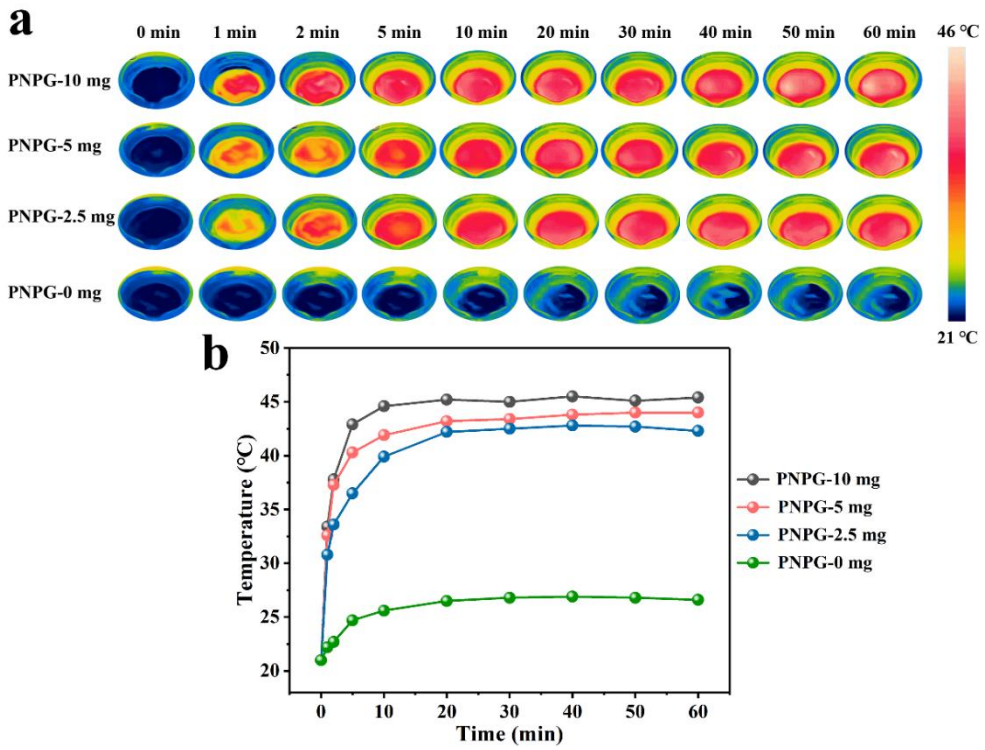

Fig. 3-7 (a) IR mapping images (b) and the corresponding temperature curves of the top view of the IWTS device with 0 mg, 2.5 mg, 5 mg, and 10 mg coating mass of PNPG under 1 sun illumination at different time points, respectively.

The PNPGM with excellent solar-thermal behavior and water transport capacity is further assembled into a device. As shown in Fig. 3-5c, an IWTS device is designed. Based on PNPGM solar absorber, PS foam is used as a thermal insulation layer. Then, by embedding cotton pieces as a water-trapped layer in the PS foam, which can effectively lock a large amount of water and continuously supply water to the PNPGM, the cotton rob water channel will continuously deliver water and stored it in the water-trapped layer. When the IWTS device is floated on the water surface, water is

effectively pumped in by capillary force. It not only can efficiently supply water but also prevent a large amount of thermal diffusion into bulk water. Therefore, this solar desalination device has the advantage of low cost, which is potentially applied to actual solar evaporation.

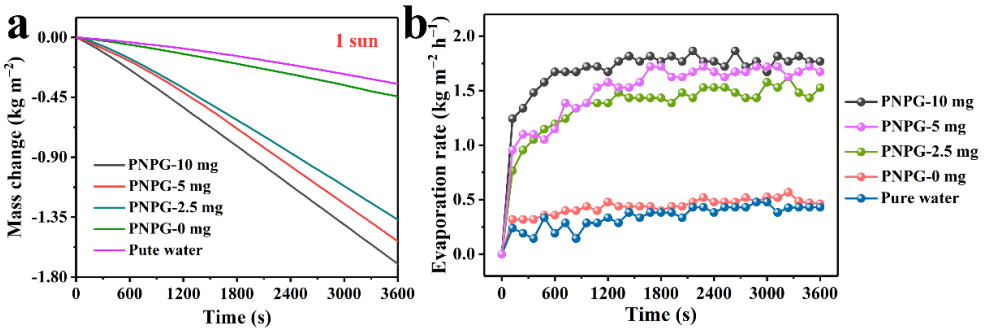

Fig. 3-8 (a) Water mass change curves (b) and the corresponding water evaporation rate curves of pure water and the IWTS device with 0 mg, 2.5 mg, 5 mg, and 10 mg coating mass of PNPG under 1 sun illumination at different time points, respectively.

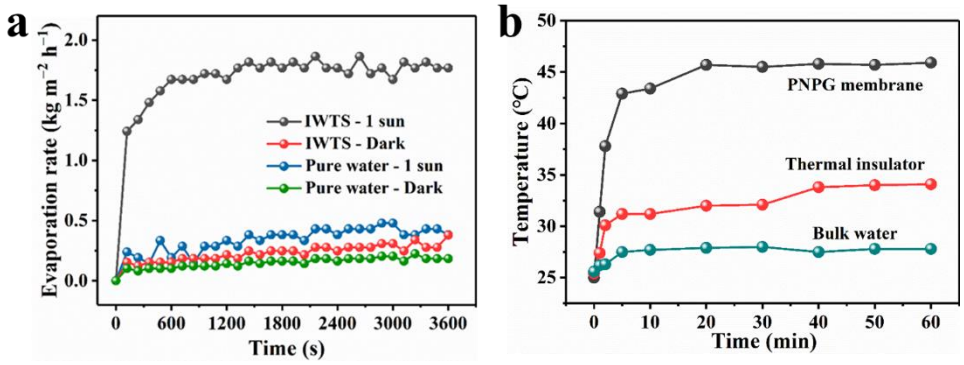

Fig. 3-9 (a) Water evaporation rate curves of IWTS system and pure water with and without solar irradiation. (b) The temperature change curves of the different positions of the IWTS system with time increase.

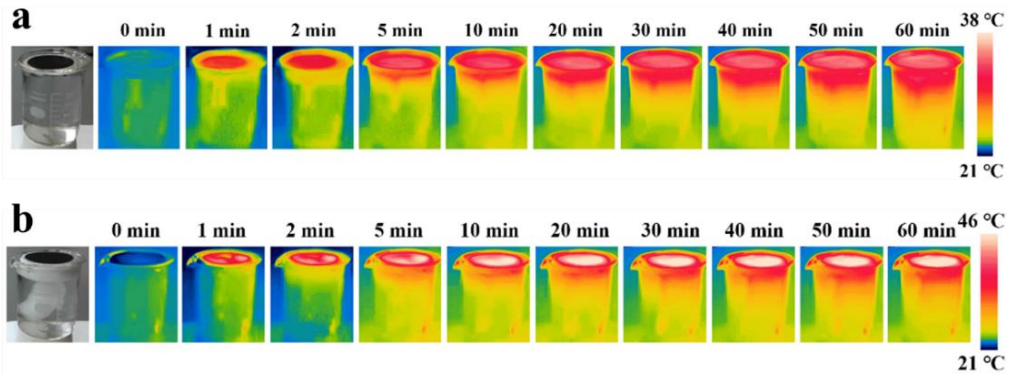

Fig. 3-10 (a) The temperature IR mapping images of the PNPGM solar evaporation system at different time points. (b) The temperature IR mapping images of the ITS solar evaporation system at different time points.

Following, the performance of the IWTS device was evaluated. The temperature change of the solar evaporation was collected by an IR camera and the water evaporation rates were calculated by monitoring the real-time mass change with simulated solar irradiation under 1 sun. Fig. S5 is the IR images of the solar steam generators with a different mass of PNPG that were marked as PNPG-0 mg, PNPG-2.5 mg, PNPG-5 mg, and PNPG-10 mg, respectively. The surface temperature of the devices rises sharply and reaches a steady-state at 26.6 ℃ (PNPG-0mg), 42.3 ℃ (PNPG-2.5mg), and 44.0 ℃ (PNPG-5mg), 45.4 ℃ (PNPG-10mg). By calculating the water evaporation rates of PNPG-0 mg, PNPG-2.5 mg, PNPG-5 mg, and PNPG-10 mg are 0.44, 1.37, 1.53, and 1.72 kg m^{-2} h^{-1}, respectively, and maintaining a steady evaporation rate under 1 sun illumination (Fig. 3-8). Since PNPG-10 mg has better evaporation efficiency, the system with this coating mass will be uniformly marked as IWTS later.

Table 1. Comparison of performance of conductive polymer-based materials.

Black polymer materials	**Q (sun)**	**v_e (kg m^{-2} h^{-1})**	**η**	**Reference**
PANI/PVDF	1	1.41	85.0 %	Ref. [44]
Janus VOPM	1	1.5~1.6	90.2 %	Ref. [43]
PPy-NL foam	1	1.76	98 %	Ref. [45]
TiO_2/PPyNP	2	2.9	97.3 %	Ref. [46]
Ni_2CO_3@PDA spong	1	2.42	109 %	Ref. [47]
PEDTO(EL-P-3040)@MF	1	1.41	88.6 %	Ref. [48]
M-PPy	1	1.447	84.72 %	Ref. [49]
PDA@MXene	1	1.276	85.2 %	Ref. [50]
PDA spong	1	1.18	74.3 %	Ref. [51]
PDA/PEI/PPy@PI	1	1.43	86.9 %	Ref. [52]
Ag/PPy membrane	1	1.55	92.6 %	Ref. [53]
PPy nanosheet	1	1.38	92.12 %	Ref. [29]
PDA@sand 2D	1	1.21	81 %	Ref. [54]
PDA@sand 3D		1.43	94 %	
PPy oriami	1	2.12	91.5 %	Ref. [55]
PDA@cotton	1	1.54	88.8 %	Ref. [22]
PDA@wood	1	1.38	87 %	Ref. [56]
This work	**1**	**1.72**	**93.5 %**	

To more clearly compare the evaporation performance of the IWTS device, the

mass loss of the IWTS device and pure water with time under dark conditions and one solar light intensity was compared (Fig. 3-5d). The evaporation rate of the IWTS device under light conditions is much faster than pure water under light or dark conditions, the mass loss ratios are 4.9 times and 11.3 times, respectively. Correspondingly, using the following equation the water evaporation rate:

$$Ve = \frac{\mathrm{d}m}{S \times \mathrm{d}t} \tag{2}$$

where m loss is the mass change, S is the area of the IWTS evaporator, and t is indicated as the irradiation time.[57] The real-time evaporation rate curves of the IWTS system and pure water with and without solar irradiation are shown in Fig. 3-9a. The evaporation performance can also be seen from the rate at which it stabilizes. Due to its excellent broadband absorption performance, it is worth noting that the solar energy efficiency of the IWTS device is as high as 93.5%. The IWTS device with outstanding evaporation performance is comparable to or even better than many recently reported black polymer-based solar steam generation systems (Table 1).

Because thermal management is one of the crucial factors that affect the efficiency of water evaporation, a good structural design can greatly improve the evaporation efficiency. Here, an IR camera was used to obtain the surface temperature changes and mapping images of the IWTS system during the simulated solar irradiation (Fig. 3-5e). After 1 h irradiation under 1 sun, the temperatures of the top view, thermal insulator, and bulk water were measured at 45.5 °C, 27.0 °C, and 22.8 °C, respectively. At the same time, the measured temperature of the top view reached 42.9 °C with 5 min solar irradiation, showing the quick response time of the IWTS system. Slight temperature

variations were observed for the bulk water (< 0.5 °C) and thermal insulator (~1.7 °C) within 5 min. By contrast, the surface temperature of the top view increased by 21.9 °C within the same condition. All these results demonstrated the fact that the PNPGM solar absorber plays a vital role in the solar-thermal conversion and the thermal insulator has exhibited an excellent thermal barrier effect and reduced the transfer of heat to the water. To make a better comparison, the generator without a water-trapped layer and the one with a PNPGM solar absorber only are named the PNPGM system (Fig. 3-10a) and thermal insulation system (TIS) (Fig. 3-10b) separately. In the thermal insulator structure system, the temperature of the top view rises to 45.6 °C after 60 mins of irradiation (Fig. 3-10a), and the heat insulation layer can reduce part of the energy loss, but some energy still diffuses into the bulk water. In contrast, the water-trapped layer IWTS in the system can also reduce heat loss to a certain extent. In the PNPGM system without a thermal insulator and water-trapped layer, the temperature of the top view rose to 36.0 °C after 60 mins of irradiation (Fig. 3-10b), and most of the energy could not be fully utilized.

3.3.3 Evaporation performance influenced by the device structure

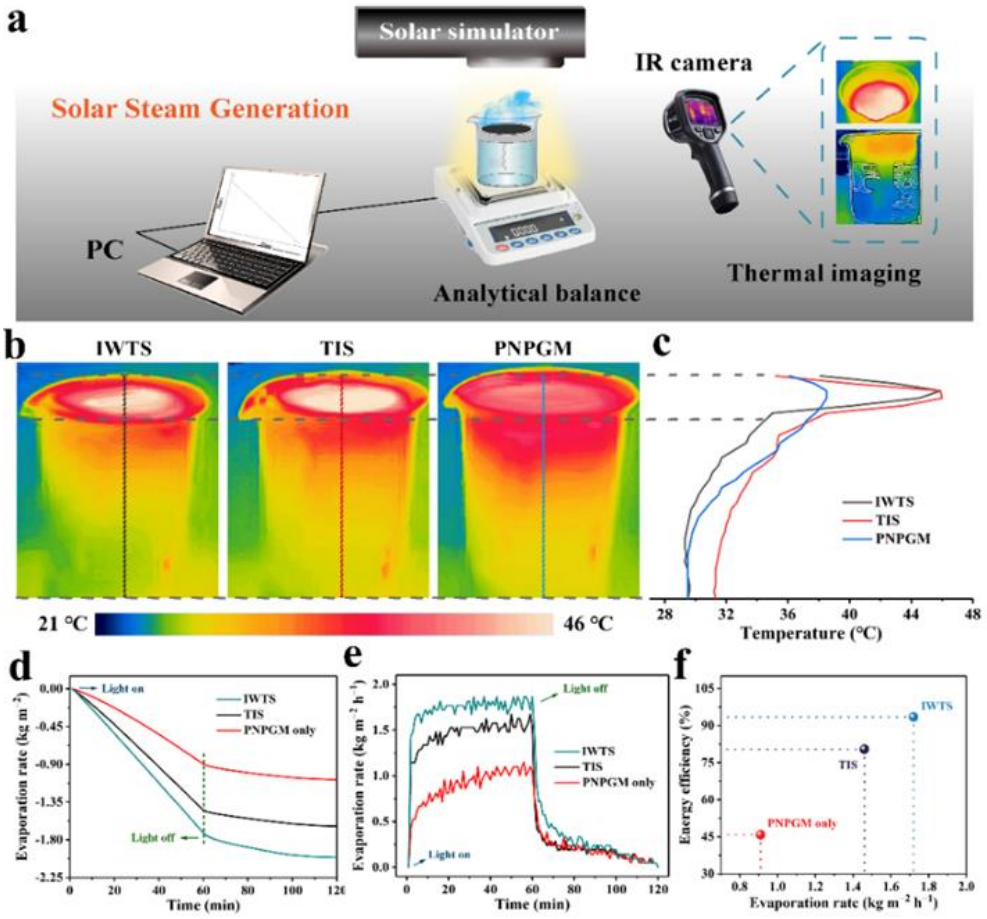

Fig. 3-11 (a) Schematic diagram of the solar evaporation measurement system. (b) Temperature distribution of PNPGM, TIS, IWTS system with 1 h irradiation under 1 sun and (c) the corresponding temperature change along the colorful dotted line. (d) Curves of water mass change (e) and the real-time evaporation rate of PNPGM, TIS, and IWTS systems, respectively. (f) Comparison of evaporation rate and energy efficiency between PNPGM, TIS, and IWTS system.

To intuitively evaluate the device structure's influence on temperature management and evaporation performance evaluation, interfacial solar steam

generation is proceeded under solar illumination to verify the temperature distribution mapping and plots. The device used in the experiment is shown in Fig. 3-11a. To compare the solar-thermal performance and energy loss of the three devices (IWTS system, TIS system, and PNPGM system), the IR mapping and plots after 1 h of solar illumination were dissected. The top of IWTS showed a temperature of about 45.9 °C (Fig. 3-11b and c), and the upper surface of the TIS device exhibited a similar high temperature, but the surface of the PNPGM showed a temperature of only 38.5 °C. The temperature mapping in the thickness direction measured from the side view is shown in Fig. 3-11b and c. The results show that, compared with the pure PNPGM and TIS devices, the heating effect of the IWTS device is highly limited to the IWTS device, and there is barely diffusion into the water, although it can be seen that the TIS device can reduce the energy loss to some extent. As a result, highly local heating greatly reduces heat loss and facilitates efficient steam generation.

The efficiency of energy utilization greatly affects the generation of steam. The solar evaporation performance of the PNPGM system, TIS system, and IWTS system was evaluated. In dark and under solar irradiation, the water evaporation rate of the PNPGM system was calculated as 0.18 and 0.91 kg m^{-2} h^{-1} (Fig. 3-11f and g), which are similar to the results previously reported.[43] The higher evaporation rate under illumination is due to the robust broadband absorption of PNPG. The similarity is that the evaporation rate of the TIS system (0.18 kg m^{-2} h^{-1}) in the dark did not show significant changes due to the interface area between water and air, and no light can be absorbed in dark. In contrast, the evaporation rate of the water increases to 1.46 kg m^{-2}

h^{-1} under 1 sun illumination due to the presence of the thermal insulation structure, which can effectively reduce the heat transfer to the bulk water and reduce the heat loss compared to the simple PNPGM system. For the IWTS system, because of the presence of the water-trapped layer, the continuous water supply of bulk water to the photothermal membrane is enhanced, and its basic water evaporation rate in dark is increased to 0.23 kg m^{-2} h^{-1}. When the IWTS system is exposed to simulated solar light, the evaporation rate increases to 1.72 kg m^{-2} h^{-1}, which is nearly 2 times higher than that of the PNPGM system. The existence of the water-trapped structure not only enhances the continuous water supply of the bulk water to the photothermal membrane but also reduces the heat transfer to the bulk water to a certain extent and reduces the heat loss. Therefore, compared with PNPGM only (45.8%) and the TIS device (80.4%), the IWTS device obtains a higher evaporation rate and energy efficiency (93.5%), which is very exciting (Fig. 3-11h).

3.3.4 The practical applications of the IWTS system

The cycle experiments were performed to further explore the reusability and lasting steam generation stability of the IWTS device. The results confirmed that such a strong device can be reused for 45 h under 1 sun illumination, as shown in Fig. 3-12a, without the water steam generation efficiency decreasing. It shows that the device had excellent photo-aging stability.

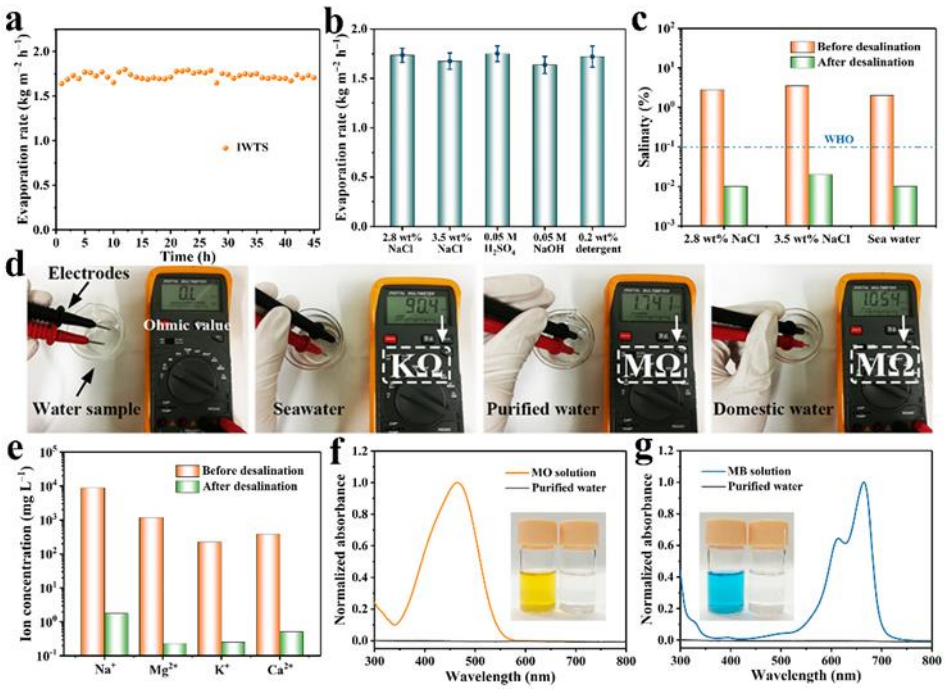

Fig. 3-12 (a) Reusability of the IWTS device in solar evaporation with 45 h irradiation. (b) The average evaporation rates in acid, alkali, salt, and detergent water conditions under 1 sun for 60 mins. (c) The salinities of homemade brine, natural seawater, and purified water from solar desalination. (d) From left to right are the device evaluating the purity of water samples with a multimeter, the ohmic value of natural seawater, purified water by solar desalination, and domestic water, respectively. (e) Concentrations of Na^{+}, Mg^{2+}, $K^{+,}$ and Ca^{2+} in the natural seawater and purified water. UV-vis spectra of the methyl orange (MO) solution (f), and methylene blue (MB) solution (g) before and after purification.

The solar evaporation performances of the IWTS device were further tested with harsh aqueous solution conditions, including homemade brine and simulated wastewater (strong acid, strong alkali, and detergent solution). Under different water conditions, the average water evaporation rate of the IWTS device is stable at around

1.70 kg m^{-2} h^{-1} (Fig. 3-12b). The solar evaporation rate was independent of salinity and the nature of the solution. After acid, alkaline, brine, and detergent solution evaporation measurement, the PNPG solar absorber of the IWTS device displayed stable evaporation performance and was intact. During the testing process, there is no salt precipitating deposit on the device surface. And it can be also used in corrosive and other extreme conditions.

For evaluating the solar desalination capacity of the IWTS device, the experiment was carried out on a homemade system. the experiment was carried out on a homemade system. In this experiment, three brine samples were used: 2.8 wt% NaCl water solution, 3.5 wt% NaCl water solution, and natural seawater (from the Sea of Japan). Studies have shown that the salinities of the purified water collected from solar desalination were significantly decreased, reaching the World Health Organization (WHO) drinking water standard (Fig. 3-12c).[58] The water purity can be intuitively evaluated by the ohmic value obtained by the digital multimeter at a constant distance between the electrodes through the resistance test (Fig. 3-12d). The resistance values of natural seawater, purified water by solar desalination, and domestic water (cooled boiled water) are 90.4 KΩ, 1.741 MΩ, and 1.054 MΩ, respectively, indicating that natural seawater has been effectively purified. Furthermore, the main cation concentrations of natural seawater and purified water collected from solar evaporation were tested (Fig. 3-12e). The four main cation concentrations in seawater show relatively high concentrations of 8890.66 mg L^{-1} (Na^{+}), 1180.26 mg L^{-1} (Mg^{2+}), 225.14 mg L^{-1} (K^{+}), and 383.43 mg L^{-1} (Ca^{2+}), but in contrast the corresponding four ions concentration in the purified water

was significantly reduced to 1.76, 0.23, 0.25, and 0.51 mg L^{-1}. In addition, the wastewater treatment capacity was studied using the same solar evaporation system (Fig. 3-12f and g). The UV-vis spectra were used to qualitatively verify the absorption spectrum of purified water evaporated from methyl blue (MB) solution (10 mg L^{-1}) and methyl orange (MO) solution (10 mg L^{-1}). Because of the negligible absorption of purified water, the IWTS steam generation system has good purification capabilities. All the results demonstrate the efficiency and high potential of the IWTS system in the fields of solar evaporation and wastewater treatment.

3.4 Conclusion

In this study, a bioinspired IWTS steam generator based on PNPG was successfully prepared using a low-cost, environmentally friendly, and scalable process for solar seawater desalination and dye removal. PNPG has effective and broadband absorption in the UV-vis-NIR region, which illustrates the high solar light absorption of the prepared device. At the same time, the construction of IWTS devices for effective thermal insulation, water-trapped, and water supply makes the solar evaporation process obtain high efficiency and high evaporation rate. Thanks to the excellent solar-thermal conversion efficiency, the surface temperature of PNPGM rose to 72 °C rapidly under 1 sun irradiation. The fabricated IWTS device in water shows outstanding solar vapor production performance that evaporation rate was 1.72 kg m^{-2} h^{-1} and energy efficiency was 93.5%. And this prepared device also shows wonderful reusability and durability without nearly zero declines in surface temperature and evaporation rate

under 5 circles of evaporation. This novel bio-inspired PNPG-based device applies a highly efficient solar-thermal conversion effect to steam generation, which exhibits the feasible application in solar desalination and pollutants removal.

Reference

[1] C.J. Vorosmarty, A.Y. Hoekstra, S.E. Bunn, D. Conway, J. Gupta, WATER. Fresh water goes global, Science 349 (2015) 478-479.

[2] G. Ni, G. Li, S.V. Boriskina, H. Li, W. Yang, T. Zhang, G. Chen, Steam generation under one sun enabled by a floating structure with thermal concentration, Nat. Energy 1 (2016) 1-7.

[3] W. Shang, T. Deng, Solar steam generation: Steam by thermal concentration, Nat. Energy 1 (2016) 1-2.

[4] A.K. Menon, I. Haechler, S. Kaur, S. Lubner, R.S. Prasher, Enhanced solar evaporation using a photo-thermal umbrella for wastewater management, Nat. Sustain. 3 (2020) 144-151.

[5] P. Tao, G. Ni, C. Song, W. Shang, J. Wu, J. Zhu, G. Chen, T. Deng, Solar-driven interfacial evaporation, Nat. Energy 3 (2018) 1031-1041.

[6] C. Chen, Y. Kuang, L. Hu, Challenges and Opportunities for Solar Evaporation, Joule 3 (2019) 683-718.

[7] F. Zhao, Y. Guo, X. Zhou, W. Shi, G. Yu, Materials for solar-powered water evaporation, Nat. Rev. Mater. 5 (2020) 388-401.

[8] Y. Yang, W. Que, J. Zhao, Y. Han, M. Ju, X. Yin, Membrane assembled from anti-fouling copper-zinc-tin-selenide nanocarambolas for solar-driven interfacial water evaporation, Chem. Eng. J. 373 (2019) 955-962.

[9] X. Wu, G.Y. Chen, G. Owens, D. Chu, H. Xu, Photothermal materials: A key platform enabling highly efficient water evaporation driven by solar energy, Mater.

Today Energy 12 (2019) 277-296.

[10] M. Gao, L. Zhu, C.K. Peh, G.W. Ho, Solar absorber material and system designs for photothermal water vaporization towards clean water and energy production, Energy Environ. Sci. 12 (2019) 841-864.

[11] K. Bae, G. Kang, S.K. Cho, W. Park, K. Kim, W.J. Padilla, Flexible thin-film black gold membranes with ultrabroadband plasmonic nanofocusing for efficient solar vapour generation, Nat. Commun. 6 (2015) 10103.

[12] D. Shin, G. Kang, P. Gupta, S. Behera, H. Lee, A.M. Urbas, W. Park, K. Kim, Thermoplasmonic and Photothermal Metamaterials for Solar Energy Applications, Adv. Opt. Mater. 6 (2018) 1800317-1800342.

[13] M. Gao, C.K. Peh, H.T. Phan, L. Zhu, G.W. Ho, Solar Absorber Gel: Localized Macro-Nano Heat Channeling for Efficient Plasmonic Au Nanoflowers Photothermic Vaporization and Triboelectric Generation, Adv. Energy Mater. 8 (2018) 1800711.

[14] X. Li, B. Zhu, J. Zhu, Graphene oxide based materials for desalination, Carbon 146 (2019) 320-328.

[15] P.D. Dongare, A. Alabastri, O. Neumann, P. Nordlander, N.J. Halas, Solar thermal desalination as a nonlinear optical process, Proc. Natl. Acad. Sci. U. S. A. 116 (2019) 13182-13187.

[16] K. 104875Li, M. Gao, Z. Li, H. Yang, L. Jing, X. Tian, Y. Li, S. Li, H. Li, Q. Wang, J.S. Ho, G.W. Ho, P.-Y. Chen, Multi-interface engineering of solar evaporation devices via scalable, synchronous thermal shrinkage and foaming, Nano Energy 74 (2020) 104875.

[17] H. Liu, C. Chen, H. Wen, R. Guo, N.A. Williams, B. Wang, F. Chen, L. Hu, Narrow bandgap semiconductor decorated wood membrane for high-efficiency solar-assisted water purification, J. Mater. Chem. A 6 (2018) 18839-18846.

[18] C. Xing, D. Huang, S. Chen, Q. Huang, C. Zhou, Z. Peng, J. Li, X. Zhu, Y. Liu, Z. Liu, H. Chen, J. Zhao, J. Li, L. Liu, F. Cheng, D. Fan, H. Zhang, Engineering Lateral Heterojunction of Selenium-Coated Tellurium Nanomaterials toward Highly Efficient Solar Desalination, Adv. Sci. 6 (2019) 1900531.

[19] Z. Li, C. Wang, Novel advances in metal-based solar absorber for photothermal vapor generation, Chin. Chem. Lett. (2019).

[20] N. Xu, H. Liu, J. Zhu, X. Yu, L. Zhou, J. Li, Plasmonic nanostructures for advanced interfacial solarvapor generation, Sci. Sin. 49 (2019) 124203.

[21] X. Zhou, Y. Guo, F. Zhao, G. Yu, Hydrogels as an Emerging Material Platform for Solar Water Purification, Acc. Chem. Res. 52 (2019) 3244-3253.

[22] X. Wu, L. Wu, J. Tan, G.Y. Chen, G. Owens, H. Xu, Evaporation above a bulk water surface using an oil lamp inspired highly efficient solar-steam generation strategy, J. Mater. Chem. A 6 (2018) 12267-12274.

[23] S. Cao, Q. Jiang, X. Wu, D. Ghim, H. Gholami Derami, P.-I. Chou, Y.-S. Jun, S. Singamaneni, Advances in solar evaporator materials for freshwater generation, J. Mater. Chem. A 7 (2019) 24092-24123.

[24] X. Zhou, F. Zhao, Y. Guo, B. Rosenberger, G. Yu, Architecting highly hydratable polymer networks to tune the water state for solar water purification, Sci. Adv. 5 (2019) 5484.

[25] B.P. Jiang, L. Zhang, X.L. Guo, X.C. Shen, Y. Wang, Y. Zhu, H. Liang, Poly(n-phenylglycine)-based nanoparticles as highly effective and targeted near-infrared photothermal therapy/photodynamic therapeutic agents for malignant melanoma, Small 13 (2017) 1602496-1602510.

[26] H. Chen, W. Liang, Y. Zhu, Z. Guo, J. Jian, B.P. Jiang, H. Liang, X.C. Shen, Supercharged fluorescent protein functionalized water-soluble poly(N-phenylglycine) nanoparticles for highly effective imaging-guided photothermal therapy, Chem. Commun. 54 (2018) 10292-10295.

[27] C. Ruan, C. Liu, H. Hu, X.L. Guo, B.P. Jiang, H. Liang, X.C. Shen, NIR-II light-modulated thermosensitive hydrogel for light-triggered cisplatin release and repeatable chemo-photothermal therapy, Chem. Sci. 10 (2019) 4699-4706.

[28] B.-P. Jiang, L. Zhang, Y. Zhu, X.-C. Shen, S.-C. Ji, X.-Y. Tan, L. Cheng, H. Liang, Water-soluble hyaluronic acid–hybridized polyaniline nanoparticles for effectively targeted photothermal therapy, J. Mater. Chem. B 3 (2015) 3767-3776.

[29] X. Wang, Q. Liu, S. Wu, B. Xu, H. Xu, Multilayer Polypyrrole Nanosheets with Self-Organized Surface Structures for Flexible and Efficient Solar-Thermal Energy Conversion, Adv. Mater. 31 (2019) 1807716-1807725.

[30] Z. Wang, Y. Zou, Y. Li, Y. Cheng, Metal-Containing Polydopamine Nanomaterials: Catalysis, Energy, and Theranostics, Small 16 (2020) 1907042.

[31] B.P. Jiang, L. Zhang, X.L. Guo, X.C. Shen, Y. Wang, Y. Zhu, H. Liang, Poly(N-phenylglycine)-Based Nanoparticles as Highly Effective and Targeted Near-Infrared Photothermal Therapy/Photodynamic Therapeutic Agents for Malignant Melanoma,

Small 13 (2017) 1602496.

[32] X. Li, R. Lin, G. Ni, N. Xu, X. Hu, B. Zhu, G. Lv, J. Li, S. Zhu, J. Zhu, Three-dimensional artificial transpiration for efficient solar waste-water treatment, Natl. Sci. Rev. 5 (2018) 70-77.

[33] Y. Shi, R. Li, Y. Jin, S. Zhuo, L. Shi, J. Chang, S. Hong, K.-C. Ng, P. Wang, A 3D Photothermal Structure toward Improved Energy Efficiency in Solar Steam Generation, Joule 2 (2018) 1171-1186.

[34] L. Zhu, M. Gao, C.K.N. Peh, G.W. Ho, Recent progress in solar-driven interfacial water evaporation: Advanced designs and applications, Nano Energy 57 (2019) 507-518.

[35] N. Xu, J. Li, Y. Wang, C. Fang, X. Li, Y. Wang, L. Zhou, B. Zhu, Z. Wu, S. Zhu, J. Zhu, A water lily-inspired hierarchical design for stable and efficient solar evaporation of high-salinity brine, Sci. Adv. 5 (2019) 7013-7021.

[36] N. Cao, S. Lu, R. Yao, C. Liu, Q. Xiong, W. Qin, X. Wu, A self-regenerating air-laid paper wrapped ASA 3D cone-shaped Janus evaporator for efficient and stable solar desalination, Chem. Eng. J. 397 (2020) 125522.

[37] P. Wang, Emerging investigator series: the rise of nano-enabled photothermal materials for water evaporation and clean water production by sunlight, Environ. Sci. Nano 5 (2018) 1078-1089.

[38] V.-D. Dao, N.H. Vu, S. Yun, Recent advances and challenges for solar-driven water evaporation system toward applications, Nano Energy 68 (2020) 104324.

[39] W. Chao, Y. Li, X. Sun, G. Cao, C. Wang, S.-H. Ho, Enhanced wood-derived

photothermal evaporation system by in-situ incorporated lignin carbon quantum dots, Chem. Eng. J. 405 (2021) 126703-126715.

[40] S. Cheng, Z. Yu, Z. Lin, L. Li, Y. Li, Z. Mao, A lotus leaf like vertical hierarchical solar vapor generator for stable and efficient evaporation of high-salinity brine, Chem. Eng. J. 401 (2020) 126108.

[41] H.-Y. Zhao, J. Zhou, Z.-L. Yu, L.-F. Chen, H.-J. Zhan, H.-W. Zhu, J. Huang, L.-A. Shi, S.-H. Yu, Lotus-Inspired Evaporator with Janus Wettability and Bimodal Pores for Solar Steam Generation, Cell Rep. Phy. Sci. 1 (2020) 100074.

[42] L. Wu, Z. Dong, Z. Cai, T. Ganapathy, N.X. Fang, C. Li, C. Yu, Y. Zhang, Y. Song, Highly efficient three-dimensional solar evaporator for high salinity desalination by localized crystallization, Nat. Commun. 11 (2020) 521.

[43] H.-H. Yu, L.-J. Yan, Y.-C. Shen, S.-Y. Chen, H.-N. Li, J. Yang, Z.-K. Xu, Janus Poly(Vinylidene Fluoride) Membranes with Penetrative Pores for Photothermal Desalination, Research 2020 (2020) 1-10.

[44] Y. Zou, X. Chen, W. Guo, X. Liu, Y. Li, Flexible and Robust Polyaniline Composites for Highly Efficient and Durable Solar Desalination, ACS Appl. Energy Mater. 3 (2020) 2634-2642.

[45] Y. Xu, J. Wang, F. Yu, Z. Guo, H. Cheng, J. Yin, L. Yan, X. Wang, Flexible and Efficient Solar Thermal Generators Based on Polypyrrole Coated Natural Latex Foam for Multimedia Purification, ACS Sustainable Chem. Eng. 8 (2020) 12053-12062.

[46] J. Xing, J. Tong, Y. Liu, Y. Guo, L. Zhuge, D. Zhang, R. Duan, B. Song, Y. Zhao, B. Dong, A high-efficiency ammonia-responsive solar evaporator, Nanoscale 12 (2020)

9680-9687.

[47] B. Shao, Y. Wang, X. Wu, Y. Lu, X. Yang, G.Y. Chen, G. Owens, H. Xu, Stackable nickel–cobalt@polydopamine nanosheet based photothermal sponges for highly efficient solar steam generation, J. Mater. Chem. A 8 (2020) 11665-11673.

[48] C. Liu, C. Cai, X. Zhao, Overcoming Salt Crystallization During Solar Desalination Based on Diatomite-Regulated Water Supply, ACS Sustainable Chem. Eng. 8 (2020) 1548-1554.

[49] Y. Fan, W. Bai, P. Mu, Y. Su, Z. Zhu, H. Sun, W. Liang, A. Li, Conductively monolithic polypyrrole 3-D porous architecture with micron-sized channels as superior salt-resistant solar steam generators, Sol. Energy Mater. Sol. Cells 206 (2020) 110347.

[50] X. Zhao, X.-J. Zha, L.-S. Tang, J.-H. Pu, K. Ke, R.-Y. Bao, Z.-y. Liu, M.-B. Yang, W. Yang, Self-assembled core-shell polydopamine@MXene with synergistic solar absorption capability for highly efficient solar-to-vapor generation, Nano Res. 13 (2019) 255-264.

[51] Y. Zhang, X. Yin, B. Yu, X. Wang, Q. Guo, J. Yang, Recyclable Polydopamine-Functionalized Sponge for High-Efficiency Clean Water Generation with Dual-Purpose Solar Evaporation and Contaminant Adsorption, ACS Appl. Mater. Interfaces 11 (2019) 32559-32568.

[52] Y. Xu, H. Xu, Z. Zhu, H. Hou, J. Zuo, F. Cui, D. Liu, W. Wang, A mechanically durable, sustained corrosion-resistant photothermal nanofiber membrane for highly efficient solar distillation, J. Mater. Chem. A 7 (2019) 22296-22306.

[53] Y. Xu, J. Ma, Y. Han, H. Xu, Y. Wang, D. Qi, W. Wang, A simple and universal

strategy to deposit Ag/polypyrrole on various substrates for enhanced interfacial solar evaporation and antibacterial activity, Chem. Eng. J. 384 (2020) 123379-123387.

[54] F. Ni, P. Xiao, N. Qiu, C. Zhang, Y. Liang, J. Gu, J. Xia, Z. Zeng, L. Wang, Q. Xue, T. Chen, Collective behaviors mediated multifunctional black sand aggregate towards environmentally adaptive solar-to-thermal purified water harvesting, Nano Energy 68 (2020) 104311-104321.

[55] W. Li, Z. Li, K. Bertelsmann, D.E. Fan, Portable Low-Pressure Solar Steaming-Collection Unisystem with Polypyrrole Origamis, Adv. Mater. 31 (2019) 1900720.

[56] X. Wu, G.Y. Chen, W. Zhang, X. Liu, H. Xu, A Plant-Transpiration-Process-Inspired Strategy for Highly Efficient Solar Evaporation, Adv. Sustain. Syst. 1 (2017) 1700046-1700053.

[57] Y. Wang, C. Wang, X. Song, M. Huang, S.K. Megarajan, S.F. Shaukat, H. Jiang, Improved light-harvesting and thermal management for efficient solar-driven water evaporation using 3D photothermal cones, J. Mater. Chem. A 6 (2018) 9874-9881.

[58] F. Zhao, X. Zhou, Y. Shi, X. Qian, M. Alexander, X. Zhao, S. Mendez, R. Yang, L. Qu, G. Yu, Highly efficient solar vapour generation via hierarchically nanostructured gels, Nat. Nanotechnol. 13 (2018) 489-495.

Chapter 4 Nature-inspired poly(N-phenylglycine)/wood solar evaporation system for high-efficiency desalination and water purification

4.1 Introduction

Human beings are currently facing many unprecedented challenges, including energy, fresh water, sanitation, *et al.*[1, 2] Among them, how to obtain safe and sanitary drinking water employing lower energy consumption, and better meet the sustainable development goals (SDGs), has become a hot topic in current research.[3, 4] To solve the above problems, interfacial solar evaporation is one of the most attractive, convenient, and primitive ways to realize the application of solar thermal technology, precisely because renewable solar energy and seawater are the most widely distributed resources on the earth.[5-7] It is well known that water evaporation is an interface process, and the local heat at the air-water interface has been considered to be the key to accelerating solar evaporation.[8-10] It is precisely because the local energy utilization determines the overall performance of the evaporator, and in the pursuit of performance advantages often ignores the initial intention of the simple design of the evaporator.[9,11-13] Therefore, it is markedly important to develop a simple, convenient and efficient solar evaporator construction strategy, which integrates a series of collaborative local interface heating processes such as solar absorption/conversion, heat management, and water transportation, and it's more attractive than a complicated

design.[8, 14-16]

Inspired and gifted by nature, people get a lot of inspiration and production materials, and trees are even more important in our daily life. Trees are one of the most common and abundant biological factories in human life, with a perfect system of transpiration and photosynthesis. During natural growth, trees can obtain water and nutrients from the earth through xylem blood vessels by the transpiration cohesion-tension (C-T) mechanism, and further transport through radial branches to the leaves for photosynthesis.[17, 18] This inspired us to whether we can directly use tree-derived wood to design solar evaporators. As a traditional material that comes from natural plants, wood not only has natural water transportation channel and excellent heat insulation effect,[19, 20] but also has the natural advantages of light material, environmental protection, and renewable and sustainable utilization.[21, 22] More importantly, the natural water transport channel in the wood maintains the original water capillary absorption and transport capacity of plants. Thus, because of interfacial solar evaporation similar to the water conversion process of plants, that is, water is transported continuously by capillarity and effectively converted to steam in the photothermal layer,[23, 24] wood has become an ideal carrier material for interfacial solar evaporation.

In addition to a wood substrate, another factor determining solar evaporation performance is the solar absorption surface, since the poor light absorption capacity of natural wood is not sufficient for stable and efficient interfacial solar evaporation.[20] In the design of a wood-based solar evaporator, it is necessary to build a photothermal

absorption layer on the surface of the wood.[25, 26] It is commonly used photothermal material modification or performing special treatment on the surface of the wood to obtain high-efficiency light absorption and energy conversion. For example, Zhu *et al*. designed a 3D wood-based evaporator decorated with plasmonic metal nanoparticles (Ag, Au, and Pd) for solar evaporation, getting an energy conversion efficiency as high as 85% under 10 sun.[27] Hu's group built a scalable narrow bandgap semiconductor modified wood-based membrane, making a fantastic material for interface solar evaporation and achieving energy efficiency of 86.2% under 5 sun.[28] Jeon *et al.* developed a solar evaporator that uses a CO_2 laser to make wood surfaces into graphite-carbon layers and create grid patterns of graphitic carbon layers on the wood, achieving the evaporation rate and energy efficiency to be 1.26 kg m^{-2} h^{-1} and 77%.[29] Even so, the relative difficulty of achieving cost-effective and energy-efficient manufacturing of these materials or processing technologies has prevented large-scale practical applications. In recent years, due to the advantages of photothermal polymers, such as simple synthesis process, high solar-heat conversion efficiency, lightweight, and low cost, they are attractive in building high-performance interface solar evaporators.[30-33] Currently, polyaniline (PANI),[34, 35] polydopamine (PDA)[36, 37], and polypyrrole (PPy),[38, 39], *etc.*, have been widely reported. PNPG is a kind of dark-colored polymer and biosafety photothermal polymer material.[40-42] Similar to the above-conjugated polymers, the photothermal conversion mechanism of PNPG is considered to be that it has a large conjugated π-electron system, which promotes the excitation of electrons under light irradiation and is accompanied by various π–π*

transitions. Excited electrons relax through electron-phonon coupling, so the absorbed light energy is transferred from the excited electrons to the vibrational mode of the entire atomic lattice, resulting in a macroscopic increase in material temperature.[43] It is intuitively shown that it has high absorption in the UV-vis-NIR region And like most conjugated polymers, PNPG is stable under light irradiation. In our previous study, we applied PNPG in the field of interfacial solar evaporation and obtained excellent evaporation performance.[44, 45] It has been confirmed that high light-to-heat conversion performance is obtained due to its effective absorption in the full band range. In addition, PNPG is more cost-competitive compared to precious metal nanoparticles, semiconductor materials, carbon nanomaterials, or through special processing processes. Besides, it has lower energy consumption because PNPG can be prepared under mild conditions. Hence, the combination of PNPG and wood with superior performance and high-cost performance to build solar evaporators is a worthy research topic.

In this work, inspired by the water transportation and liquid-vapor conversion process of the plants, we developed a wood-based evaporator that combines PNPG photothermal nanomaterials and a multi-porous with heat-insulating wood to achieve efficient seawater solar desalination (Fig. 4-1). The PNPG wood solar evaporation system features effective full-band light absorption, easy preparation, lightweight and inherent heat insulation, as well as the natural transporting water microchannel, making it excellent performance and competitive in seawater desalination and wastewater purification. Similar to the water transportation and conversion of plants, the PNPG

wood evaporator realizes water transportation under the driving force of capillary action and cooperates with the effective photothermal conversion of the upper surface to achieve steam generation. This PNPG wood evaporator can be acted as an outstanding solar desalination device. In addition, clean water can be gathered using the PNPG wood device, and the purified water meets the drinking water standard. All these results show that the PNPG wood solar evaporator is a hopeful material with characteristics of robust, expansible, and cost performance, which will have a broad application prospect inefficient solar desalination.

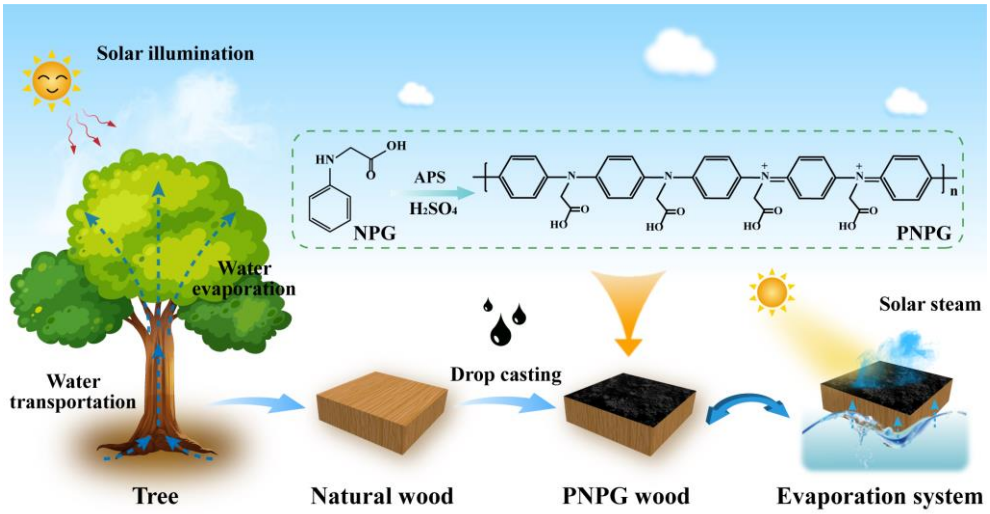

Fig. 4-1 Illustration demonstrating the fabrication of PNPG wood solar evaporator and the installation of evaporation system for interface solar evaporation.

4.2 Experimental Section

4.2.1 Reagents and materials

Wood materials were purchased from a local market and then cut into the size of 3 cm × 3 cm × 1 cm (length × width × height) with the growth direction. N-phenylglycine (NPG) was received from Tokyo Chemical Industry. Ammonium

persulfate (APS), NaCl, H_2SO_4, methylene blue (MB), and methyl orange (MO) were provided by Fujifilm Wako Pure Chemical. All of the reagents were applied directly in the following experiments.

4.2.2 Preparation of PNPG nanoparticles

The PNPG was synthesized by the following: adding 7 mmol NPG into 50 mL of 0.1 M H_2SO_4 solution under room temperature to form the NPG solution. Then added 7 mmol APS with 50 mL of 0.1 M H_2SO_4 together and then slowly added to the NPG solution. After 24 h, the black suspension was formed in ice water bath condition. The above sample was separated and purified with ultrapure water to remove the unreacted reagents and then re-dispersed for later application.

4.2.3 Preparation of PNPG wood solar absorber

To ensure PNPG suspension was evenly coated on the wood surface, the PNPG wood solar evaporator was prepared carefully on the natural wood surface by the drop-casting method. In this process, a PNPG suspension containing a solute mass of 10 mg was used. The obtained PNPG wood device was dried naturally overnight and the wood-based solar absorber was successfully prepared.

4.2.4 Characterization

The topography images of PNPG nanoparticles were collected from a transmission electron microscope (Hitachi HT-7700, TEM, Japan) and the microscopic images of natural wood and PNPG wood were taken using scanning electron microscopy (Hitachi S-4300, SEM, Japan). The solar light absorption performance was evaluated by UV-

vis-NIR spectra (UV-3600, Shimadzu, Japan). The functional groups of materials were collected via FT-IR spectra (PerkinElmer Spectrum Two N, The USA). The surface contact angles and wetting of natural wood and PNPG wood were characterized *via* the DMs-401 contact angle system (Kyowa Interface Science, Japan). The IR images were obtained by a FLIR thermal imaging camera. The ion concentrations in seawater and distilled water were tested with the help of Shimadzu ICPE-9000. The salinity of seawater and distilled water was tested by a LAQUAtwin salt meter (Horiba Scientific, Japan).

4.2.5 Experiment for solar desalination

The interfacial solar evaporation with mass and temperature changes was measured at 1 sun by the XES-40S3-TT solar simulator (SAN-EI Electric, Japan). The indoor temperature and humidity were kept at 25 °C and 60% during the experiments, respectively. The water mass changes used to calculate evaporation rates and solar-heat efficiency were recorded in real-time by an FX-200GD balance with an accuracy of 0.001 g (A&D Company, Japan).

The following equation was used to calculate the energy efficiency (η) of the interface solar evaporation process:[46-48]

$$\eta = (m_1\text{-}m_0)h_v/C_{opt}P_0 \quad (1)$$

where m_1 (units: kg m^{-2} h^{-1}) represents the interface solar evaporation rate, m_0 (units: kg m^{-2} h^{-1}) is the dark natural evaporation rate, h_v (units: kJ kg^{-1}) donates to the liquid-vapor phase transition enthalpy, C_{opt} is the optical density, and P_0 (units: W m^{-2}) donates to the power density of one sun illumination.

Corresponds with the real-time evaporation rates V_e (kg m^{-2} h^{-1}) of solar evaporation systems were determined by the below equation:

$$V_e = dm/(S \times dt) \quad (2)$$

where dm (units: kg) is the water weight change per minute, S (units: m^2) donates the area of the PNPG wood device, and t (units: h) donates the solar illumination time.

4.3 Results and discussion

4.3.1 Preparation and characterization of PNPG wood device

PNPG wood solar evaporator was realized in this work. To fabricate PNPG wood solar absorber, tetragonal wood blocks with the vessel direction were used. In brief, the PNPG was synthesized (the synthesis process of PNPG is shown in Fig. 4-2a) and then coated on the wood surface by the drop-casting method. For the overnight drying, the PNPG wood solar evaporator was obtained.

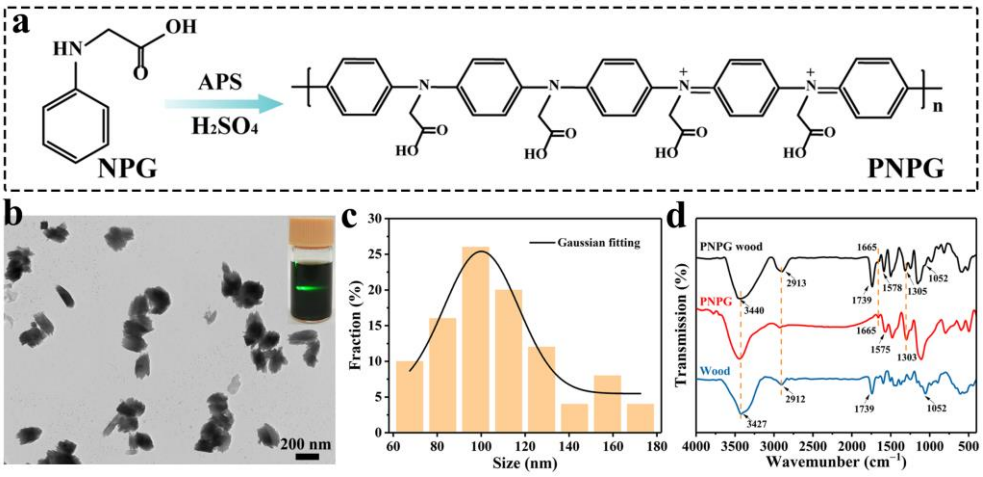

Fig. 4-2 (a) The synthesis process of PNPG. (b) TEM image of PNPG nanoparticles Inset: photo of Tyndall effect of PNPG solution. (c) The corresponding size distribution of PNPG nanoparticles. (d) FT-IR spectra of wood, PNPG, and PNPG wood.

Herein, the photothermal polymer PNPG was firstly synthesized, and then, the morphology and chemical properties of PNPG were investigated. As shown in Fig. 4-2b, the PNPG presents uniform distribution and monodisperse morphology. The PNPG solution shows an obvious Tyndall effect because of the existence of the large number of nanoscale particles, which on the other hand proved the morphological characteristics observed by TEM. The size distribution was noticed to be about 120 nm, which is to the corresponding Gaussian fitting data (Fig. 4-2c). Further, PNPG, natural wood, and PNPG wood were compared at the physical and chemical levels. The FT-IR spectra results show the chemical functional groups of natural wood, PNPG, and PNPG wood (Fig. 4-2d). The main components of the cell wall of natural wood, such as carbohydrate and lignin with an aromatic ring structure, exhibit several typical absorption peaks. The corresponding peaks located at 3427 cm^{-1}, 2912 cm^{-1}, 1739 cm^{-1}, and 1052 cm^{-1} were related to O–H, C–H, C=O, and C–O stretching, respectively.[49, 50] In contrast, the PNPG wood exhibited characteristic PNPG bands. For the main absorption peaks of the PNPG wood, the C=O stretching vibration was located at 1665 cm^{-1}, the band at 1578 cm^{-1} was attributed to the quinonoid structure, and the peaks located at 1305 cm^{-1} were related to the C-N bond.[40, 44] Notably, compared to raw wood, the O-H stretching of PNPG wood shifted from 3427 to 3440 cm^{-1}, and that's probably because of the existence of the hydrogen bonding between the nitrogen or carboxyl groups of the PNPG and the hydroxyl groups of wood. The above observations indicated that the surface of natural wood was successfully coated with PNPG nanoparticles.

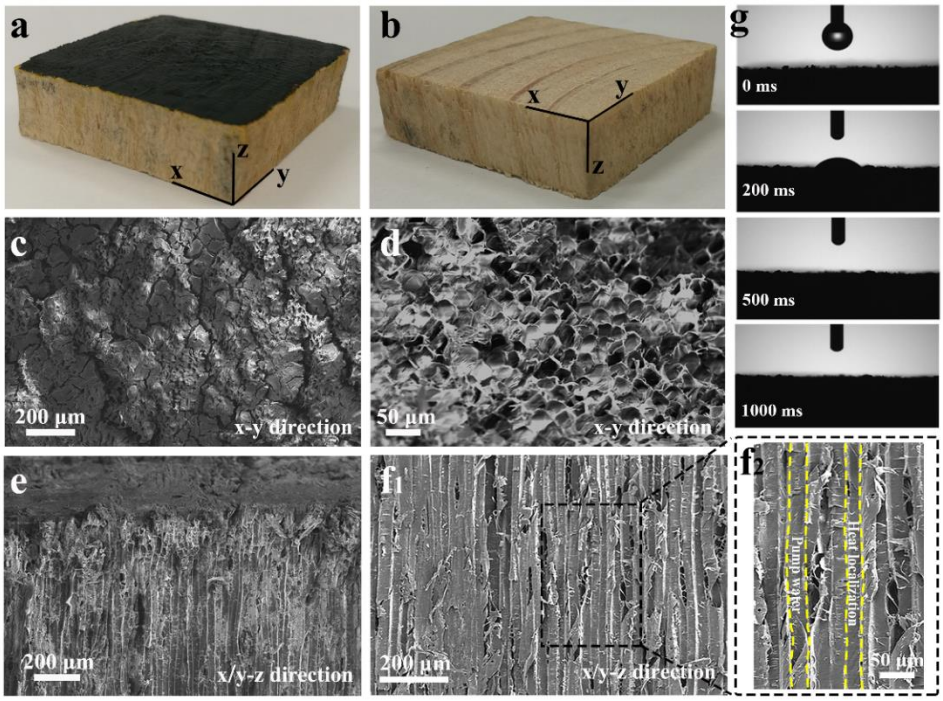

Fig. 4-3 (a, b) Digital photos of PNPG wood and natural wood, (c, d) SEM photos of the cross direction of PNPG wood, and natural wood, respectively. (e, f) SEM photos of the longitudinal direction of PNPG wood, and natural wood, respectively. (f_2) shows a magnified image in (f_1). (g) Wettability of the top surface of PNPG wood.

PNPG nanoparticles were anchored on the natural wood surface by the drop-casting method. Because of the coating of PNPG nanoparticles, a black surface can be observed in PNPG wood compared to natural wood (Fig. 4-3 a and b). Due to the PNPG with a strong light absorption effect, PNPG wood has potential application for efficient solar interface evaporation. At the micro-level, the cross-direction SEM image of the wood reveals a highly porous microstructure (Fig. 4-3d), while the SEM image of cross direction shows the long microchannel of natural xylem vessels (Fig. 4-3f). It is these natural microchannels that form a continuous network in plants to transport water and nutrients, and here these natural microchannels were ingeniously applied to keep water

flowing into the photothermal layer. By surface coating treatment, the PNPG wood device maintains the morphology of a good porous structure of natural wood, moreover, a several microns thin photothermal layer was grown (Figs. 3c and 3e). The above structural characteristics prove that the PNPG wood device has sufficient innate conditions for interface solar evaporation.

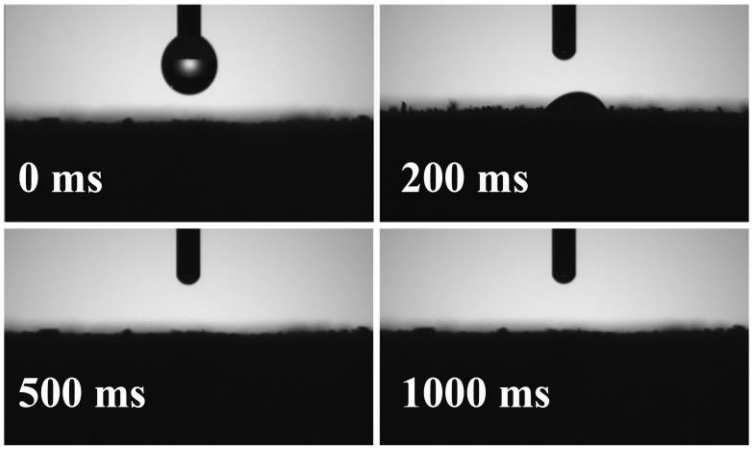

Fig. 4-4 Wettability of the top surface of natural wood.

Both the PNPG wood sample and the natural wood showed super hydrophilicity, as shown in Fig. 4-3g and Fig. 4-4. The water droplets (3 μL) dropped on the surface of PNPG wood can be quickly adsorbed within a very short time, which is consistent with the super-hydrophilic character of natural wood. The results indicate that the modified PNPG coating on the surface has a negligible influence on water transmission, and it is also confirmed that the water transport can meet the needs of subsequent solar evaporation. Due to its natural porous structure and super hydrophilicity, the prepared PNPG wood can effectively do shifting of water and be used as a water reservoir, providing better basic conditions for interfacial solar evaporation. It is also verified that the special multi-channel structure of wood can provide favorable conditions for water

transport and solar steam overflow.

4.3.2 Solar-heat conversion and evaporation performance

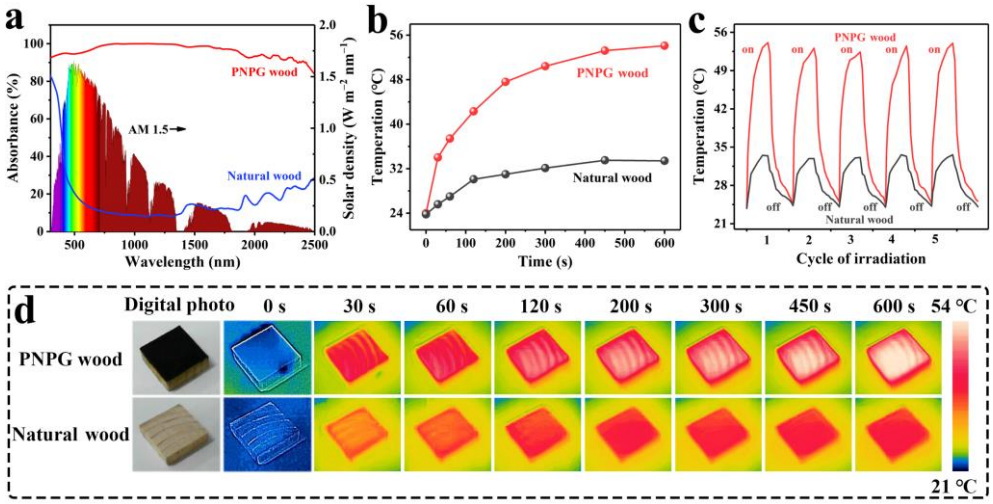

Fig. 4-5 (a) The UV−vis−NIR spectra of natural wood and PNPG wood. The rainbow color area represents the normalized AM 1.5G spectral solar density. (b) Surface temperature change curves of the natural wood and PNPG wood under 1 sun. (c) The temperature curves of the photothermal cycle test for natural wood and PNPG wood. (d) Infrared imaging of surface temperature of natural wood and PNPG wood under 1 sun.

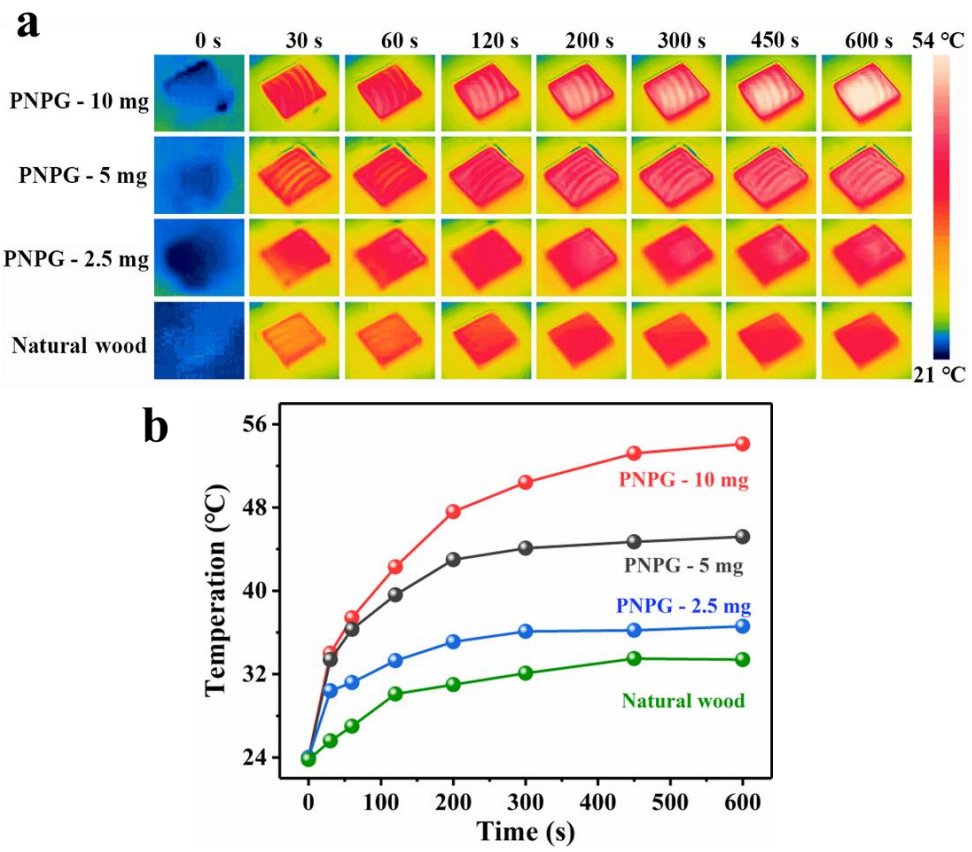

Fig. 4-6 (a) Infrared imaging of surface temperature of wood-based photothermal absorber with different PNPG coating mass under 1 sun. (b) Surface temperature change curves of wood-based photothermal absorber with different PNPG coating mass under 1 sun.

The performance of the PNPG wood solar absorber attributes to the photothermal conversion capability of PNPG nanoparticles. The full band absorption performance of PNPG wood was investigated by the UV-vis-NIR spectra. As shown in Fig. 4-5a, natural wood reflects most of the solar radiation, resulting in poor absorption of solar light. After surface modification of PNPG, the totality solar light absorption rate of PNPG wood remarkably increase, exhibiting a full band absorption range from 300 nm to 2500 nm. This improvement is owed to the effective solar-heat conversion of PNPG

coating, confirming the previously mentioned concentrating light energy. Encouraged by the high solar absorption rate of PNPG wood, the superior photothermal conversion effect of PNPG wood was verified by measuring the change of surface temperature of PNPG wood with solar irradiation. The temperature rise of the absorbers with different PNPG coating mass was monitored under 1 sun (Fig. 4-6). It is found that with the PNPG mass increase, the solar-thermal conversion effect gradually becomes better. Considering that further increasing the mass of PNPG coating can improve the total absorption rate, the too thick coating will lead to the deterioration of stability and durability. Therefore, a PNPG coating mass of 10 mg was used for subsequent studies. To be specific, the results were exposed to 1 sun solar irradiation and the temperature changes were shown in Fig. 4-5 b and d. The surface temperature of PNPG wood rises rapidly under 1 sun, and the high temperature of 54 ℃ can be reached at 600 s. By comparison, the heating effect under the same irradiation condition is very weak. Moreover, cycles of photothermal tests reflect that the highly light-stable PNPG wood and the energy conversion ability are well preserved (Fig. 4-5c). These results indicate that PNPG wood with better light stability can be used as an effective solar absorber for interfacial solar evaporation.

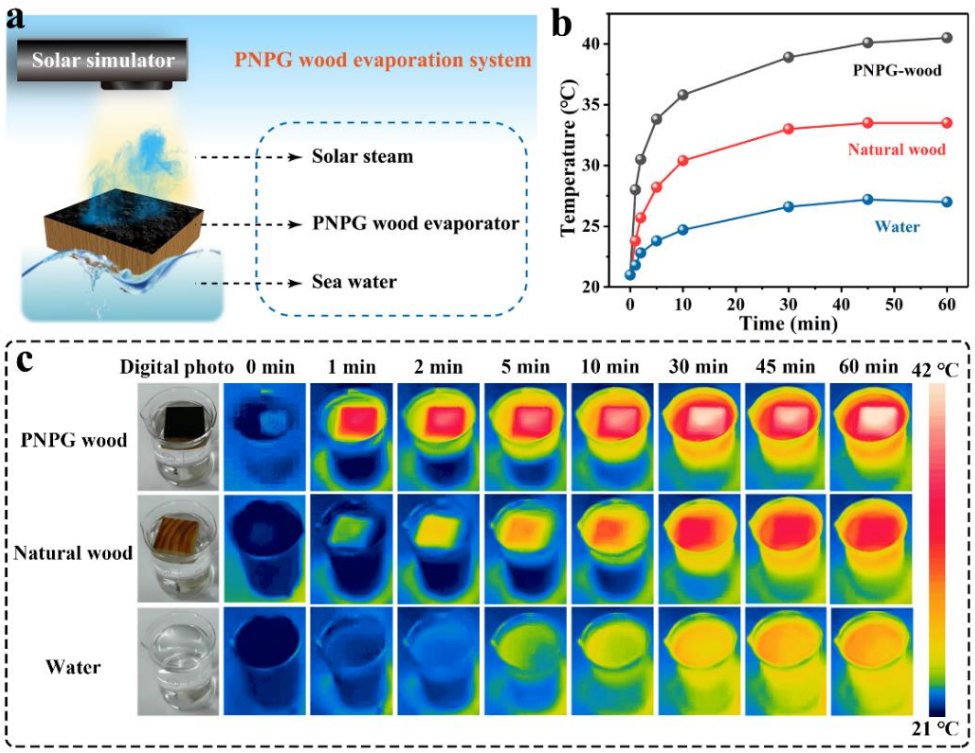

Fig. 4-7 (a) Schematic diagram of PNPG wood interface solar desalination system. (b) Temperature curves of the PNPG wood, natural wood, and pure water system at various time points and (c) the corresponding thermal images in (b)

To further investigate the solar-heat conversion property and solar evaporation performance of PNPG wood, PNPG wood in bulk water was exposed to 1 sun solar light irradiation (Fig. 4-7a). IR camera is applied to monitor the real-time temperature change in the process of solar-to-heat conversion. After 60 mins of irradiation, the temperature of the PNPG wood surface significantly increased with a large temperature difference of 21 °C compared to the beginning. By contrast, the top temperature change of the natural wood and bulk water is only 12 °C and 6 °C under the same condition irradiation, and the solar-heat conversion performance is weaker. This is because that natural wood has a low thermal conductivity, which is a natural advantage that can

effectively reduce heat loss. As a result, the wood acts as a natural insulator between the bulk water and PNPG coating, which effectively inhibits the loss of energy from the solar absorption layer to bulk water. To demonstrate the heat insulation effect of wood, the temperature distribution of PNPG wood after 1 sun irradiation for 60 min is shown in Fig. 4-7 b and c. Compared with the PNPG coating surface, the temperature of the bulk water changed insignificantly. Here, the PNPG wood absorber provides a natural microchannel for continuous solar steam overflow, and the photothermal layer of PNPG wood does not directly exchange heat with the bulk water, thus achieving good heat management.

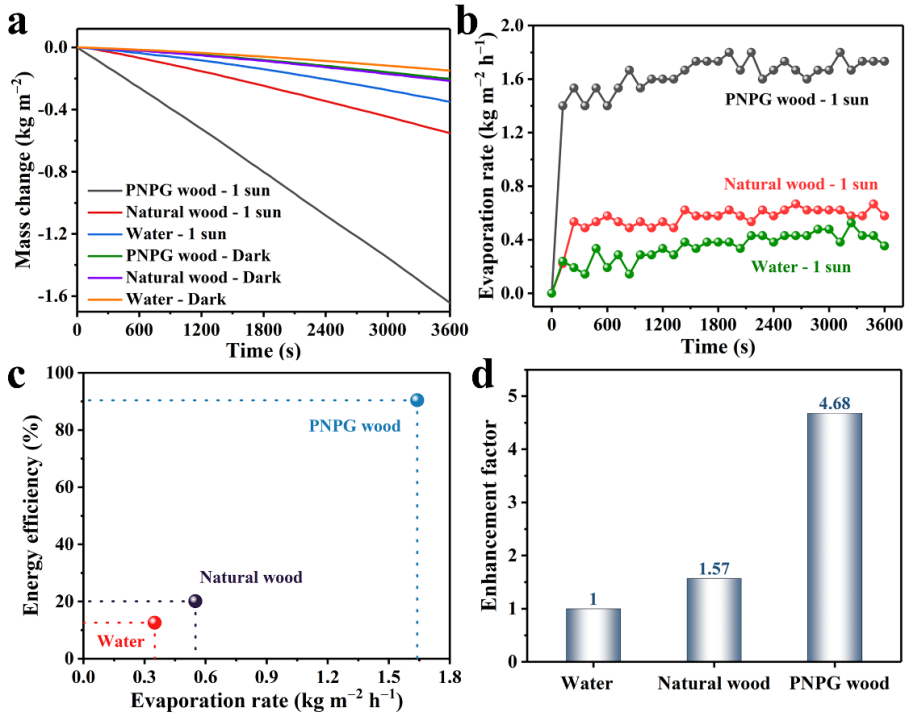

Fig. 4-8 (a) Mass change curves depending on the time of the PNPG wood, natural wood, and pure water under different conditions, (b) and the corresponding real-time water evaporation rate. (c) Evaporation rates and efficiency. (d) The evaporation enhancement effect.

Fig. 4-9 Digital photograph of the PNPG wood solar evaporation system.

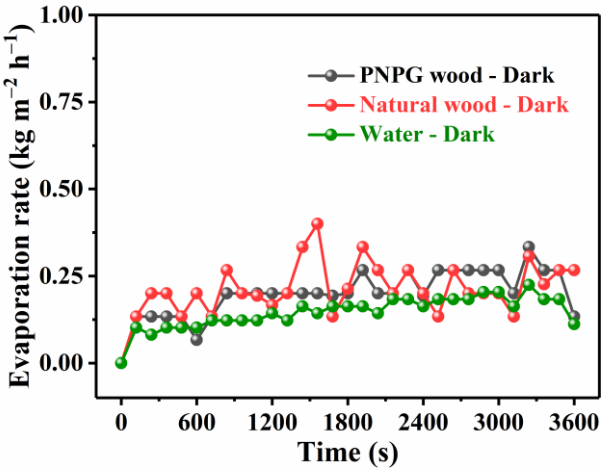

Fig. 4-10 Water evaporation rate curves of the PNPG wood, natural wood, and pure water in dark conditions.

Then, the solar evaporation performance of the PNPG wood system was evaluated, the measurements were carried out under 1 sun irradiation by a homemade device and the purified water was collected (Fig. 4-9). The over-time mass changes of PNPG wood,

natural wood, and pure water under different conditions were shown in Fig. 4-8a. In the control group of pure water and natural wood, the evaporation rates were measured to be just 0.35 and 0.55 kg m^{-2} h^{-1}, while the PNPG wood system was measured at 1.64 kg m^{-2} h^{-1}, much higher than that of pure water and natural wood. Then corresponding real-time evaporation rates are calculated, and the results are shown in Fig. 4-8b and Fig. 4-10, respectively. The high evaporation rate at which it stabilizes can also reveal the high-efficiency evaporation performance. By calculating and comparing the energy efficiency of the three evaporation systems, the evaporation performance can be compared more intuitively. As shown in Fig. 4-8c, compared with water (12.6%) and natural wood (20.1%), the PNPG wood evaporator can achieve a higher evaporation rate and energy efficiency (90.4%). The ratio of the evaporation rates of PNPG wood, natural wood, and pure water was defined as an enhancement factor to explain the difference in the performance of the three systems. The result as illustrated in Fig. 4-8d, the enhancement factor of pure water is set as 1, the natural wood is only 1.57, while the PNPG wood is increased to 4.68 under the same conditions. This result is attributed to the strong solar-heat effect of PNPG wood due to its more efficient utilization of solar light. The surface of the PNPG coating effectively absorbs solar light and generates a large amount of heat, while the natural water transport channels enable water vapor to escape rapidly from the energy-focused evaporation interface. The natural insulation of the wood traps most of the heat, thus improving the evaporation rate and efficiency of the PNPG wood. All these make the PNPG wood system achieve stable and efficient performance.

4.3.3 The practical applications of PNPG wood device

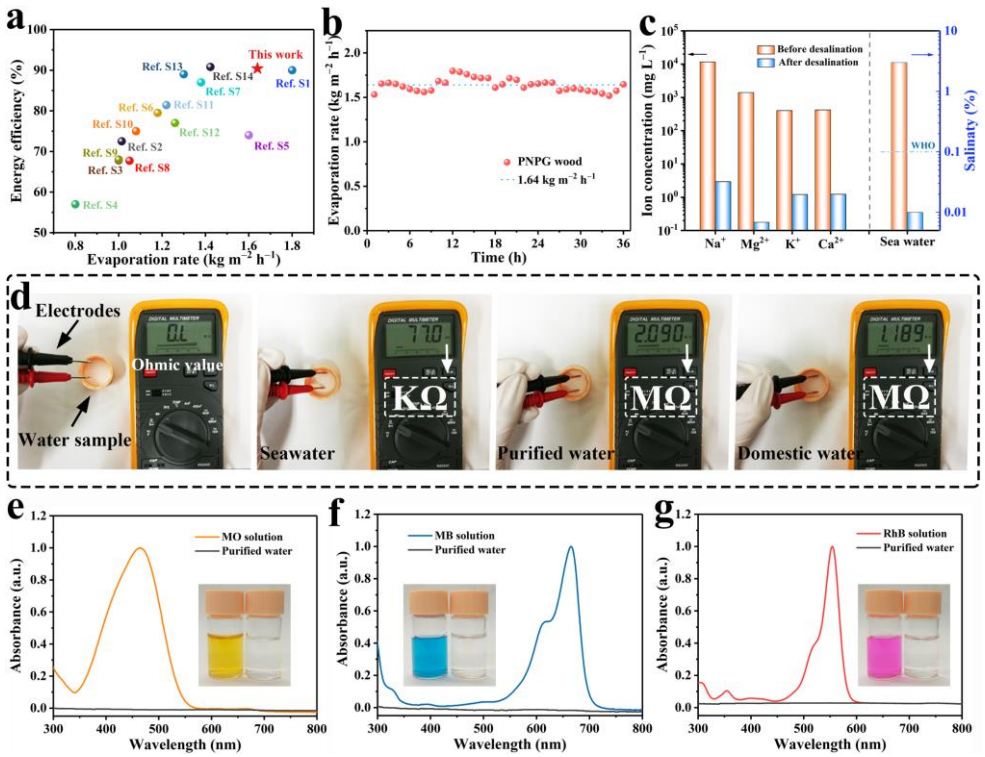

Fig. 4-11 (a) The performance of previous wood-based solar evaporation system comparison with this work. (b) Reusability of PNPG wood solar evaporator. (c) The ion concentrations and salinity in purified water and seawater. (d) Ohmic value of seawater, purified water, and domestic water, respectively. UV−vis spectra of the MO solution (e), MB solution (f), and RhB solution (g) before and after purification.

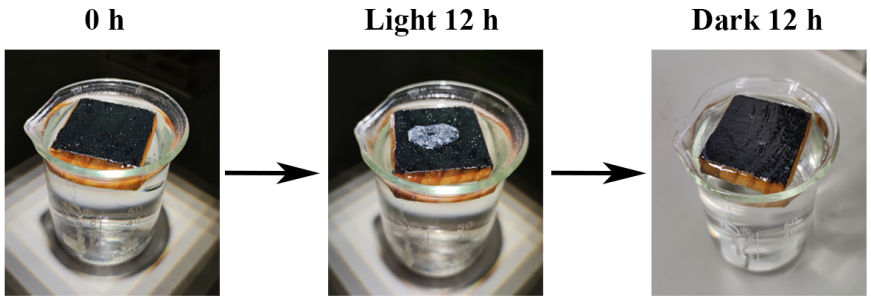

Fig. 4-12 Photos of salt crystallization on the PNPG wood evaporator surface for 12 h evaporation and 12 h dark condition under natural sea water.

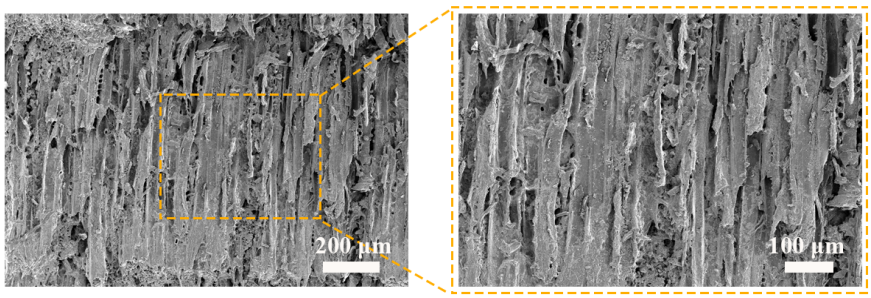

Fig. 4-13 SEM photos of the PNPG wood evaporator after long-term solar evaporation in the natural sea water.

The properties of some representative wood-based evaporators reported in recent years were summarized in Fig. 4-11a and Table 1, which were compared with PNPG wood. In contrast, the PNPG wood exhibits outstanding evaporation performance. Both the evaporation rate and evaporation efficiency are comparable or even better than the reported research. More importantly, compared with some evaporators reported so far, the PNPG Wood evaporator has some advantages in performance and cost performance (Table 2). Then, the reusability performance of PNPG wood for solar water evaporation was explored by cycle experiments under 1 sun. As shown in Fig. 4-11b, the results proved that such robust materials can be reused in the long term under 1 sun without the evaporation efficiency decreasing, confirming the remarkable stability of the PNPG wood evaporator. Since the natural seawater contains a lot of salt, after a long period of solar evaporation, salt crystallization will inevitably occur on the surface of the evaporator (Fig. 4-12**)**. However, after 12 h of dark conditions, the salt crystallization on the surface was completely dissolved. The results show that salt crystallization will not block the water transport channel, so it has little effect on the durability of the PNPG wood evaporator. At the same time, the SEM photos (Fig. 4-13**)** of the sample that has

been for long-term solar evaporation in natural seawater showed that no salt crystals are blocking the water transport in the channel, which further confirms the results in Fig. 4-12.

Table 1 Comparison of performance of wood-based solar evaporation system.[27-29, 33, 49, 51-59]

Sample	**Q (sun)**	**v_e (kg m^{-2} h^{-1})**	**η**	**Reference**
Wood-TA-Fe^{3+}	1	1.8	90 %	Ref. 27
PPy-wood	1	1.014	72.5 %	Ref. 28
$CuFeSe_2$ NP-wood	1	1.05	67.7 %	Ref. 29
Bimodal wood evaporator	1	0.8	57 %	Ref. 33
Ink wood	1	1.6	74 %	Ref. 49
CDs-wood	1	1.18	79.5 %	Ref. 51
PDA-wood	1	1.38	87 %	Ref. 52
CNT wood	1	1.0	67.8 %	Ref. 53
Plasmonic wood	1	1.0	68 %	Ref. 54
self-regenerating wood	1	1.08	75 %	Ref. 55
MnO_2-wood	1	1.22	81.4 %	Ref. 56
Laser-treated wood	1	1.26	77 %	Ref. 57
Carbonization wood	1	1.3	89 %	Ref. 58
Wood@AIP	1	1.423	90.8 %	Ref. 59
PNPG wood	**1**	**1.64**	**90.4 %**	**This work**

Table 2 Comparison of cost-effectiveness over previous reported solar evaporators.[12, 39, 60-67]

Absorber	Floating material	v_e (kg m^{-2} h^{-1})	η	Cost ($/m^2)	Ref.
Ti_2O_3 NPs	PVA hydrogel	3.6	/	293.21	Ref. 12
Treated Cu mesh	Cu Mesh	0.7	/	110.34	Ref. 39
GO/CNTs	3D origami	1.59	71%	36.97	Ref. 60
Graphite flakes	Carbon foam	1.2	64%	205.07	Ref. 61
Polypyrrole	Airlaid paper	1.35	92%	20	Ref. 62
Cu-CAT-1 MOF	Cu Mesh	1.5	/	190	Ref. 63
CNTs	Polycyclic octenes	1.26	83%	43	Ref. 64
MWCNTs	Cotton paper	0.674	43%	5.3	Ref. 65
Carbon Black	Polystyrene foam	0.6	53.9%	16.86	Ref. 66
AuNP@c-silica	Filter fiber paper	1.50	94.6%	>18	Ref. 67
PNPG	**Wood**	**1.64**	**90.4%**	**24.6**	**This work**

Further, to evaluate the desalination performance of the PNPG wood, natural seawater gathered from the Sea of Japan is used for solar evaporation. The water vapor was carefully collected into purified water during the solar evaporation process and tested for ion concentration and salinity (Fig. 4-11c). The concentrations of the main

metal ion in the water samples were tracked using ICP-OES. The four main metal ion concentrations in seawater display higher concentrations of 11500, 1070, 396, and 357 mg L^{-1} (Na^{+}, Mg^{2+}, K^{+}, and Ca^{2+}). By contrast, the corresponding ion concentrations were notably reduced to 2.92, 0.176, 1.21, and 1.23 mg L^{-1} in purified water. The results show that the ion content in the water sample is greatly decreased by 3~4 orders of magnitude after desalination. Similarly, the salinities of the purified water were significantly decreased, which were much lower than the WHO standard for drinking water. And the salt in natural seawater also rarely crystallized on the surface of the PNPG wood sample. Besides, the resistance value can intuitively display the purity of the water, which can be measured by a multimeter (Fig. 4-11d). The results show that ohmic values of seawater, purified water, and domestic water (boiled water) are 77.0 KΩ, 2.090 MΩ, and 1.189 MΩ, respectively, which indicated that it was excellent solar distillation.

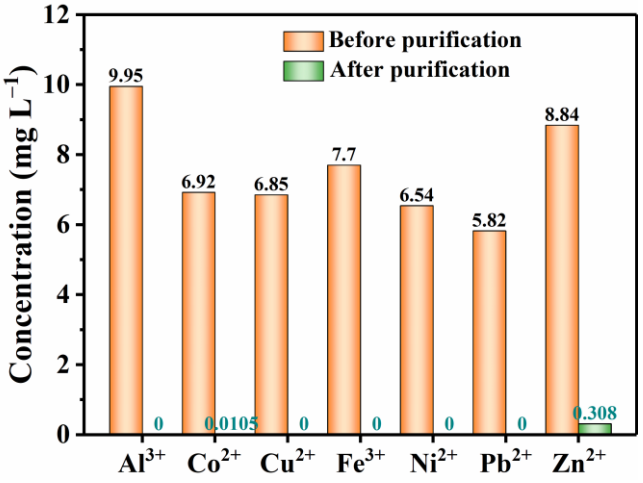

Fig. 4-14 Concentration changes of metal ions (Al^{3+}, Co^{2+}, Cu^{2+}, Fe^{3+}, Ni^{2+}, Pb^{2+}, and Zn^{2+}) in artificial wastewater before and after solar purification.

Next, the PNPG wood solar evaporation systems can be applied to sewage purification. The ions concentration of inartificial heavy metals wastewater (containing Al^{3+}, Co^{2+}, Cu^{2+}, Fe^{3+}, Ni^{2+}, Pb^{2+}, and Zn^{2+}) before and after solar evaporation were tested. As the results as shown in Fig. 4-14, after purification, the concentration of these heavy metal ions is much lower than that of the original artificial wastewater, demonstrating that photothermal evaporation has a strong removal effect on heavy metal ions. In addition, the results show that the distilled water from the MO, MB, and RhB solutions (10 mg L^{-1}) present a negligible absorbance, which proved PNPG wood evaporator has good solar purification capabilities (Figs. 7e–7g). All of the results show that PNPG wood has stable and lasting evaporation performance, and has high efficiency and potential in solar desalination and wastewater treatment applications.

4.4 Conclusion

In summary, inspired by the transpiration process of trees, a high-effective PNPG wood solar evaporator with the advantages of being cost-effective, convenient, and environment-friendly was developed by a simple drop-casting method. Due to natural water transport channels and low thermal conductivity of the wood, as well as the effective solar-heat conversion of PNPG, the PNPG wood solar evaporator has achieved rapid water transfer, excellent interface thermal positioning, and local heat management ability. Therefore, the PNPG wood evaporator has achieved solar efficiency of 90.4% under the 1 sun, which is better than most reported wood-based evaporators and shows exciting performance and cost-effective performance. Moreover, the evaporation rate can be well maintained for a long-term evaporation process, showing good reusability

and durability. Herein, such a well-designed, low cost cost-effective, and high-efficiency PNPG wood solar evaporation system has the potential to be applied to solve the practical problem of seawater desalination and water purification.

Reference

[1] C.J. Vorosmarty, A.Y. Hoekstra, S.E. Bunn, D. Conway, J. Gupta, WATER. Fresh water goes global, Science 349 (2015) 478-479.

[2] M.S. Mauter, I. Zucker, F.o. Perreault, J.R. Werber, J.-H. Kim, M. Elimelech, The role of nanotechnology in tackling global water challenges, Nat. Sustain. 1 (2018) 166-175.

[3] Y. Lu, N. Nakicenovic, M. Visbeck, A.S. Stevance, Policy: Five priorities for the UN Sustainable Development Goals, Nature 520 (2015) 432-433.

[4] B. Van der Bruggen, Sustainable implementation of innovative technologies for water purification, Nature Reviews Chemistry 5 (2021) 217-218.

[5] W. Shang, T. Deng, Solar steam generation: Steam by thermal concentration, Nat. Energy 1 (2016) 1-2.

[6] P. Tao, G. Ni, C. Song, W. Shang, J. Wu, J. Zhu, G. Chen, T. Deng, Solar-driven interfacial evaporation, Nat. Energy 3 (2018) 1031-1041.

[7] C. Chen, Y. Kuang, L. Hu, Challenges and Opportunities for Solar Evaporation, Joule 3 (2019) 683-718.

[8] Z. Wang, T. Horseman, A.P. Straub, N.Y. Yip, D. Li, M. Elimelech, S. Lin, Pathways and challenges for efficient solar-thermal desalination, Sci. Adv. 5 (2019) 763-776.

[9] F. Zhao, Y. Guo, X. Zhou, W. Shi, G. Yu, Materials for solar-powered water evaporation, Nat. Rev. Mater. 5 (2020) 388-401.

[10] M. Gao, L. Zhu, C.K. Peh, G.W. Ho, Solar absorber material and system designs for photothermal water vaporization towards clean water and energy production,

Energy Environ. Sci. 12 (2019) 841-864.

[11] F. Zhao, X. Zhou, Y. Shi, X. Qian, M. Alexander, X. Zhao, S. Mendez, R. Yang, L. Qu, G. Yu, Highly efficient solar vapour generation via hierarchically nanostructured gels, Nat. Nanotechnol. 13 (2018) 489-495.

[12] H. Ghasemi, G. Ni, A.M. Marconnet, J. Loomis, S. Yerci, N. Miljkovic, G. Chen, Solar steam generation by heat localization, Nat. Commun. 5 (2014) 4449-4465.

[13] X. Li, R. Lin, G. Ni, N. Xu, X. Hu, B. Zhu, G. Lv, J. Li, S. Zhu, J. Zhu, Three-dimensional artificial transpiration for efficient solar waste-water treatment, Natl. Sci. Rev. 5 (2018) 70-77.

[14] N. Xu, J. Li, Y. Wang, C. Fang, X. Li, Y. Wang, L. Zhou, B. Zhu, Z. Wu, S. Zhu, J. Zhu, A water lily-inspired hierarchical design for stable and efficient solar evaporation of high-salinity brine, Sci. Adv. 5 (2019) 7013-7021.

[15] Y. Shi, R. Li, Y. Jin, S. Zhuo, L. Shi, J. Chang, S. Hong, K.-C. Ng, P. Wang, A 3D Photothermal Structure toward Improved Energy Efficiency in Solar Steam Generation, Joule 2 (2018) 1171-1186.

[16] Z. Li, C. Wang, J. Su, S. Ling, W. Wang, M. An, Fast-Growing Field of Interfacial Solar Steam Generation: Evolutional Materials, Engineered Architectures, and Synergistic Applications, Solar RRL 3 (2019) 1800206-1800225.

[17] A.J. McElrone, B. Choat, G.A. Gambetta, C.R. Brodersen, Water uptake and transport in vascular plants, Nature Education Knowledge 4 (2013) 1-13.

[18] Z. Bo, H. Zhu, C. Ying, H. Yang, S. Wu, J. Kong, S. Yang, X. Wei, J. Yan, K. Cen, Tree-inspired radially aligned, bimodal graphene frameworks for highly efficient and

isotropic thermal transport, Nanoscale 11 (2019) 21249-21258.

[19] W. Li, Z. Chen, H. Yu, J. Li, S. Liu, Wood-Derived Carbon Materials and Light-Emitting Materials, Adv. Mater. (2020) 2000596-2000618.

[20] Q. Jiang, S. Singamaneni, Water from Wood: Pouring through Pores, Joule 1 (2017) 429-430.

[21] C. Chen, L. Hu, Nanoscale Ion Regulation in Wood-Based Structures and Their Device Applications, Adv. Mater. (2020) 2002890-2002918.

[22] C. Chen, Y. Kuang, S. Zhu, I. Burgert, T. Keplinger, A. Gong, T. Li, L. Berglund, S.J. Eichhorn, L. Hu, Structure–property–function relationships of natural and engineered wood, Nat. Rev. Mater. 5 (2020) 642-666.

[23] L. Zhu, M. Gao, C.K.N. Peh, G.W. Ho, Recent progress in solar-driven interfacial water evaporation: Advanced designs and applications, Nano Energy 57 (2019) 507-518.

[24] X. Dong, S. Gao, S. Li, T. Zhu, J. Huang, Z. Chen, Y. Lai, Bioinspired structural and functional designs towards interfacial solar steam generation for clean water production, Mater. Chem. Front. 5 (2021) 1510-1524.

[25] S. Cao, P. Rathi, X. Wu, D. Ghim, Y.S. Jun, S. Singamaneni, Cellulose Nanomaterials in Interfacial Evaporators for Desalination: A "Natural" Choice, Adv. Mater. (2020) 2000922-2000944.

[26] R. Fillet, V. Nicolas, V. Fierro, A. Celzard, A review of natural materials for solar evaporation, Sol. Energy Mater. Sol. Cells 219 (2021) 110814-110832.

[27] M. Zhu, Y. Li, F. Chen, X. Zhu, J. Dai, Y. Li, Z. Yang, X. Yan, J. Song, Y. Wang,

E. Hitz, W. Luo, M. Lu, B. Yang, L. Hu, Plasmonic Wood for High-Efficiency Solar Steam Generation, Adv. Energy Mater. 8 (2018) 1701028-1701035.

[28] H. Liu, C. Chen, H. Wen, R. Guo, N.A. Williams, B. Wang, F. Chen, L. Hu, Narrow bandgap semiconductor decorated wood membrane for high-efficiency solar-assisted water purification, J. Mater. Chem. A 6 (2018) 18839-18846.

[29] H. Jang, J. Choi, H. Lee, S. Jeon, Corrugated Wood Fabricated Using Laser-Induced Graphitization for Salt-Resistant Solar Steam Generation, ACS Appl. Mater. Interfaces 12 (2020) 30320-30327.

[30] Y. Zou, X. Chen, P. Yang, G. Liang, Y. Yang, Z. Gu, Y. Li, Regulating the absorption spectrum of polydopamine, Sci. Adv. 6 (2020) 4696-4979.

[31] F. Ni, P. Xiao, N. Qiu, C. Zhang, Y. Liang, J. Gu, J. Xia, Z. Zeng, L. Wang, Q. Xue, T. Chen, Collective behaviors mediated multifunctional black sand aggregate towards environmentally adaptive solar-to-thermal purified water harvesting, Nano Energy 68 (2020) 104311-104321.

[32] X. Zhou, Y. Guo, F. Zhao, G. Yu, Hydrogels as an Emerging Material Platform for Solar Water Purification, Acc. Chem. Res. 52 (2019) 3244-3253.

[33] X. Wu, G.Y. Chen, W. Zhang, X. Liu, H. Xu, A Plant-Transpiration-Process-Inspired Strategy for Highly Efficient Solar Evaporation, Adv. Sustain. Syst. 1 (2017) 1700046-1700053.

[34] Y. Zou, X. Chen, W. Guo, X. Liu, Y. Li, Flexible and Robust Polyaniline Composites for Highly Efficient and Durable Solar Desalination, ACS Appl. Energy Mater. 3 (2020) 2634-2642.

[35] Z. Li, X. Ma, D. Chen, X. Wan, X. Wang, Z. Fang, X. Peng, Polyaniline‐Coated MOFs Nanorod Arrays for Efficient Evaporation‐Driven Electricity Generation and Solar Steam Desalination, Sci. Adv. (2021) 2004552-2004562.

[36] H.-H. Yu, L.-J. Yan, Y.-C. Shen, S.-Y. Chen, H.-N. Li, J. Yang, Z.-K. Xu, Janus Poly(Vinylidene Fluoride) Membranes with Penetrative Pores for Photothermal Desalination, Research 2020 (2020) 1-10.

[37] L. Zong, M. Li, C. Li, Intensifying solar-thermal harvest of low-dimension biologic nanostructures for electric power and solar desalination, Nano Energy 50 (2018) 308-315.

[38] J. Chen, B. Li, G. Hu, R. Aleisa, S. Lei, F. Yang, D. Liu, F. Lyu, M. Wang, X. Ge, F. Qian, Q. Zhang, Y. Yin, Integrated Evaporator for Efficient Solar-Driven Interfacial Steam Generation, Nano Lett. 20 (2020) 6051-6058.

[39] X. Wang, Q. Liu, S. Wu, B. Xu, H. Xu, Multilayer Polypyrrole Nanosheets with Self-Organized Surface Structures for Flexible and Efficient Solar-Thermal Energy Conversion, Adv. Mater. 31 (2019) 1807716-1807725.

[40] B.P. Jiang, L. Zhang, X.L. Guo, X.C. Shen, Y. Wang, Y. Zhu, H. Liang, Poly(n-phenylglycine)-based nanoparticles as highly effective and targeted near-infrared photothermal therapy/photodynamic therapeutic agents for malignant melanoma, Small 13 (2017) 1602496-1602510.

[41] C. Ruan, C. Liu, H. Hu, X.L. Guo, B.P. Jiang, H. Liang, X.C. Shen, NIR-II light-modulated thermosensitive hydrogel for light-triggered cisplatin release and repeatable chemo-photothermal therapy, Chem Sci 10 (2019) 4699-4706.

[42] H. Chen, W. Liang, Y. Zhu, Z. Guo, J. Jian, B.P. Jiang, H. Liang, X.C. Shen, Supercharged fluorescent protein functionalized water-soluble poly(N-phenylglycine) nanoparticles for highly effective imaging-guided photothermal therapy, Chem. Commun. 54 (2018) 10292-10295.

[43] L. Xiao, X. Chen, X. Yang, J. Sun, J. Geng, Recent Advances in Polymer-Based Photothermal Materials for Biological Applications, ACS Appl. Polym. Mater. 2 (2020) 4273-4288.

[44] Z. Lin, T. Wu, J. Shi, B. Zhou, C. Zhu, Y. Wang, R. Liang, M. Mizuno, Poly(N-phenylglycine)-Based Bioinspired System for Stably and Efficiently Enhancing Solar Evaporation, ACS Sustainable Chem. Eng. 9 (2021) 448-457.

[45] Z. Lin, T. Wu, Y.F. Feng, J. Shi, B. Zhou, C. Zhu, Y. Wang, R. Liang, M. Mizuno, Poly(N-phenylglycine)/MoS2 Nanohybrid with Synergistic Solar-Thermal Conversion for Efficient Water Purification and Thermoelectric Power Generation, ACS Appl. Mater. Interfaces 14 (2022) 1034-1044.

[46] X. Li, G. Ni, T. Cooper, N. Xu, J. Li, L. Zhou, X. Hu, B. Zhu, P. Yao, J. Zhu, Measuring Conversion Efficiency of Solar Vapor Generation, Joule 3 (2019) 1798-1803.

[47] L. Zhang, B. Tang, J. Wu, R. Li, P. Wang, Hydrophobic Light-to-Heat Conversion Membranes with Self-Healing Ability for Interfacial Solar Heating, Adv. Mater. 27 (2015) 4889-4894.

[48] Z.C. Xiong, Y.J. Zhu, D.D. Qin, F.F. Chen, R.L. Yang, Flexible Fire-Resistant Photothermal Paper Comprising Ultralong Hydroxyapatite Nanowires and Carbon Nanotubes for Solar Energy-Driven Water Purification, Small 14 (2018) 1803387.

[49] Z. Wang, Y. Yan, X. Shen, C. Jin, Q. Sun, H. Li, A wood–polypyrrole composite as a photothermal conversion device for solar evaporation enhancement, J. Mater. Chem. A 7 (2019) 20706-20712.

[50] J. Yang, Y. Chen, X. Jia, Y. Li, S. Wang, H. Song, Wood-Based Solar Interface Evaporation Device with Self-Desalting and High Antibacterial Activity for Efficient Solar Steam Generation, ACS Appl. Mater. Interfaces 12 (2020) 47029-47037.

[51] F. He, M. Han, J. Zhang, Z. Wang, X. Wu, Y. Zhou, L. Jiang, S. Peng, Y. Li, A simple, mild and versatile method for preparation of photothermal woods toward highly efficient solar steam generation, Nano Energy 71 (2020) 104650-104660.

[52] S. He, C. Chen, Y. Kuang, R. Mi, Y. Liu, Y. Pei, W. Kong, W. Gan, H. Xie, E. Hitz, C. Jia, X. Chen, A. Gong, J. Liao, J. Li, Z.J. Ren, B. Yang, S. Das, L. Hu, Nature-inspired salt resistant bimodal porous solar evaporator for efficient and stable water desalination, Energy Environ. Sci. 12 (2019) 1558-1567.

[53] X.-F. Zhang, Z. Wang, L. Song, Y. Feng, J. Yao, Chinese ink enabled wood evaporator for continuous water desalination, Desalination 496 (2020) 114727-114734.

[54] W. Chao, Y. Li, X. Sun, G. Cao, C. Wang, S.-H. Ho, Enhanced wood-derived photothermal evaporation system by in-situ incorporated lignin carbon quantum dots, Chem. Eng. J. 405 (2021) 126703-126715.

[55] Y. Wang, H. Liu, C. Chen, Y. Kuang, J. Song, H. Xie, C. Jia, S. Kronthal, X. Xu, S. He, L. Hu, All Natural, High Efficient Groundwater Extraction via Solar Steam/Vapor Generation, Adv. Sustain. Syst. 3 (2019) 1800055-1800060.

[56] Y. Kuang, C. Chen, S. He, E.M. Hitz, Y. Wang, W. Gan, R. Mi, L. Hu, A High-

Performance Self-Regenerating Solar Evaporator for Continuous Water Desalination, Adv. Mater. 31 (2019) 1900498-1900506.

[57] D. Li, D. Han, C. Guo, C. Huang, Facile Preparation of MnO2-Deposited Wood for High-Efficiency Solar Steam Generation, ACS Appl. Energy Mater. 4 (2021) 1752-1762.

[58] Z. Chen, B. Dang, X. Luo, W. Li, J. Li, H. Yu, S. Liu, S. Li, Deep Eutectic Solvent-Assisted In Situ Wood Delignification: A Promising Strategy To Enhance the Efficiency of Wood-Based Solar Steam Generation Devices, ACS Appl. Mater. Interfaces 11 (2019) 26032-26037.

[59] T. Chen, Z. Wu, Z. Liu, J.T. Aladejana, X.A. Wang, M. Niu, Q. Wei, Y. Xie, Hierarchical Porous Aluminophosphate-Treated Wood for High-Efficiency Solar Steam Generation, ACS Appl. Mater. Interfaces 12 (2020) 19511-19518.

[60] Y. Guo, X. Zhou, F. Zhao, J. Bae, B. Rosenberger, G. Yu, Synergistic Energy Nanoconfinement and Water Activation in Hydrogels for Efficient Solar Water Desalination, ACS Nano 13 (2019) 7913-7919.

[61] C. Chang, P. Tao, J. Xu, B. Fu, C. Song, J. Wu, W. Shang, T. Deng, High-Efficiency Superheated Steam Generation for Portable Sterilization under Ambient Pressure and Low Solar Flux, ACS Appl. Mater. Interfaces 11 (2019) 18466-18474.

[62] S. Hong, Y. Shi, R. Li, C. Zhang, Y. Jin, P. Wang, Nature-Inspired, 3D Origami Solar Steam Generator toward Near Full Utilization of Solar Energy, ACS Appl. Mater. Interfaces 10 (2018) 28517-28524.

[63] Q. Ma, P. Yin, M. Zhao, Z. Luo, Y. Huang, Q. He, Y. Yu, Z. Liu, Z. Hu, B. Chen,

H. Zhang, MOF-Based Hierarchical Structures for Solar-Thermal Clean Water Production, Adv. Mater. 31 (2019) 1808249-1808255.

[64] L. Zhao, L. Wang, J. Shi, X. Hou, Q. Wang, Y. Zhang, Y. Wang, N. Bai, J. Yang, J. Zhang, B. Yu, C.F. Guo, Shape-Programmable Interfacial Solar Evaporator with Salt-Precipitation Monitoring Function, ACS Nano 15 (2021) 5752-5761.

[65] D. Li, Q. Zhou, G. Wang, H. Zhao, S. Ma, K. Leng, Y. Wang, J. Bai, Assembly of Janus complex with low-cost and salt rejection for solar-thermal water evaporation, J. Mater. Sci. 55 (2020) 15551-15561.

[66] L. Chen, H. Wang, S. Kuravi, K. Kota, Y.H. Park, P. Xu, Low-cost and reusable carbon black based solar evaporator for effective water desalination, Desalination 483 (2020) 114412-114425.

[67] R. Cui, J. Wei, C. Du, S. Sun, C. Zhou, H. Xue, S. Yang, Engineering trace AuNPs on monodispersed carbonized organosilica microspheres drives highly efficient and low-cost solar water purification, J. Mater. Chem. A 8 (2020) 13311-13319.

Chapter 5 Poly(N-phenylglycine)/MoS_2 nanohybrid with synergistic solar-thermal conversion for efficient water purification and thermoelectric power generation

5.1 Introduction

Energy and water shortages are major global problems that are often interconnected.[1, 2] Researchers are presently exploring abundant, sustainable solar energy to drive the rapid evaporation of seawater or sewage while producing fresh water and thermoelectric power generation.[3-6] However, conventional solar energy conversion-driven steam generation is relatively inefficient due to the underutilization of solar energy and inevitable heat loss. In recent years, solar interfacial evaporation has garnered increasing attention as an economical and effective method. In this method, solar evaporators integrated with photothermal conversion materials provide locally concentrated heat and generate steam quickly.[7-10] Solar evaporators must demonstrate i) good solar light absorption and excellent solar-thermal conversion capacity, ii) outstanding thermal management (allowing heat to be located at the water evaporation interface), and iii) excellent water supply capacity to fully transport water to the evaporation interface. Thus far, significant progress has been made in the development of photothermal conversion materials for the solar evaporator, including semiconductors,[11] metallics,[12] carbon materials,[13] macromolecules[14] and

biomass materials,[15] *et al.* Solar evaporation efficiency has been proven superior to conventional bulk heating. However, although solar interfacial evaporation has achieved remarkable success in freshwater production, it is still a practical challenge to integrate the above features into a single evaporation system.

Transition metal dichalcogenide (TMDs) nanomaterials, especially MoS_2, have attracted tremendous attention due to their good light absorption properties, easy compound processing, natural abundance, and relatively low cost.[16-19] MoS_2 nanosheets are widely considered to be one of the most promising materials for solar water purification because of their strong solar radiation absorption (>70%) accomplished by leveraging on the resonant photonic structure.[20] Recently, Jun *et al.* reported using MoS_2/BNC bilayer aerogels for solar thermal water purification, achieving evaporation efficiency of 76% and 81% with 0.76 kW m^{-2} and 5.35 kW m^{-2} irradiation, respectively. [21] Wang *et al.* utilized a novel MoS_2-based 3D evaporator for solar desalination, realizing an efficiency of 85% using 1 kW m^{-2}. [22] Despite these advancements, the evaporation performance of MoS_2 as a single photothermal absorber and its solar-thermal efficiency is still unsatisfactory. Given this, constructing a system with a synergistic photothermal effect is still an effective method for improving solar-thermal efficiency and evaporation performance.[23,24]

In recent years, it has been widely reported that photothermal polymers (such as polyaniline, polydopamine, and polypyrrole) combined with other photothermal materials to obtain synergistic enhancement of photothermal properties.[25-27] As a competitive photothermal polymer material, PNPG is chemically stable, conductive,

easily prepared, and provides good light absorption performance. [28,29] Therefore, it is assumed that if another photothermal material such as MoS_2 was combined with PNPG, more effective enhanced synergistic photothermal conversion could be obtained. However, thus far, as solar evaporation is a new branch of solar-thermal application, the synergistic photothermal effect of PNPG has not been reported.

In addition, in the process of water evaporation, there will inevitably be a certain amount of residual heat, resulting in the decline of solar heat conversion utilization. .[30, 31] To utilize solar heat more effectively, recovery of the diffused waste heat is an important research focus. Thermoelectricity generation is a promising method for waste heat recovery because it can convert heat directly into electricity without environmental pollution. Recently, with the use of thermoelectric modules, some new strategies have been proposed to collect and further utilize waste heat. [32, 33] For example, Zhu et al. developed a strategy to store and recycle steam enthalpy during the solar evaporation process while producing clean water (evaporation efficiency 72.2%) and thermoelectricity power (energy efficiency 1.23%) using 30 kW m^{-2} irradiation. [34] Ho et al. constructed a device coupling a shape conformal 3D sponge with a TE module that converted waste energy into thermoelectricity, achieving 87.4% evaporation efficiency and 0.4 W m^{-2} output power under one sun. [35] Chen et al. designed a CNT paper solar–thermoelectric generation system that demonstrated a 1.28 kg m^{-2} h^{-1} evaporation rate and 83.3% efficiency under one sun, and generated power with an output voltage of 100 mV. [36] Therefore, the synergistic coupling of thermal management and power generation in solar evaporation progress holds great promise

as an attractive approach to simultaneously producing clean water and electricity.

Herein, a stable PNPG/MoS_2 nanohybrid was constructed via electrostatically induced self-assembly of negative MoS_2 and positive PNPG and then prepared into a photothermal membrane, which was applied to simultaneous solar water purification–thermoelectric power generation (Fig. 5-1). Due to the synergistic photothermal enhancement effect by PNPG and MoS_2, the PNPG/MoS_2 nanohybrid system shows excellent solar absorption capacity. As a result, the evaporation rate of a PNPG/MoS_2 solar water purification system was 1.65 kg m^{-2} h^{-1} with an efficiency of 90.1% under 1 kW m^{-2} solar irradiation. In addition, the solar evaporation–thermoelectricity generating system operated using an open circuit with +110 mV voltage and 0.23 W m^{-2} maximum output density under 1 kW m^{-2}. An evaporation rate of 1.70 kg m^{-2} h^{-1} was obtained, and the evaporation efficiency was improved to 92.9%, indicating that the TE module can also be a heat insulator to improve evaporator performance. Such a well-designed system provides a practicable approach to using solar-thermal technology and guidance to manage the challenges of clean water and green energy.

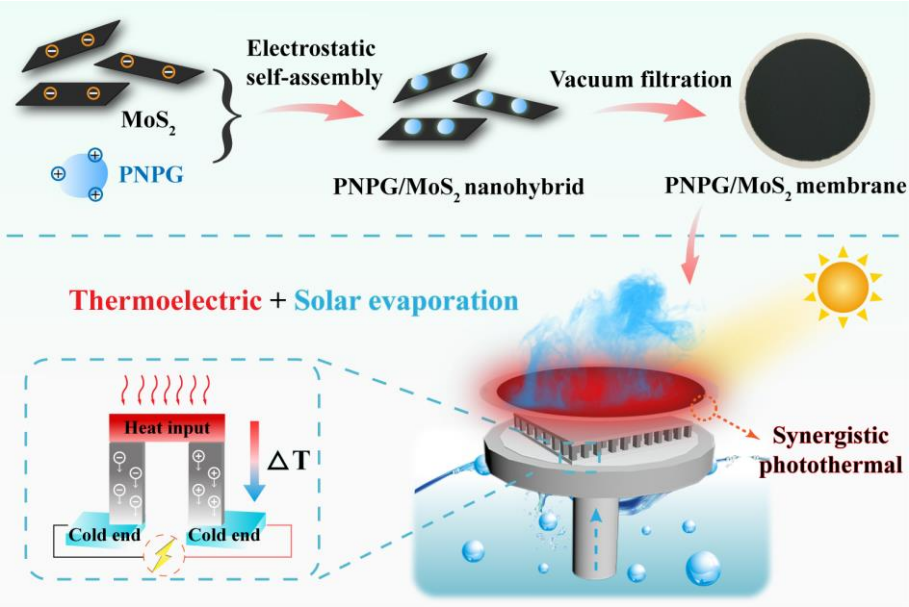

Fig. 5-1 Schematic of PNPG/MoS_2 solar evaporation–thermoelectric power generation system.

5.2 Experimental

5.2.1 Reagents and materials

N-phenylglycine (NPG, >97.0%) was bought from Tokyo Chemical Industry (Japan). High Purity Materials Kojundo Chemical Lab Co., Ltd (Japan) provided MoS_2 powder (99.9%). Tannic acid (TA, ≤100%), HCl (35.0~37.0%), ammonium persulfate (APS, 98.0%), methylene blue (MB, 98.5%), methyl orange (MO, ≤100%), and rhodamine B (RhB, ≤100%) were provided by Fujifilm Wako Pure Chemical (Japan). Hydrophilic PVDF membranes were acquired from Merck Millipore (USA). The ultrapure water was produced by Yamato WG 250 (Japan).

5.2.2 TA-assisted aqueous exfoliation of MoS_2 nanomaterial

The aqueous exfoliation process of MoS_2 was performed with the assistance of TA using a 250 W ultrasonic cell crusher (Branson Sonifier 250, USA). Briefly, 120 mg of

MoS_2 powder was added to 60 mL (1 mg L^{-1}) aqueous TA solution, and the suspension was sonicated for 3 h. Finally, the MoS_2 nanosheets in the supernatant were collected after 15 min centrifugation at 3000 rpm to remove the MoS_2 bulk. Ultrapure water was used in the exfoliation experiments to prevent the aggregation of the exfoliated nanosheets.

5.2.3 Preparation of PNPG nanoparticles

PNPG was prepared by polymerization from the NPG monomer. The APS solution was added to the NPG solution. The polymerization process was performed using an ice-water bath method for 24 h. The prepared sample was washed several times with ultra-pure water to remove impurities, and the PNPG was re-dispersed into the water with ultrasonication and kept at 4 ℃.

5.2.4 Preparation of the PNPG/MoS_2 solar evaporation device

We obtained the PNPG/MoS_2 nanohybrid by mixing the PNPG and MoS_2 (both 1 mg mL^{-1}) suspensions in specific ratios then dispersing them for 30 min using ultrasonication. The PNPG/MoS_2 nanohybrid (total mass, 5 mg) with mass ratios of 1:4, 1:2, 1:1, 2:1, and 4:1 was obtained. Finally, the PNPG/MoS_2 nanohybrid was fixed onto a blank PVDF membrane by vacuum filtration to prepare the PNPG/MoS_2 photothermal membrane. The obtained PNPG/MoS_2 photothermal membrane was dried at room temperature for 12 h.

Then, a solar desalination device was assembled using a PNPG/MoS_2 photothermal membrane, thermal insulation polystyrene (PS) foam, a water-trapped layer, and a water channel made of cotton. The thermal insulation foam supports the

PNPG/MoS_2 membrane and the thermoelectric device floating on water. The cotton layer and cotton water supply channel ensured a continuous water supply for the evaporation process.

5.2.5 Characterization

TEM (Hitachi HT-7700) and SEM (Hitachi S-4300) images of the nanomaterials and membranes were obtained. The Shimadzu UV-3600 spectrophotometer (Japan) was used to obtain the UV-vis-NIR spectrum. Using PerkinElmer Spectrum Two N (USA), the FT-IR spectra (400 cm^{-1} to 4000 cm^{-1}) were collected. Contact angles were determined using the Kyowa Interface Science DMs-401 device (Japan). A Zeta Plus analyzer (Brookhaven Instruments, USA) was used to study the zeta potential. IR maps and temperature distributions were monitored by a thermal imager (FLIR One Pro, USA). Cation concentrations were determined using Shimadzu ICPE-9000 (Japan).

5.2.6 Solar water purification experiments

The solar water purification and sewage treatment experiments were performed using an XES-40S3-TT solar simulator (SAN-EI Electric, Japan). The laboratory temperature was maintained at approximately 25 °C with 60% humidity. The real-time water mass changes were recorded using an FX-200GD electronic balance (A&D Company, Japan). The efficiency (η) of solar-thermal conversion during solar evaporation was calculated using the following equation:

$$\eta = (m-m_0)h_v/C_{opt}P_0 \quad (1)$$

The solar evaporation rate is denoted as m, the natural evaporation rate (in the dark) is denoted as m_0, and the liquid-vapor phase change enthalpy is represented by h_v, [37]

the optical concentration is C_{opt}, and P_0 represents the power density (1 kW m^{-2}).

5.2.7 Thermoelectricity generation during solar evaporation

Utilizing the temperature difference created by the top solar absorber and the cold water-trapped layer, a commercial 30 × 30 mm TE module (ET-127-10-13-RS, made in Russia) was used to generate thermoelectricity. The TE module was placed between the PNPG/MoS_2 membrane and the cotton water-trapped layer, and the device floated on water due to the support of the PS insulator. The cotton water-trapped layer was in direct contact with the TE module to establish the cold end, and the PNPG/MoS_2 membrane on the top side was exposed to solar light to establish the hot end. The electrical measurements were conducted using a Keithley DDM6500 (Tektronix, USA), and a 3 Ω external resistance was connected to the TE module to measure the power output. The loading current was recorded, and the output density was calculated using the equation:

$$P = I^2R \quad (2)$$

Where P is the output power, I is the loading current, and R is external resistance.

5.3. Results and discussion

5.3.1 Fabrication and characterization of the PNPG/MoS_2 nanohybrid

The preparation of the PNPG/MoS_2 nanohybrid is demonstrated in Fig. 5-2a. The PNPG/MoS_2 nanohybrid was constructed via electrostatically induced self-assembly of negative potential MoS_2 with a positive potential PNPG. The microstructure evolution and material component were then analyzed. The morphology and structure of MoS_2,

PNPG, and the PNPG/MoS_2 nanohybrid were obtained by TEM. The delaminated MoS_2 nanosheets were extremely thin and transparent with a transverse size of approximately 200 nm (Fig. 5-2b). PNPG appeared as approximately 200 nm short rod-like nanoparticles in aggregations (Fig. 5-2c). The PNPG/MoS_2 nanohybrid appeared in the inherent shape profile of PNPG covered with MoS_2 nanosheets (Fig. 5-2d). The PNPG/MoS_2 nanocomposite surface was much rougher than that of MoS_2 due to the interaction between PNPG and MoS_2.

PNPG/MoS_2 was characterized structurally by XRD (Fig. 5-2e). The diffraction peaks at $2\theta = 14.30°$, 32.50°, 39.40°, 44.08°, 49.62°, and 58.27° were classified as (002), (100), (103), (006), (105), and (110) diffraction planes of MoS_2 (JCPD card, PDF#37-1492).[38] These distinct characteristic diffraction characteristics indicate the crystal properties of MoS_2. However, compared to MoS_2, the spectra of PNPG/MoS_2 nanohybrid had a wide diffraction pattern at $2\theta = 15°$ to 35°, which corresponds to the amorphous characteristics of PNPG. These results indicate that PNPG was successfully integrated into the MoS_2 nanosheets, consistent with the TEM results.

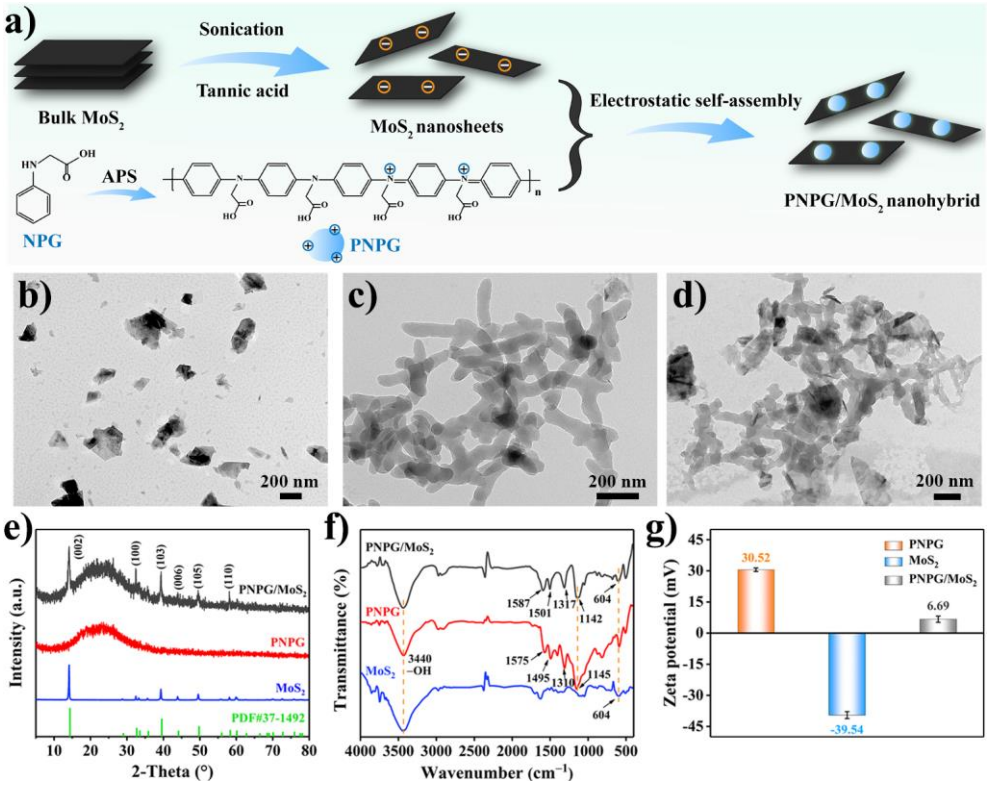

Fig. 5-2 (a) Schematic of PNPG/MoS_2 nanohybrid preparation. TEM images of (b) MoS_2, (c) PNPG, and (d) PNPG/MoS_2 nanohybrid. (e) XRD patterns, (f) FT-IR spectra, (g) Zeta potential of MoS_2, PNPG, and PNPG/MoS_2 nanohybrid.

The successful functionalization of PNPG with MoS_2 is also supported by FT-IR spectra (Fig. 5-2f). The broadband at 3440 cm^{-1} was assigned to the –OH group. The MoS_2 had a Mo–S vibration peak at 604 cm^{-1}, and this peak remained unchanged in PNPG/MoS_2. [39] The vibration peak at 1145 cm^{-1} corresponds to the PNPG backbone charge delocalization. The characteristic peaks around 1575 and 1495 cm^{-1} were assigned to the C=O stretching patterns of quinoid and benzene rings. Also, the band around 1310 cm^{-1} corresponds to the stretching vibration of C–N connected to the quinoid and benzenoid ring, confirming PNPG with a form of doping.[29] Notably, in PNPG/MoS_2, these peaks further shifted to 1587 cm^{-1}, 1501 cm^{-1}, and 1317cm^{-1},

indicating delocalization of polarons with MoS_2. All position changes of the characteristic FT-IR bands of PNPG in MoS_2 indicate the presence of some interaction between MoS_2 and PNPG.

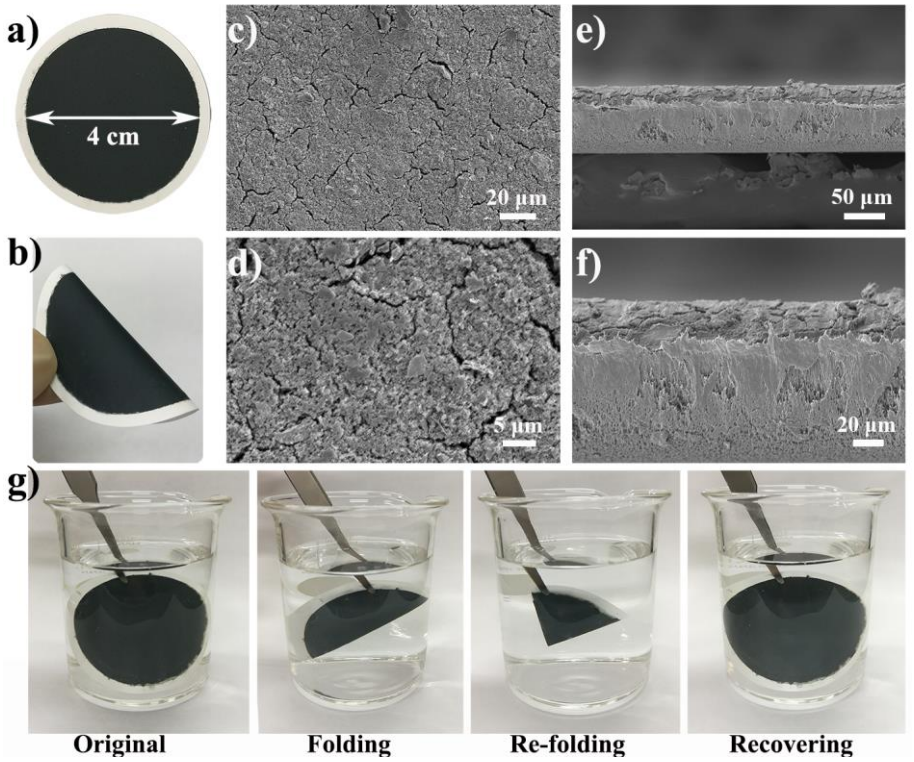

Fig. 5-3 (a) The PNPG/MoS_2 membrane and (b) a bent PNPG/MoS_2 membrane. (c) The top view SEM photo of the PNPG/MoS_2 membrane and (d) the amplified surface coating structure. (e) The cross-section SEM photo of the PNPG/MoS_2 membrane and (f) the amplified PNPG/MoS_2 coating. (g) The physical stability of the PNPG/MoS_2 membrane folded multiple times underwater.

The interaction mechanism of components in the PNPG/MoS_2 nanohybrid was shown to be mainly through electrostatic interaction according to the zeta potential measurement. As shown in Fig. 5-2g, the net charges of PNPG and MoS_2 dispersions were 30.52 mV and -39.54 mV, respectively. When PNPG and MoS_2 were stabilized at

a solute mass ratio of 2:1, the zeta potential was determined to be 6.69 mV. The above experimental results show that PNPG and MoS_2 are steadily hybridized through electrostatic interactions, further supported by the drift of characteristic peaks in FT-IR spectra.

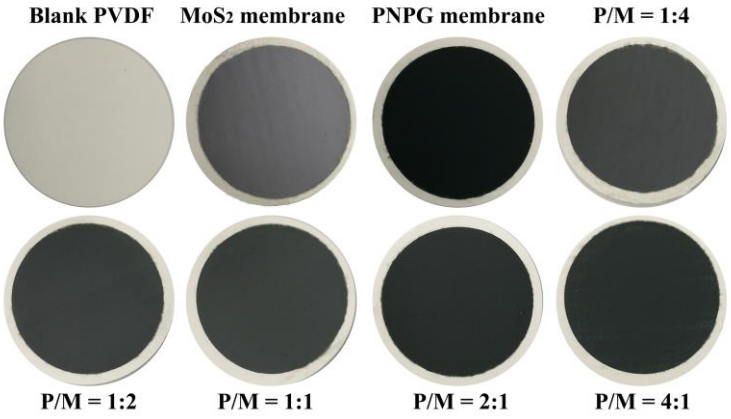

Fig. 5-4 Photograph of the photothermal membrane with the different mass ratios of PNPG to MoS_2.

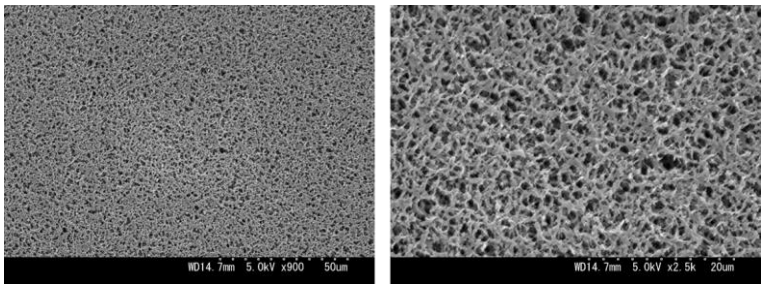

Fig. 5-5 SEM images of the top surface of blank PVDF membrane and a magnified image of the microstructure.

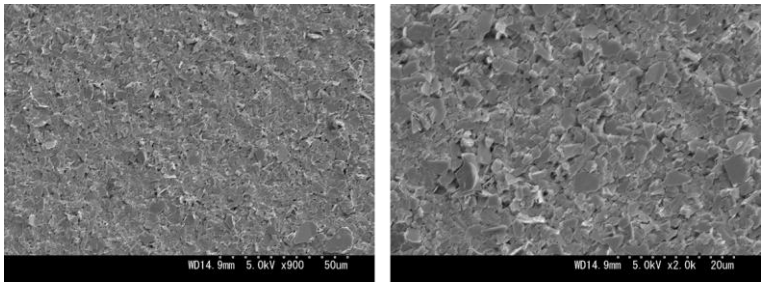

Fig. 5-6 SEM images of the top surface of the MoS_2 membrane and a magnified image

of the microstructure.

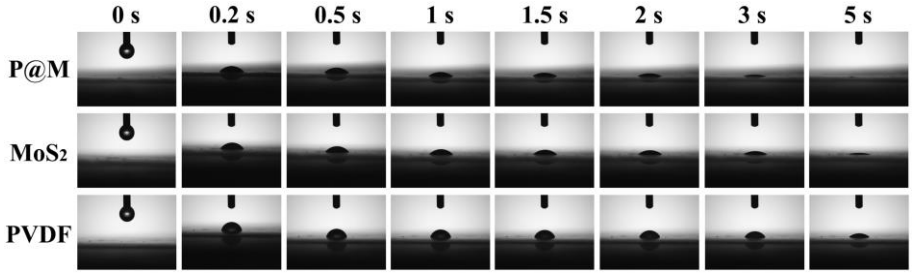

Fig. 5-7 Water contact angles of PNPG/MoS_2 membrane, MoS_2 membrane, and pure PVDF membrane over time.

We tested the PNPG/MoS_2 nanohybrid for solar water purification by loading the nanohybrid onto a hydrophilic PVDF membrane. As shown in Fig. 5-3a, the PNPG/MoS_2 nanohybrid was prepared for the photothermal membrane via vacuum filtration with a PNPG/MoS_2 coating 4 cm in diameter. Due to the assembled structure, the PNPG/MoS_2 nanohybrid can easily accumulate and form a hydrophilic coating. For comparison, multiple mass ratios of PNPG to MoS_2 membranes were prepared, and the membranes with slight color differences are exhibited in Fig. 5-4. SEM was conducted to observe the PNPG/MoS_2 coating of the membrane. Compared to the original PVDF (Fig. 5-5), a PNPG/MoS_2 coating can be observed. Notably, the PNPG/MoS_2 layer forms a rough surface and wide channels due to the interaction between PNPG and MoS_2, which is conducive to reducing light reflection and solar steam diffusion (Fig. 5-3 c and d). This observation contrasts with that of MoS_2 being stacked tightly in the MoS_2 membrane (Fig. 5-6). Moreover, from the cross-section, the PNPG/MoS_2 is also observed deposited on PVDF, forming a thin top photothermal layer of several micrometers (Fig. 5-3 e and f). Furthermore, the surface wettability of the photothermal

membrane can seriously affect water transport and solar evaporation. As Fig. 5-3b and 5-7 show, the PNPG/MoS_2 membrane exhibited good hydrophilicity and excellent flexibility. Moreover, the PNPG/MoS_2 film can be immersed in water and folded many times. It can also be released and returned to its original form, showing good structural integrity and stability (Fig. 5-3g). These results suggest that the PNPG/MoS_2 membrane provides a rapid water supply and sufficient interfacial evaporation characteristics.

5.3.2 Evaporation acceleration by PNPG/MoS_2 system

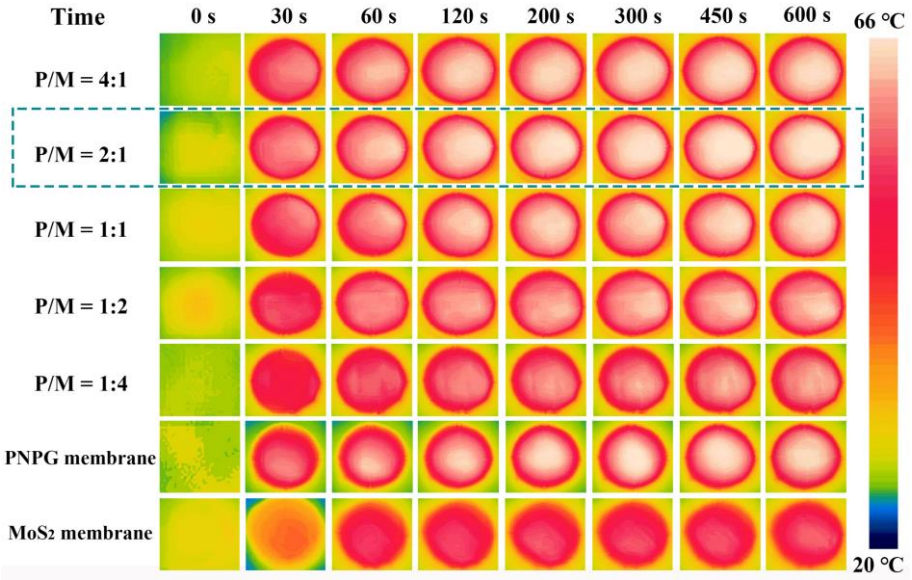

Fig. 5-8 IR images of the photothermal membrane with the different mass ratios of PNPG to MoS_2 over time.

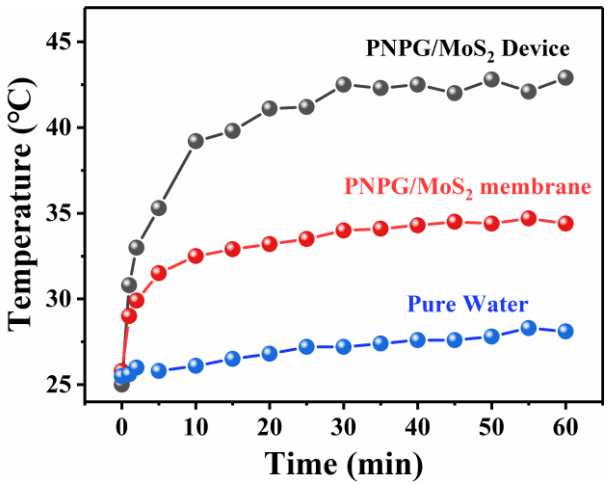

Fig. 5-9 Temperature change of the PNPG/MoS_2 device, PNPG/MoS_2 membrane only and pure water at various time points.

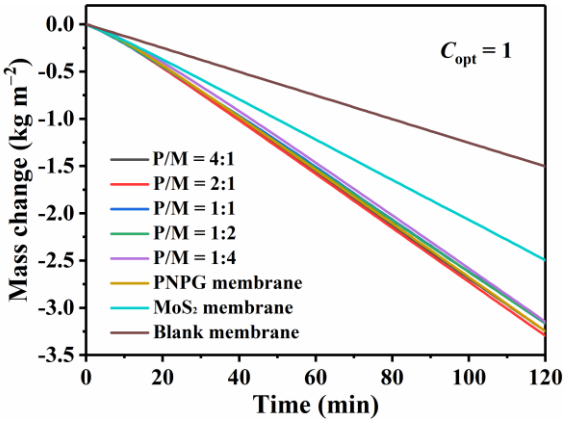

Fig. 5-10 Curves of water mass change of the photothermal membrane system with the different mass ratios of PNPG to MoS_2.

We evaluated the photothermal performance of the system after constructing the evaporator, as shown in Fig. 5-11a. The apparatus consisted of the PNPG/MoS_2 membrane, water-trapped layer, PS insulator, and water channel. The solar-thermal conversion capability of the photothermal membrane plays a crucial role in improving the efficiency of solar water purification. For this reason, the solar-thermal behavior of the photothermal membranes with the different mass ratios of PNPG to MoS_2 was

studied under 1 kW m^{-2}. Fig. 5-8 and 5-11c show that the temperature rose rapidly under solar irradiation. It then stabilized and remained at this level after 300 s. The results indicated the best synergistic solar-thermal effect at a mass ratio of 2:1. In contrast, under the same irradiation conditions, the solar-thermal effect of a single material coating membranes was relatively weaker, and for blank PVDF, the effect can be negligible. Moreover, PNPG/MoS_2 in a mass ratio of 2:1 demonstrated superior evaporation performance, confirming the photothermal steam conversion capability (Fig. 5-10). The 2:1 membrane ratio was used in the follow-up experiments, hereafter referred to as the PNPG/MoS_2 membrane.

The capability of the PNPG/MoS_2 membrane to absorb sunlight was measured by UV-vis-NIR spectra. As Fig. 5-11b shows, since the blank membrane reflected the majority of incoming solar radiation, it had a weak sunlight absorption capacity. The full band absorption of the PNPG/MoS_2 membrane can be observed after coating with the PNPG/MoS_2 nanohybrid layer. This enhanced absorption confirmed the high solar-heat conversion effect observed in the previous experiment. The membrane was then assembled into a solar evaporation device (Fig. 5-11a). We removed the PS insulator from the groove and inserted a cotton layer. The photothermal film was then placed between the PS insulator insulation layer and the cotton water-trapped layer; meanwhile, the cotton water channel continuously transported water to the water-trapping layer. The evaporator structure ensured a continuous water supply to the photothermal membrane and good thermal management.

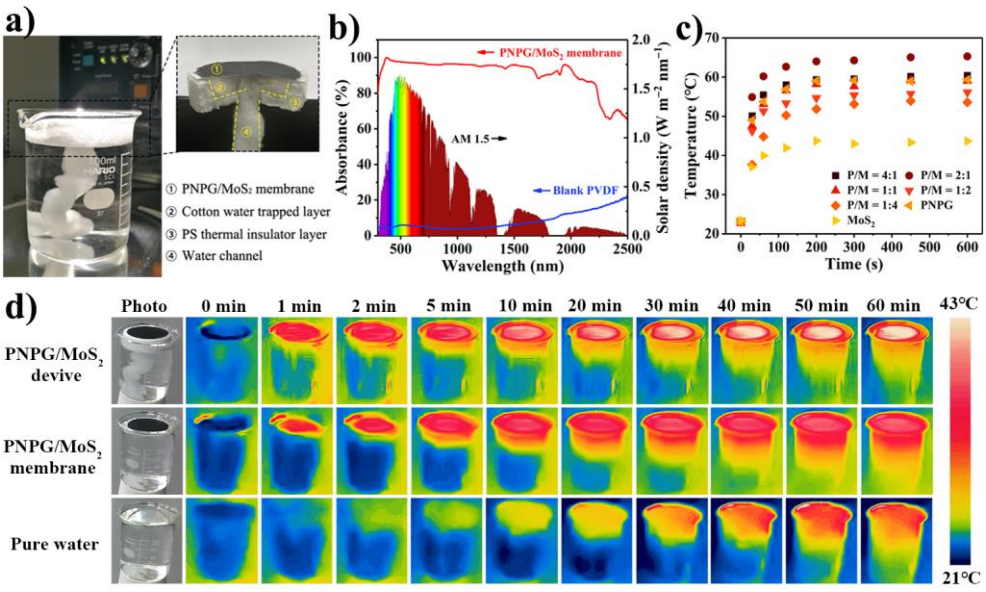

Fig. 5-11 (a) Structure images of the PNPG/MoS_2 solar evaporation device. (b) The UV-vis-NIR spectrum of the blank and PNPG/MoS_2 membrane. (c) The membrane temperature change with different mass ratios of PNPG to MoS_2 (represented by P/M) over time. (d) The thermal images of the PNPG/MoS_2 device, PNPG/MoS_2 membrane, and pure water under one sun irradiation at various time points.

The performance of the PNPG/MoS_2 device was further investigated, and for comparison, PNPG/MoS_2 membrane only and pure water controls were included. The real-time temperature changes of the PNPG/MoS_2 device, PNPG/MoS_2 membrane only, and pure water were monitored using an IR camera under one sun (Fig. 5-9 and 5-11d). After 60 min irradiation, the surface temperature of the PNPG/MoS_2 device significantly increased by 18 °C. In contrast, the top temperature change of the PNPG/MoS_2 membrane only and the bulk water system increased by only 9 °C and 3 °C under the same conditions, demonstrating a weaker solar-heat conversion performance. This observation resulted from the PS insulator having a low thermal

conductivity, which can effectively reduce heat loss. As a result, the device effectively inhibited energy loss from the solar absorption layer to bulk water.

We analyzed the temperature distribution IR mapping and plots of PNPG/MoS_2 device, PNPG/MoS_2 membrane only, and pure water system after 60 min of irradiation and 1 kW m^{-2} to visually evaluate the effect of evaporator structure on thermal management and evaporation performance. The apparatus shown in Fig. 5-12a was used to evaluate solar water purification. The temperature distribution allows for a better comparison of the performance of the three devices in solar-thermal performance and energy loss. The results showed that the temperature of the solar absorber at the top of the PNPG/MoS_2 device was approximately 43 °C (Fig. 5-12b). In contrast, the comparable PNPG/MoS_2 membrane exhibited a much lower temperature of only 35 °C, and the pure water showed a negligible increase. In addition, the temperature variation trend determined from the vertical direction is demonstrated in Fig. 5-12c. As the results showed, the heat from sunlight was substantially more concentrated in the evaporation interface of the PNPG/MoS_2 device than in the PNPG/MoS_2 membrane only and pure water system. This phenomenon allows greater heat at the evaporation interface for solar water purification and less loss to bulk water. Thus, the precise concentration of local heating greatly reduced unnecessary heat loss, improving energy efficiency and promoting efficient solar vapor generation.

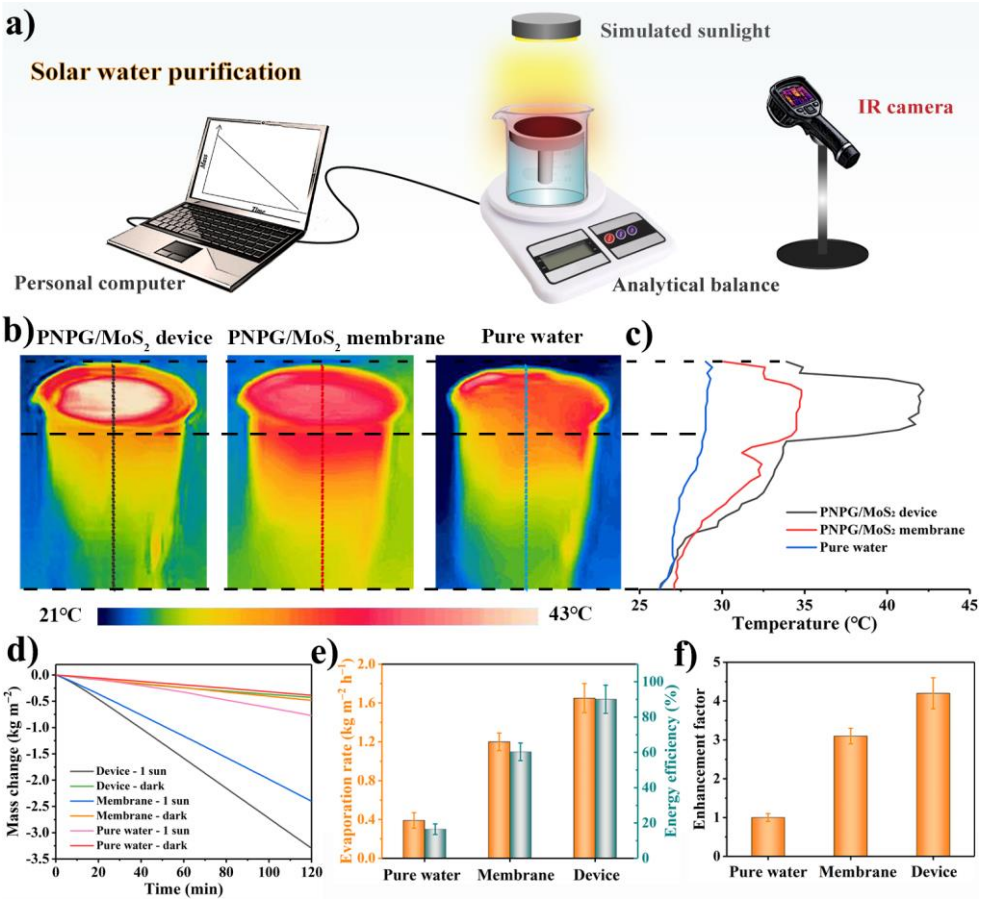

Fig. 5-12 (a) Illustration of the solar water purification measurement apparatus. (b) Temperature profiles of the PNPG/MoS_2 device, PNPG/MoS_2 membrane only, and pure water system. (c) The temperature trend of IR mapping. (d) Mass change and (e) average evaporation rate and efficiency. (f) The evaporation enhancement factor.

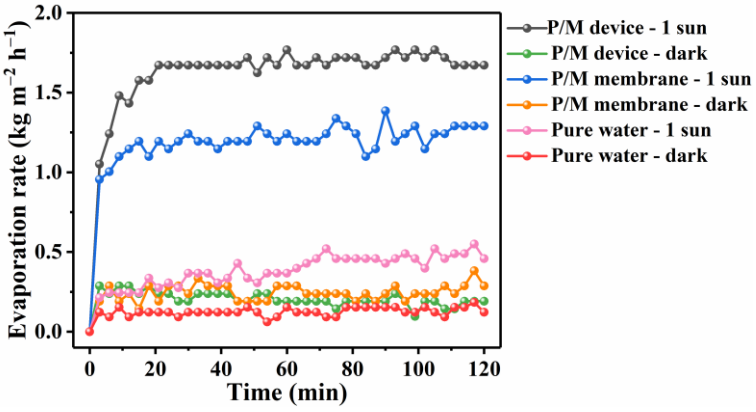

Fig. 5-13 Real-time water evaporation rate curves of the PNPG/MoS_2 device, PNPG/MoS_2 membrane only, and pure water system.

The energy utilization efficiency of solar energy determined the overall performance of solar water purification. The solar water purification performance of the PNPG/MoS_2 device, PNPG/MoS_2 membrane, and pure water system was subsequently evaluated. The water evaporation rate of pure water was determined to be 0.19 and 0.39 kg m^{-2} h^{-1}, respectively, in the absence and presence of solar light (Fig. 5-12d). For of PNPG/MoS_2 membrane only (0.24 kg m^{-2} h^{-1}), the evaporation rate did not change significantly because the interfacial evaporation area changed little, and light could not be absorbed under dark conditions. This result is due to the strong broadband absorption of PNPG/MoS_2 determining the higher evaporation rate under solar light irradiation. In contrast, the solar steam generation rate increased to 1.20 kg m^{-2} h^{-1} under the same conditions due to the robust broadband absorption of PNPG/MoS_2, which can absorb and convert solar light to heat. (Fig. 5-12d). For the PNPG/MoS_2 device system, the solar steam generation rate increased to 1.65 kg m^{-2} h^{-1} due to the improved continuous water transport capacity of the water-trapped layer and the reduced heat loss of the insulating layer (Fig. 5-12d). Moreover, as Fig. 5-13 shows, the real-time solar steam generation rate of the PNPG/MoS_2 device, PNPG/MoS_2 membrane only, and pure water system remained stable after 30 minutes of illumination, as did the evaporation rate. To compare the performance of the PNPG/MoS_2 device, PNPG/MoS_2 membrane only, and pure water more clearly, the mass change and evaporation efficiency of each system are listed separately (Fig. 5-12e). Compared to pure water (16.5%) and PNPG/MoS_2 membrane (60.3%), the PNPG/MoS_2 device achieved a more satisfactory solar steam generation rate and

efficiency (90.1%). In addition, the enhancement factor corresponded to the evaporation rate ratio of the PNPG/MoS_2 membrane, the PNPG/MoS_2 apparatus, and pure water under one sun, which is used to explain the different evaporation rates between the three systems. [40] The enhancement effect of the PNPG/MoS_2 device can be visually digitized by the enhancement factors (Fig. 5-12f).

Table 1. Comparison of performance with previous works.

Materials	**Q (sun)**	v_e **(kg m^{-2} h^{-1})**	η	**Reference**
MoS_2-cotton	1	1.287	80.1%	Ref. [19]
SWNT-MoS_2	5	6.6	91.5%	Ref. [24]
TiO_2@MoS_2	1	1.42	72.2%	Ref. [41]
MoS_2@CDs-SA	1	1.9	–	Ref. [42]
MoS_2@Sponge	1	1.204	85%	Ref. [22]
MoS_2 coating-wood	1	1.46	82.5%	Ref. [43]
MoS_2-based solar evaporator	1	1.447	84.72%	Ref. [44]
B Ns@MoS_2	1	1.538	96.5%	Ref. [45]
MoS_2/BNC aerogels	5.35	6.15	81%	Ref. [21]
$FeMoS_2$	1	1.52	90%	Ref. [46]
MoS_2 aerogels	1	1.27	88%	Ref. [18]
PNPG (coating 10mg)	1	1.72	93.5 %	Ref. [28]
PANI@PVDF	1	1.41	85%	Ref. [47]
$NiCo_xS_y$-PANI@GF	1	1.30	78.7%	Ref. [27]

PANI-Ag	1	1.37	84.7%	Ref. [48]
PNPG/MoS_2	**1**	**1.70**	**92.9%**	**This work**

The results of previous research are summarized in Table 1 for comparison with the PNPG/MoS_2 evaporator. In contrast, the PNPG/MoS_2 exhibited outstanding evaporation performance, and the evaporation rate and efficiency were comparable or superior to that in previous research.

5.3.3 The practical applications of the PNPG/MoS_2 system

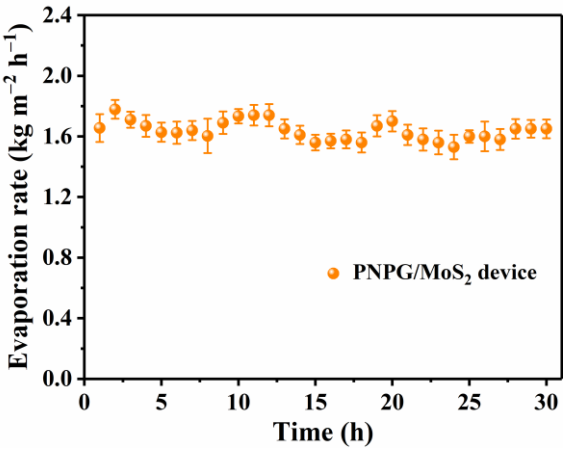

Fig. 5-14 Reusability of PNPG/MoS_2 device in solar evaporation with 30 h irradiation.

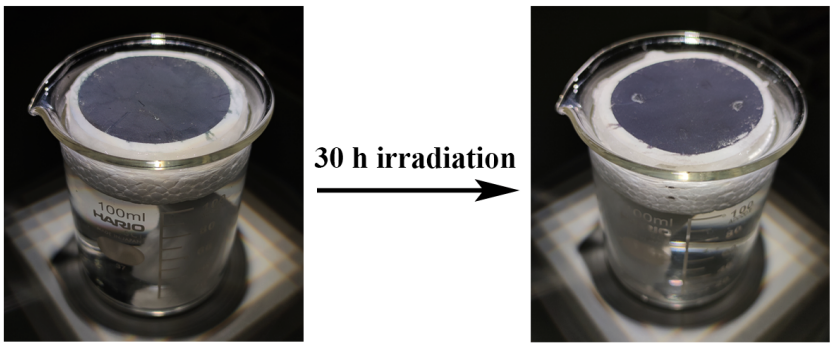

Fig. 5-15 The photos of the PNPG/MoS_2 device before and after 30 h solar irradiation.

Fig. 5-16 Photograph of the homemade solar evaporation system under 1 sun for 3 h.

Long-term stability testing can provide conclusive proof of the sustainability of the PNPG/MoS_2 apparatus. As shown in Fig. 5-14, the stability tests were performed for 30 h under one sun of irradiation. The results show that water vapor generation was maintained at a stable and efficient rate. In addition, Fig. 5-15 shows that after 30 h of seawater evaporation, the PNPG/MoS_2 membrane remained dark black, and the material was not damaged. Furthermore, there was only a small amount of salt deposition on the membrane, caused by insufficient contact with the water-trapped layer at this location. The above results indicate that the PNPG/MoS_2 device is stable and can be applied in practice.

The PNPG/MoS_2 device was used as a viable solar evaporator for wastewater purification and seawater desalination to produce clean water sustainably. An in-house manufactured device, as displayed in Fig. 5-16, was used to collect the purification

water. As Fig. 5-17a shows, the solar evaporation performance of the PNPG/MoS_2 device was measured under harsh aqueous solution conditions, including strong acid (pH 1 sulfuric acid) and alkali (pH 13 sodium hydroxide). The average solar steam generation rate of the PNPG/MoS_2 device remained steady even under such severe conditions. The evaporation rate of artificial and natural seawater was to some extent lower than that of domestic drinking water because of the influence of a small amount of salt crystallization in the evaporation process, which admittedly has little effect on the overall evaporation rate. Purified water collected from acidic or alkaline solutions demonstrated a near-neutral pH, as shown in Fig. 5-17 b and c. In addition, in determining the organic dye removal capability from wastewater using the PNPG/MoS_2 device, we found the obvious characteristic wastewater bands (MB = 664 nm, MO = 454 nm, and RhB = 554 nm) completely disappeared after purification. As shown in Fig. 5-17 d and f, the color of the purified water from wastewater was colorless and transparent.

To further verify its capability to purify seawater, the concentration variations of major cations (including Na^+, Mg^{2+}, K^+, and Ca^{2+}) were determined by ICPE-9000. The concentrations of Na^+, Mg^{2+}, K^+, and Ca^{2+} sharply decreased to 3.37, 0.627, 0.143, and 1.04 mg L^{-1} respectively after solar purification (Fig. 5-17g), which are substantially below the salinity standard for drinking water set by the WHO (1‰).[49] Furthermore, resistance tests confirm water quality acceptability after solar desalination. As seen in Fig. 5-17h, the resistance value of purified water increased from 102.9 KΩ of natural seawater to 1.945 MΩ, far exceeding the value of 0.885 MΩ of domestic water,

indicating that solar seawater desalination can effectively produce clean water. The reliable water purification rate and water quality indicate that the PNPG/MoS_2 device is promising for water purification. Furthermore, these results indicate that the PNPG/MoS_2 system has high efficiency and potential in solar evaporation and wastewater treatment.

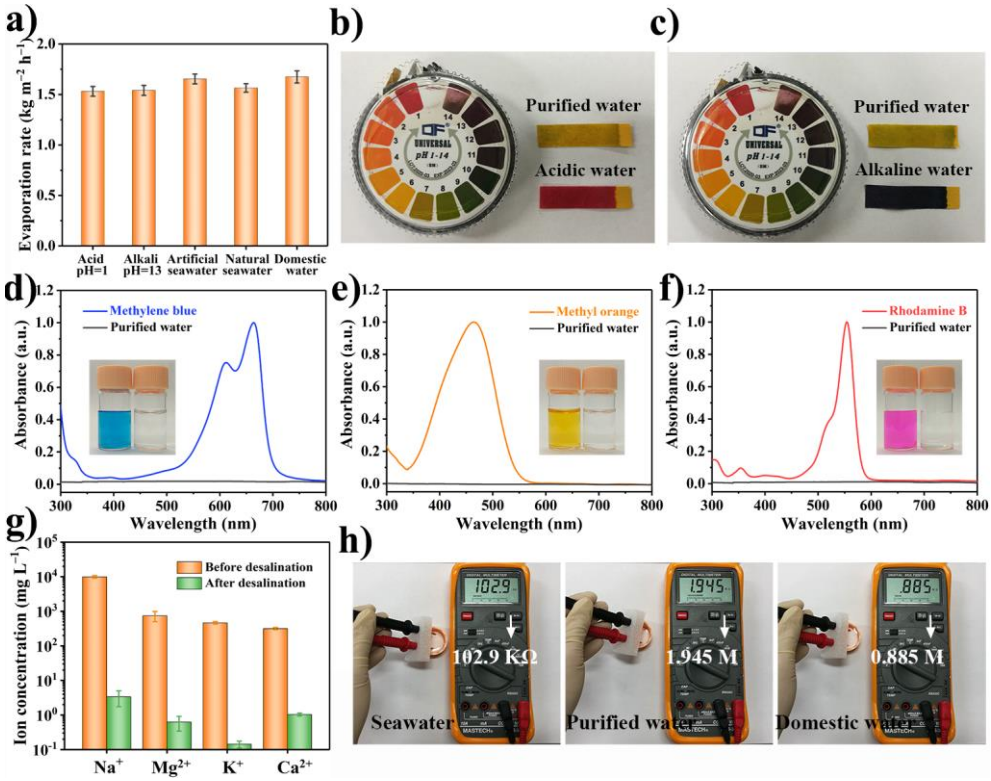

Fig. 5-17 (a) Average evaporation rates of the individual water samples irradiated by 1 kW m^{-2}. The pH of (b) acid, (c) alkali, and the purified water was confirmed by pH test paper. (d-f) UV-vis spectrum of different wastewater types with or without purification. Inset: photos of dye solution and solar-purified water. (g) The concentrations of four main cations in seawater and purified water. (h) Resistance tests for seawater, purified water, and domestic water with a multimeter.

Although heat locating allowed the PNPG/MoS_2 device to achieve efficient

evaporation, in the evaporation process, there was still a large temperature difference between PNPG/MoS_2 membrane and the water-trapped layer, inevitably leading to heat loss. To remedy this, a solar evaporation-thermoelectricity generating device was designed to co-generate power and produce clean water. The thermoelectric effect accompanying solar water evaporation was realized by a commercial TE module (Fig. 5-18a). In this setup, the cotton water-trapped layer was readily shaped to conformally load a TE module while simultaneously ensuring efficient water transportation for solar water evaporation. Meanwhile, the solar evaporation-thermoelectricity generating device can float on water, assisted by the PS insulator.

The real-time temperature difference between the upper and lower parts of the TE module was monitored using a thermocouple (Fig. 5-18b). There was a stable temperature difference of approximately 6 ℃ using the photothermal membrane under one sun irradiation, while the blank group only formed at 2 ℃. Here, the TE module also acted as an insulator, reducing heat loss and thus improving the rate of solar evaporation. The evaporation rates of PNPG/MoS_2 devices with or without TE module were 1.70 kg m^{-2} h^{-1} and 1.65 kg m^{-2} h^{-1}, respectively (Fig. 5-18c). Moreover, the efficiency increased from 90.1% to 92.9%, indicating a slight improvement overall (Fig. 5-18d).

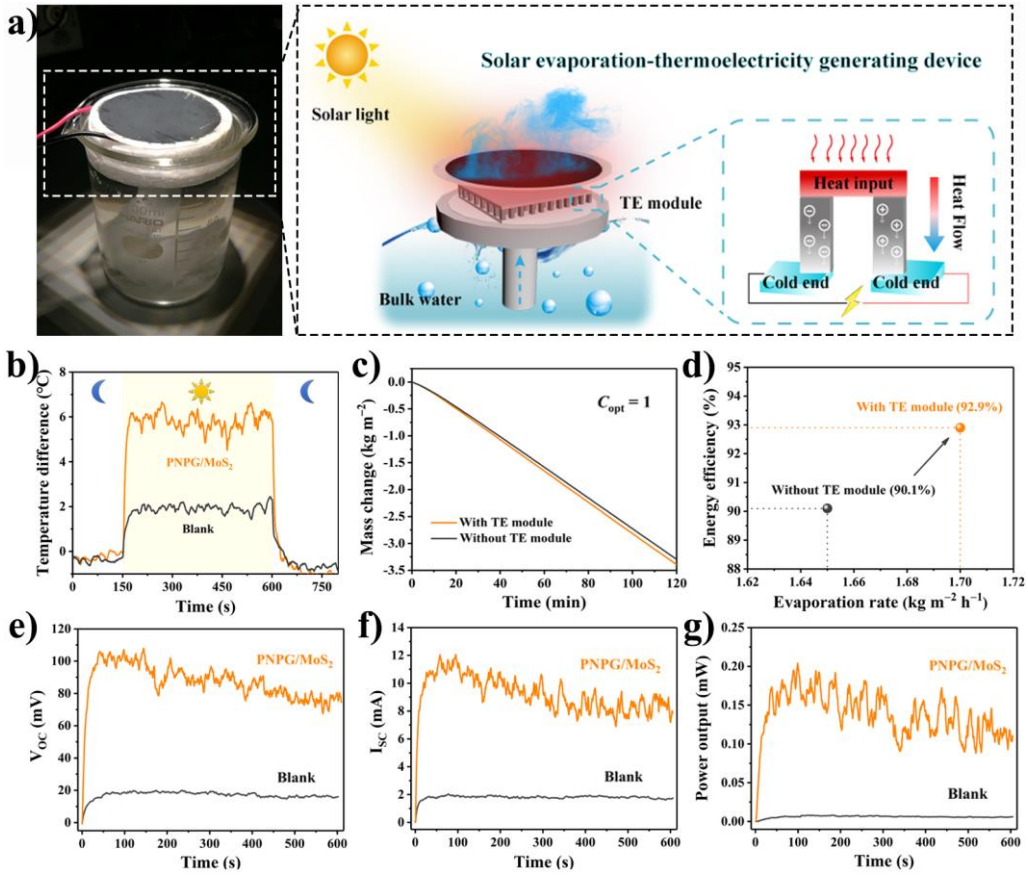

Fig. 5-18 (a) Schematic of the simultaneous solar evaporation–thermoelectricity generating device. (b) The temperature difference between the upper and lower parts of the TE module covering a PNPG/MoS_2 membrane or blank under one sun. (c) Water mass changes over time with or without the TE module and (d) solar evaporation efficiency. (e) Open circuit voltage (V_{oc}) and (f) short circuit current (I_{sc}) for thermoelectric generation by the PNPG/MoS_2 device. (g) The output power of the PNPG/MoS_2 device and the blank for the loading a 3 Ω resistance.

Fig. 5-19 Photograph of thermoelectricity generation setup and the electrical signal testing system.

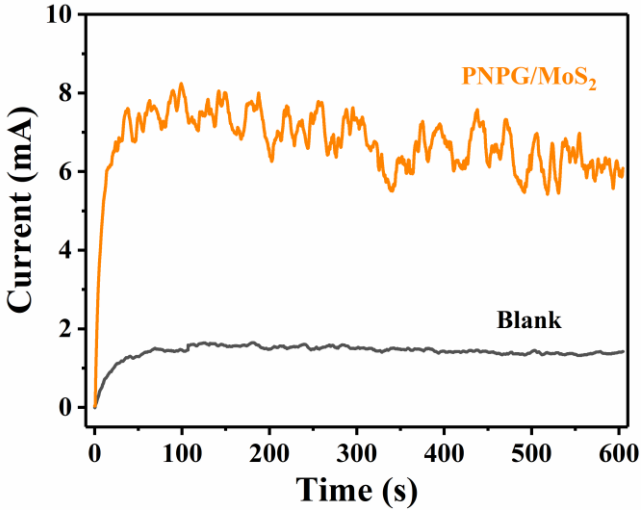

Fig. 5-20 Load current of PNPG/MoS_2 device with TE module and the single TE module under 1 sun.

To monitor the power generation performance of the solar evaporation-thermoelectricity generating device, the V_{oc} and I_{sc} were recorded in real-time (Fig. 5-19). As shown in Fig. 5-18 e and f, the induced maximum V_{oc} and I_{sc} of the solar evaporation-thermoelectricity generating devices were approximately 110 mV and 12 mA, respectively. By comparison, much lower values of only 20 mV and 1.8 mA were obtained in the control measurements. We estimated the theoretical power performance of the solar evaporation–thermoelectricity generating device by connecting an external resistor with resistance (3 Ω). The corresponding current was measured (Fig. 5-20). The results are shown in Fig. 5-18g. The power output of the solar evaporation–thermoelectricity generating device at 1 kW m^{-2} was 0.21 mW, which is higher than that of the blank (0.005 mW). Because the size of the TE module used in the experiment was 30 mm × 30 mm, the calculated maximum power was 0.23 W m^{-2}. Although a single TE module is weak, achieving a larger output through a large-scale series connection is straightforward. The as-designed PNPG/MoS_2 solar evaporation–thermoelectricity generating device shows a synergy for water purification and power generation, which improves the comprehensive utilization rate of solar energy. This device could be practically significant for harnessing the extra energy generated by the evaporation process.

5.4 Conclusion

In this study, we designed and fabricated a PNPG/MoS_2 solar evaporation system with broad-spectra solar light for efficient solar water purification. The addition of

environment-friendly MoS_2 expanded the light absorption capacity of photothermal polymer PNPG, leading to the synergistic photothermal enhancement effect. Furthermore, PNPG/MoS_2 demonstrated effective light capture and inherent superhydrophilicity, resulting in efficient water transport and local heating. Thus, the PNPG/MoS_2 device exhibited excellent solar-to-vapor performance at a rate of 1.65 kg m^{-2} h^{-1} and an efficiency to be 90.1% at 1 kW m^{-2}. Furthermore, the PNPG/MoS_2 photothermal membrane has good flexibility and can be applied in extreme water environments, exhibiting good physical and chemical stability. More importantly, we demonstrated the integral design of simultaneous solar evaporation and thermoelectricity generation. TE module collects low-grade waste heat by taking advantage of the Seebeck effect caused by temperature differences in the evaporation process, and at the same time plays an insulating role in the evaporation process. Under one sun of solar irradiation, a higher evaporation rate of 1.70 kg m^{-2} h^{-1} and an output of 0.23 W m^{-2} were realized concurrently. Therefore, this study demonstrated the promising use of solar-thermal energy and provided an effective approach for the synergy of solar water purification and power generation to meet clean water and green energy challenges.

Reference

[1] Y. Lu, N. Nakicenovic, M. Visbeck, A.S. Stevance, Policy: Five priorities for the UN Sustainable Development Goals, Nature 520 (2015) 432-433.

[2] M.-H. Yuan, S.-L. Lo, Developing indicators for the monitoring of the sustainability of food, energy, and water, Renewable and Sustainable Energy Reviews 119 (2020) 109565-109573.

[3] W. Shang, T. Deng, Solar steam generation: Steam by thermal concentration, Nat. Energy 1 (2016) 1-2.

[4] X. Li, R. Lin, G. Ni, N. Xu, X. Hu, B. Zhu, G. Lv, J. Li, S. Zhu, J. Zhu, Three-dimensional artificial transpiration for efficient solar waste-water treatment, Natl. Sci. Rev. 5 (2018) 70-77.

[5] C. Chen, Y. Kuang, L. Hu, Challenges and Opportunities for Solar Evaporation, Joule 3 (2019) 683-718.

[6] Y. Guo, J. Bae, Z. Fang, P. Li, F. Zhao, G. Yu, Hydrogels and Hydrogel-Derived Materials for Energy and Water Sustainability, Chem. Rev. 120 (2020) 7642-7707.

[7] M. Gao, L. Zhu, C.K. Peh, G.W. Ho, Solar absorber material and system designs for photothermal water vaporization towards clean water and energy production, Energy Environ. Sci. 12 (2019) 841-864.

[8] J. Zhou, Y. Gu, P. Liu, P. Wang, L. Miao, J. Liu, A. Wei, X. Mu, J. Li, J. Zhu, Development and Evolution of the System Structure for Highly Efficient Solar Steam Generation from Zero to Three Dimensions, Adv. Funct. Mater. 29 (2019) 1903255-1903274.

[9] K. Xu, C. Wang, Z. Li, S. Wu, J. Wang, Salt Mitigation Strategies of Solar‐Driven Interfacial Desalination, Adv. Funct. Mater. (2020) 2007855-2007880.

[10] X. Zhou, F. Zhao, P. Zhang, G. Yu, Solar Water Evaporation Toward Water Purification and Beyond, ACS Materials Letters (2021) 1112-1129.

[11] I. Ibrahim, D.H. Seo, A.M. McDonagh, H.K. Shon, L. Tijing, Semiconductor photothermal materials enabling efficient solar steam generation toward desalination and wastewater treatment, Desalination (2020) 114853-114874.

[12] D. Shin, G. Kang, P. Gupta, S. Behera, H. Lee, A.M. Urbas, W. Park, K. Kim, Thermoplasmonic and Photothermal Metamaterials for Solar Energy Applications, Adv. Opt. Mater. 6 (2018) 1800317-1800342.

[13] W. Guan, Y. Guo, G. Yu, Carbon Materials for Solar Water Evaporation and Desalination, Small (2021) 2007176-2007192.

[14] S.W. Sharshir, A.M. Algazzar, K.A. Elmaadawy, A.W. Kandeal, M.R. Elkadeem, T. Arunkumar, J. Zang, N. Yang, New hydrogel materials for improving solar water evaporation, desalination and wastewater treatment: A review, Desalination 491 (2020) 114564-1145681.

[15] I. Ibrahim, V. Bhoopal, D.H. Seo, M. Afsari, H.K. Shon, L.D. Tijing, Biomass-based photothermal materials for interfacial solar steam generation: a review, Mater. Today Energy 21 (2021) 100716-100734.

[16] Z. Xie, Y. Duo, Z. Lin, T. Fan, C. Xing, L. Yu, R. Wang, M. Qiu, Y. Zhang, Y. Zhao, X. Yan, H. Zhang, The Rise of 2D Photothermal Materials beyond Graphene for Clean Water Production, Advance Science 7 (2020) 1902236-1902258.

[17] Z. Xie, Y.-P. Peng, L. Yu, C. Xing, M. Qiu, J. Hu, H. Zhang, Solar‐Inspired Water Purification Based on Emerging 2D Materials: Status and Challenges, Solar RRL 4 (2020) 1900400-1900427.

[18] Q. Wang, Q. Guo, F. Jia, Y. Li, S. Song, Facile Preparation of Three-Dimensional MoS2 Aerogels for Highly Efficient Solar Desalination, ACS Appl. Mater. Interfaces 12 (2020) 32673-32680.

[19] Z. Guo, G. Wang, X. Ming, T. Mei, J. Wang, J. Li, J. Qian, X. Wang, PEGylated Self-Growth MoS2 on a Cotton Cloth Substrate for High-Efficiency Solar Energy Utilization, ACS Appl. Mater. Interfaces 10 (2018) 24583-24589.

[20] L. Huang, G. Li, A. Gurarslan, Y. Yu, R. Kirste, W. Guo, J. Zhao, R. Collazo, Z. Sitar, G.N. Parsons, M. Kudenov, L. Cao, Atomically Thin MoS2 Narrowband and Broadband Light Superabsorbers, ACS Nano 10 (2016) 7493-7499.

[21] D. Ghim, Q. Jiang, S. Cao, S. Singamaneni, Y.-S. Jun, Mechanically interlocked 1T/2H phases of MoS2 nanosheets for solar thermal water purification, Nano Energy 53 (2018) 949-957.

[22] Q. Wang, F. Jia, A. Huang, Y. Qin, S. Song, Y. Li, M.A.C. Arroyo, MoS2@sponge with double layer structure for high-efficiency solar desalination, Desalination 481 (2020) 114359-114365.

[23] X. Zhao, X.-J. Zha, L.-S. Tang, J.-H. Pu, K. Ke, R.-Y. Bao, Z.-y. Liu, M.-B. Yang, W. Yang, Self-assembled core-shell polydopamine@MXene with synergistic solar absorption capability for highly efficient solar-to-vapor generation, Nano Res. 13 (2019) 255-264.

[24] X. Yang, Y. Yang, L. Fu, M. Zou, Z. Li, A. Cao, Q. Yuan, An Ultrathin Flexible 2D Membrane Based on Single-Walled Nanotube-MoS2 Hybrid Film for High-Performance Solar Steam Generation, Adv. Funct. Mater. 28 (2018) 1704505-1704513.

[25] Y. Xu, J. Ma, Y. Han, H. Xu, Y. Wang, D. Qi, W. Wang, A simple and universal strategy to deposit Ag/polypyrrole on various substrates for enhanced interfacial solar evaporation and antibacterial activity, Chem. Eng. J. 384 (2020) 123379-123387.

[26] R. Zhu, M. Liu, Y. Hou, D. Wang, L. Zhang, D. Wang, S. Fu, Mussel-inspired photothermal synergetic system for clean water production using full-spectrum solar energy, Chem. Eng. J. 423 (2021) 129099.

[27] L. Ying, H. Zhu, H. Huang, X. Qu, C. Wang, X. Wang, F. Duan, S. Lu, M. Du, Scalable NiCoxSy-PANI@GF Membranes with Broadband Light Absorption and High Salt-Resistance for Efficient Solar-Driven Interfacial Evaporation, ACS Appl. Energy Mater. 4 (2021) 3563-3572.

[28] Z. Lin, T. Wu, J. Shi, B. Zhou, C. Zhu, Y. Wang, R. Liang, M. Mizuno, Poly(N-phenylglycine)-Based Bioinspired System for Stably and Efficiently Enhancing Solar Evaporation, ACS Sustainable Chem. Eng. 9 (2021) 448-457.

[29] B.P. Jiang, L. Zhang, X.L. Guo, X.C. Shen, Y. Wang, Y. Zhu, H. Liang, Poly(n-phenylglycine)-based nanoparticles as highly effective and targeted near-infrared photothermal therapy/photodynamic therapeutic agents for malignant melanoma, Small 13 (2017) 1602496-1602510.

[30] H. Bai, T. Zhao, M. Cao, Interfacial solar evaporation for water production: from structure design to reliable performance, Molecular Systems Design & Engineering 5

(2020) 419-432.

[31] F. Zhao, Y. Guo, X. Zhou, W. Shi, G. Yu, Materials for solar-powered water evaporation, Nat. Rev. Mater. 5 (2020) 388-401.

[32] T. Ding, G.W. Ho, Using the sun to co-generate electricity and freshwater, Joule 5 (2021) 1639-1641.

[33] G. Liu, T. Chen, J. Xu, G. Li, K. Wang, Solar evaporation for simultaneous steam and power generation, J. Mater. Chem. A 8 (2020) 513-531.

[34] X. Li, X. Min, J. Li, N. Xu, P. Zhu, B. Zhu, S. Zhu, J. Zhu, Storage and Recycling of Interfacial Solar Steam Enthalpy, Joule 2 (2018) 2477-2484.

[35] L. Zhu, T. Ding, M. Gao, C.K.N. Peh, G.W. Ho, Shape Conformal and Thermal Insulative Organic Solar Absorber Sponge for Photothermal Water Evaporation and Thermoelectric Power Generation, Adv. Energy Mater. 9 (2019) 1900250-1900256.

[36] Y. Duan, M. Weng, W. Zhang, Y. Qian, Z. Luo, L. Chen, Multi-functional carbon nanotube paper for solar water evaporation combined with electricity generation and storage, Energy Convers. Manage. 241 (2021) 114306-114317.

[37] H.-H. Yu, L.-J. Yan, Y.-C. Shen, S.-Y. Chen, H.-N. Li, J. Yang, Z.-K. Xu, Janus Poly(Vinylidene Fluoride) Membranes with Penetrative Pores for Photothermal Desalination, Research 2020 (2020) 1-10.

[38] Q. Lu, W. Shi, H. Yang, X. Wang, Nanoconfined Water-Molecule Channels for High-Yield Solar Vapor Generation under Weaker Sunlight, Adv. Mater. 32 (2020) 2001544-2001550.

[39] N. Maity, A. Mandal, A.K. Nandi, High dielectric poly(vinylidene fluoride)

nanocomposite films with MoS2 using polyaniline interlinker via interfacial interaction, Journal of Materials Chemistry C 5 (2017) 12121-12133.

[40] J. Yang, Y. Chen, X. Jia, Y. Li, S. Wang, H. Song, Wood-Based Solar Interface Evaporation Device with Self-Desalting and High Antibacterial Activity for Efficient Solar Steam Generation, ACS Appl. Mater. Interfaces 12 (2020) 47029-47037.

[41] B. Yuan, L. Meng, C. Zhang, L. Yang, L. Bai, H. Yang, D. Wei, F. Wang, Q. Wang, W. Wang, H. Chen, Enhancement of pollutant degradation and solar-driven water evaporation by architecting hierarchical 1D/2D TiO2 @ MoS2 core–shell networks, Appl. Surf. Sci. 570 (2021).

[42] Z. Guo, J. Wang, Y. Wang, J. Wang, J. Li, T. Mei, J. Qian, X. Wang, Achieving steam and electrical power from solar energy by MoS2-based composites, Chem. Eng. J. 427 (2022) 131008-131016.

[43] X. He, L. Zhang, X. Hu, Q. Zhou, Formation of S defects in MoS2-coated wood for high-efficiency seawater desalination, Environ. Sci. Nano 8 (2021) 2069-2080.

[44] R. Chen, X. Wang, Q. Gan, T. Zhang, K. Zhu, M. Ye, A bifunctional MoS2-based solar evaporator for both efficient water evaporation and clean freshwater collection, J. Mater. Chem. A 7 (2019) 11177-11185.

[45] J. Yin, X. You, Z. Zhang, Z. Guo, J. Wang, X. Wang, Boron nanosheets loaded with MoS2 porous sponges for water purification, J. Water Process. Eng. 41 (2021) 102048-102056.

[46] Z. Guo, Z. Chen, Z. Shi, J. Qian, J. Li, T. Mei, J. Wang, X. Wang, P. Shen, Stable metallic 1T phase engineering of molybdenum disulfide for enhanced solar vapor

generation, Sol. Energy Mater. Sol. Cells 204 (2020) 110227-110233.

[47] Y. Zou, X. Chen, W. Guo, X. Liu, Y. Li, Flexible and Robust Polyaniline Composites for Highly Efficient and Durable Solar Desalination, ACS Appl. Energy Mater. 3 (2020) 2634-2642.

[48] R. Li, C. Zhou, L. Yang, J. Li, G. Zhang, J. Tian, W. Wu, Multifunctional cotton with PANI-Ag NPs heterojunction for solar-driven water evaporation, J. Hazard. Mater. 424 (2021) 127367-127379.

[49] F. Zhao, X. Zhou, Y. Shi, X. Qian, M. Alexander, X. Zhao, S. Mendez, R. Yang, L. Qu, G. Yu, Highly efficient solar vapour generation via hierarchically nanostructured gels, Nat. Nanotechnol. 13 (2018) 489-495.

Chapter 6 Summary

Solar desalination technology is a low-cost, green, and pollution-free water purification technology, but it has not been popularized for a long time due to the low photothermal conversion efficiency and the output of freshwater per unit area. The introduction of light absorber and interface heating technology has greatly improved its photothermal conversion efficiency. This paper focuses on high-efficiency photothermal steam, studies the construction of polymer-based photothermal vaporizers, and effectively explores potential applications. The work in this paper can be divided into the following points.

(1) A bio-inspired solar steam generator based on PNPG was successfully prepared using a low-cost, environmentally friendly, and scalable process for solar seawater desalination and dye removal. PNPG has effective and broadband absorption in the UV-vis-NIR region, which illustrates the high solar light absorption of the prepared device. At the same time, the construction of devices for effective thermal insulation, water-trapped, and water supply makes the solar evaporation process obtain high efficiency and high evaporation rate. This novel bio-inspired PNPG-based device applies high efficient solar-thermal conversion effect to steam generation, which exhibits the feasible application in solar desalination and pollutants removal.

(2) Inspired by the transpiration process of trees, a high-effective PNPG wood solar evaporator with the advantages of being cost-effective, convenient, and environment-friendly was developed by a simple drop-casting method. Due to natural

water transport channels and low thermal conductivity of the wood, as well as the effective solar-heat conversion of PNPG, the PNPG wood solar evaporator has achieved rapid water transfer, excellent interface thermal positioning, and local heat management ability. Such a well-designed, low cost cost-effective, and high-efficiency PNPG wood solar evaporation system has the potential to be applied to solve the practical problem of seawater desalination and water purification.

(3) We designed and fabricated a PNPG/MoS_2 solar evaporation system with broad-spectra solar light for efficient solar water purification. The addition of environment-friendly MoS_2 expanded the light absorption capacity of photothermal polymer PNPG, leading to the synergistic photothermal enhancement effect. Furthermore, PNPG/MoS_2 demonstrated effective light capture and inherent superhydrophilicity, resulting in efficient water transport and local heating. In addition, we demonstrated the integral design of simultaneous solar evaporation and thermoelectricity generation. TE module collects low-grade waste heat by taking advantage of the Seebeck effect caused by temperature differences in the evaporation process, and at the same time plays an insulating role in the evaporation process. This study demonstrated the promising use of solar-thermal energy and provided an effective approach for the synergy of solar water purification and power generation to meet clean water and green energy challenges.

Publications

1. Periodical papers

(1) **Zhaoxing Lin**, Tingting Wu, Yan-Fang Feng, Jian Shi, Bo Zhou, Chunhong Zhu, Yiyu Wang, Ruilu Liang, Mamoru Mizuno, Poly(N-phenylglycine)/MoS_2 nanohybrid with synergistic solar-thermal conversion for efficient water purification and thermoelectric power generation. ***ACS Applied Materials & Interfaces*** 2022, 14 (1), 1034-1044. (Impact Factor = 9.229)

(2) **Zhaoxing Lin**, Tingting Wu, Benxu Jia, Jian Shi, Bo Zhou, Chunhong Zhu, Yiyu Wang, Ruilu Liang, Mamoru Mizuno, Nature-inspired poly(N-phenylglycine)/wood solar evaporation system for high-efficiency desalination and water purification. ***Colloids and Surfaces A: Physicochemical and Engineering Aspects*** 2022, 637, 128272-128280. (Impact Factor = 4.539)

(3) **Zhaoxing Lin**, Tingting Wu, Jian Shi, Bo Zhou, Chunhong Zhu, Yiyu Wang, Ruilu Liang, Mamoru Mizuno, Poly(N-phenylglycine)-based bioinspired system for stably and efficiently enhancing solar evaporation. ***ACS Sustainable Chemistry & Engineering*** 2021, 9, 448-457. (Impact Factor = 8.198)

(4) Tingting Wu, **Zhaoxing Lin**, Hongyi Wu, Chunhong Zhu, Takao Komiyama, Jian Shi, Ruilu Liang, Selective and sensitive adsorption of Au(III) by poly-N-phenylglycine. ***Separation and Purification Technology*** 2022, 287, 120604-120614. (Impact Factor = 7.312)

(5) Tingting Wu, **Zhaoxing Lin**, Hongyi Wu, Mingxu Wang, Chunhong Zhu, Kanazawa Nobuhiro, Jian Shi, Ruilu Liang, Adsorption studies on Ag(I) using poly-N-phenylglycine membrane and application in practical silver recycling. ***ACS Applied Polymer Materials***, DOI:10.1021/acsapm.1c01901. (Impact Factor = 4.089)

Note: Doctoral dissertation related: 3 papers ((1) ~ (3)), others: 2 papers ((4) ~ (5)).

2. Conference

(1) **Zhaoxing Lin**, Tingting Wu, Jian Shi, Mamoru Mizuno, Poly(N-phenylglycine)-based photothermal membrane system for stably solar evaporation. ***The Society of Fiber Science and Technology Japan Autumn Meeting*** 2021, Online.

(2) **Zhaoxing Lin**, Tingting Wu, Jian Shi, Mamoru Mizuno, One-step preparation of a water soluble phycocyanin-carbon nanohorn hybrid for cancer phototherapy. ***The Society of Fiber Science and Technology Japan Autumn Meeting*** 2019, Ueda, Nagano.

(3) Tingting Wu, **Zhaoxing Lin**, Ruilu Liang, The adsorption mechanism between conductive polymer poly-N-phenylglycine on Ag(I) and recovery of silver, ***The Mining and Materials Processing Institute of Japan Annual Meeting*** 2022, Online

(4) Tingting Wu, **Zhaoxing Lin**, Ruilu Liang, Poly-N-phenylglycine membrane for recovery of Au from trace-level solution, ***The Mining and Materials Processing Institute of Japan Annual Meeting*** 2021, Online

Acknowledgments

Time flies and the years fly by, and the three-year doctoral study is coming to an end. These three years of studying abroad are the most unforgettable time in my life. I am very grateful to those who helped me during this time.

First of all, I would like to thank my supervisors, Professor Mamoru Mizuno and Assistant Professor Jian Shi, for their guidance and support. Secondly, I would like to thank Associate Professor Ruilu Liang from Akita Prefectural University and Associate Professor Chunhong Zhu from Shinshu University for their guidance and advice, which were very helpful to my research work.

Thanks to Prof. Teruo Bitoh, Faculty of Systems Science, Akita Prefectural University, and Prof. Ick-Soo Kim, Faculty of Fiber, Shinshu University, for their comments and suggestions, whose suggestions were invaluable to my research.

I would like to thank Professor Xingcan Shen and Professor Bangping Jiang from the School of Chemistry of Guangxi Normal University, and Dr. Bo Zhou of Guilin Medical College for their guidance and suggestions on my research work.

I would also like to thank my friends during my PhD period, including Haodao Mo, Hongjian Huang, Manxi Sun, Chunyin Lu, Wei Zhao, Ming Feng, Dongdong Zhao, Qiaoqiao Li, and Fang Xin, for their assistance, friendship, and support in my research.

Thank you to my girlfriend Tingting Wu for her company and support over the years, and even more to my family for their support, encouragement, and patience during my study and throughout my life.

Zhaoxing Lin

2022.09, Yurihonjo City, Japan